GOTTFRIED WILHELM LEIBNIZ UNIVERSITÄT HANNOVER
INSTITUT FÜR METEOROLOGIE UND KLIMATOLOGIE

Master Thesis

Influences on the reflectance of Arctic sea ice and the impact of anthropogenic impurities on the surface shortwave radiation balance

by
Hannes Schulz

Supervisors:
Prof. Dr. Gunther Seckmeyer, IMuK
Ansgar Stührmann, IMuK
Dr. Andreas Herber, AWI
Dr. Gerit Birnbaum, AWI

Examiners:
Prof. Dr. Gunther Seckmeyer, IMuK
Dr. Andreas Herber, AWI

November 2014

ALFRED-WEGENER-INSTITUT
HELMHOLTZ-ZENTRUM FÜR POLAR-
UND MEERESFORSCHUNG

Abstract

In order to investigate influences on the reflectance of snow covered Arctic sea ice, a discrete ordinate method and Mie-Theory based radiative transfer model has been set up. This model, the Snow on Sea Ice Model (SoSIM), is able to investigate changes in spectral and spectrally integrated (broadband) albedo of a multi-layer snow cover on sea ice due to varying snow microphysical parameters, atmospheric composition and incoming solar radiation. For typical conditions in the Arctic sea-ice area, it was found that the size of spherical snow grains and the angle of the sun above the horizon ultimately determine both spectral and broadband albedo of a thick snow layer. At 1300 nm, doubling the snow grain size decreases the albedo by about 20%, while a lower incident angle of solar light can offset this effect. The light absorbing impurity black carbon (soot) has a distinct influence on the albedo in the ultra-violet and visible range of the solar spectrum. However, it likely only lowers the albedo by less than 2%, for present concentrations of black carbon in Arctic snow. The spectral signature of black carbon is very similar to a thinning snow cover on top of a darker surface. SoSIM was also tested against other models and parametrisations for the spectral and broadband albedo of snowpacks as well as against field measurements of the spectral albedo of snow covered sea ice. The test proved the plausibility of the model results.

Further, broadband albedo data from an airborne measurement campaign has been evaluated together with accompanying data such as sea ice thickness. This data demonstrated that sea-ice dynamics cause strong local surface heterogeneities. As a consequence, a strong variation is found in the spatially averaged surface albedo. To quantify this surface heterogeneity, an algorithm has been developed that automatically classifies typical freeze-up season surface covers of the Arctic ocean from photographs.

As a combination of the findings from model study and evaluation of the campaign data, a model could be developed able to re-analyse the spatial distribution of broadband surface albedo of the Arctic ocean. The model utilises spatial information based on satellite observation of sea-ice concentration and thickness as well as climatological data of snow thickness. It is an alternative approach to derive the surface albedo based on SoSIM and not relying on satellite measurements in the visible range of the spectrum. First validations with air and satellite borne measurements of albedo distributions showed that the modelled albedo is plausible, yet has no better accuracy than $\pm 5\%$. The model was used to predict the surface forcing of changes in the albedo as caused by the deposition of anthropogenic light absorbing substances onto the snow cover. It was found that depositing 40 ppbw black carbon into a pure snowpack causes an extra absorption of $1.58 \pm 0.83\,\mathrm{W/m^2}$ on average for the sea ice covered Arctic. The high relative uncertainty is caused by the uncertainty involved in the enhancement of light absorption by BC particles due to ageing processes.

Contents

1. Introduction and motivation

Sea ice covering the polar oceans is a key component in the global climate system. The ice cover has a strong impact on the shortwave energy budget via its much higher reflectance compared to the open ocean. The hemispheric reflectance, or albedo, is often used to express how much of the incoming sunlight is reflected by a surface. The presence of bare sea ice raises the low albedo of the ocean surface in a way that about half of the incoming solar radiation is reflected. Yet, the accumulation of snow upon the ice raises the albedo even further – compare with Figure 1.1 showing the three different surface types present during the freeze-up season. In fact, most of the sea ice is covered with a snow layer of varying depth. The highest albedo values are found for newly fallen thick snow layers. Yet, the albedo decreases over time as ageing processes change the microphysical structure of the snow layer – even without any melt processes taking place. Hence, properties of the snow that influence the albedo can change the energy uptake of shortwave solar radiation at the surface by more than 10% (Figure 1.1).
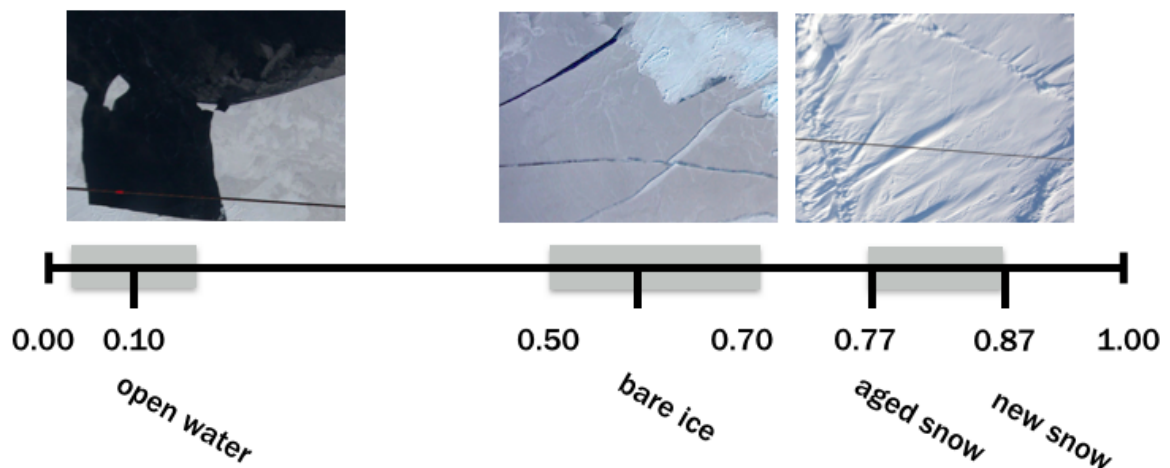
Figure 1.1: The range of albedo values in the Arctic almost spans the entire interval (0 for a black and 1 for a perfect white surface). The photographs show three commonly observed situations, featuring dark open ocean water, greyish bare sea ice and bright snow covered ice, as well as mixtures of the three surface types. The Figure is composed after Wadhams [2000] with data from Perovich et al. [1998] and photographs of the surface automatically taken during the campaign PAMARCMiP 2009 – see Chapter 4.

Sea ice in the Arctic is also one of the most rapidly changing components of the global climate system. Over the past few decades, its summer areal extent has declined over 30%, additionally all months show statistically significant declining trends [Meier et al., 2014]. Satellite-derived data indicate a 40% decline since the 1980s in sea-ice thickness, mostly due to a loss of older, i.e. thicker, sea ice cover [Meier et al., 2014]. These changes in sea ice are happening faster than models have projected [Meier et al., 2014].

The onset of melt of the snow cover significantly changes the radiative balance of the sea ice, with albedo dropping from about 0.8 for cold, dry snow to 0.5 or less for melting snow [Perovich and Polashenski, 2012]. A trend towards earlier melt onsets has been found from passive microwave satellite data. From 1970 to 2013, the onset of melt has trended earlier by an average of 5 days per decade [Stroeve et al., 2014].

Under most atmospheric conditions, absorption of shortwave radiation is the largest energy source for heating the surface and melting snow and ice [Paterson and Reeh, 2001]. The amount of shortwave radiation absorbed depends on both incident radiation and surface albedo. Hansen and Nazarenko [2004] have shown that changes to snow albedo are twice as efficient in changing the global near-surface air temperature than an equal forcing by greenhouse gases like carbon dioxide. Snow albedo changes directly increase the energy deposition at the surface where it enhances snow ageing processes that degrade the albedo. Thus, the positive ice-albedo feedback increases the amount of absorbed energy. This feedback is a normal process leading to rising temperatures and melting of snow and ice at the beginning of the melting season. However, the feedback may be amplified by additionally lowering the albedo by depositions of light absorbing aerosols, thus causing an earlier onset of spring melt [e.g. Flanner et al., 2009, Hansen and Nazarenko, 2004]. In turn, if melting starts earlier, the ocean can gain more heat from solar energy over the summer [Perovich and Polashenski, 2012] and autumn freeze-up is subsequently delayed by the time needed for the ocean mixed layer to lose the heat gained during the summer [Markus et al., 2009].

Scientific questions

Since the albedo of sea ice, significantly increased by the snow cover, plays an important role for the shortwave energy balance of the Arctic atmosphere-ice-ocean system, it is important to thoroughly understand the ongoing physical processes that change the albedo in order to improve model predictions of the energy balance. Therefore, goals of this study are to acquire knowledge of the physical processes governing the reflectance of snow covered sea ice, and to quantify the variability each of these processes can cause. This will be approached by

- characterising the variability of the albedo of snow covered sea ice on a regional scale from airborne measurements, and by

- investigating the variability of the albedo of a snow cover due to changes of its microstructure and distribution of incident radiation with a radiative transfer model.

The Alfred Wegener Institute Helmholtz Centre for Polar and Marine Research (AWI) in Bremer-haven, Germany, has undertaken several airborne measurement campaigns evaluating, amongst other quantities, the surface albedo and sea-ice thickness in the Western Arctic. Aiming to identify the mean surface albedo and its variability on a regional scale, data from the PAMARCMiP (Polar Airborne Measurements and Arctic Regional Model Simulation Project) campaigns is investigated in this study. The quality and uncertainty of these albedo measurements has not yet been documented in depth, thence there is a need to quantify the measurement uncertainty of the specific instrument setup in order to judge which conclusions the accuracy allows to draw from the albedo measurements. Special problems airborne albedo measurements are facing include changes of the orientation of the sensors relative to the sun due the pitch and roll movement of the aeroplane and atmospheric influence on the measured radiation fluxes.

The large possible variability of a snow layer's reflectance has been demonstrated with model studies based on radiative transfer theory by Wiscombe and Warren [1980] and the studies reviewed in Warren [1982]. This variability can be induced by changes of the snow layer's microphysical parameters and depth and also aspects, like the angle of incident solar radiation and content of light absorbing impurities within the snow. In order to see which snow albedo changes can possibly be related to the measured variability, new model simulations are needed, focusing on the relevant range of these parameters, which is observed in the Arctic sea-ice area today. The model study aims to quantify the variability that realistically could occur for snow covered sea-ice.

Figure 1.1 demonstrates that sea ice shows surface heterogeneities of various scales. Thence, the interpretation of measured albedo time series might be ambiguous if no additional information about the surface conditions are available. It is therefore a goal to evaluate additional measurements parallel to the albedo measurements in order to characterise the influence of surface heterogeneities on a spatially averaged albedo. With this understanding, it could also be possible to bridge the gap between modelled spot measurements and measurements representative for a larger area. Spatial knowledge about the parameters with most influence on the albedo would enable a model to estimate the distribution of a spatially averaged albedo.

A further incentive of this study is to formulate and test a model, which is able to produce a sophisticated Arctic wide distribution of the sea-ice albedo in an approach that is coupled to a snow-albedo model via a look-up-table. The primary result of this model, a map of the sea-ice albedo, is already operationally derived from satelliteborne radiance measurements in the visible and near-infrared, e.g. by applying the algorithm by Xiong et al. [2002]. However, since the model, that is to be formulated here, will be coupled to a model describing the physical processes of surface reflectance, it can be used for further studies of these processes.

As a secondary result, the model can be used to evaluate regional differences in the additional energy deposition caused by a lowered surface albedo due to changes to the snow cover. A special interest lies in studying the impact of black carbon depositions in the snow cover. Additional light absorption impacts the shortwave radiation budget of the surface (surface forcing) and enhances further albedo degradation via the ice-albedo feedback, as mentioned above. Black carbon, also

known as *soot*, is a light absorbing aerosol that originates from the incomplete combustion of fossil fuels and biomass [AMAP, 2011]. It is transported into the Arctic via long range transport from lower latitudes in so-called events of *Arctic Haze* [Barrie, 1986] or emitted by human activities such as ship traffic and exploitation of natural resources inside the Arctic [AMAP, 2011]. The Assessment Reports of the IPCC (Intergovernmental Panel on Climate Change) name the effect of black carbon depositions on snow as a relevant contributor to global warming, but estimates of its radiative forcing still have a low confidence [Stocker et al., 2013].

Scope

This study will focus on evaluating the impact of black carbon depositions in snow on the shortwave radiation budget of the surface. Albeit, natural substances like dust also enhance the absorption of sunlight, most variability is expected from black carbon since rising atmospheric concentrations are reported in recent years [Stone et al., 2010]. Second to none, black carbon has a very strong ability to absorb solar radiation – the same mass of dust is about 200 times less absorbent than BC [Bond and Bergstrom, 2006, Gardner and Sharp, 2010].

All investigations in this study will focus on winter and early spring conditions. No melt processes will be taken into account, since all measurements from the PAMARCMiP campaigns were conducted before the onset of spring melt. Melting introduces further complex mechanisms that change the surface albedo [e. g. see the books of Thomas and Dieckmann, 2009, Wadhams, 2000]. The scope of this master thesis is limited by excluding wet snow and ice.

Methods and structure

In order to investigate influences on the reflectance of snow covered Arctic sea ice with a model based on the radiative transfer theory, an understanding of the modelling theory is needed. An introduction will be given in Sections 2.2 to 2.3, focusing on microphysical parameters of snow and the optical parameters that describe a snow layer in radiative transfer theory. There are different approaches to solve the radiative transfer equation and evaluate the reflectance of a snow surface. An overview on these approaches will be given in 2.5.

From the different possible model approaches, the discrete-ordinate method will be chosen, in order to not only describe the reflectance of a snow layer but also its optical interaction with the atmosphere via multiple reflections. This model approach also offers the possibility of atmospheric studies. Hence, there is a motivation to find and test a model approach that can be utilised in further studies of radiative transfer in snow covered regions. An appropriate model is described in Chapter 3. How the reflectance of a snowpack is influenced by varying snow microphysical parameters, atmospheric composition and incoming solar radiation is evaluated with a parameter study in Sections 3.2 and 3.3. It will be evaluated which parameters mostly determine the surface albedo and which possibly have rather minor influence. The plausibility of the obtained results with the model from this study is tested by a comparison to results from other models and field measurements in Section 3.4.

Chapter 4 investigates which information can be obtained from airborne albedo measurements and where the limitations of the accuracy are. Data from two campaigns (Section 4.1) focused on sea ice

in the Western Arctic are evaluated in Section 4.2. Representative flight legs are selected from the campaigns and the data are filtered. A graphical presentation of the measured broadband albedo along with auxiliary measurement data of surface parameters, described in Sections 4.3 and 4.4, is used to interpret the variability of the measured values along the flight tracks (Section 4.5). Based on this, influences of surface heterogeneities on a spatially averaged albedo are characterised.

As a combination of the findings from model study and evaluation of the campaign data, a model will be developed in Chapter 5, able to re-analyse the spatial distribution of the ice covered Arctic ocean's surface albedo. This model is then used to predict the surface forcing of an altered albedo as caused by the deposition of anthropogenic light absorbing substances onto the snow cover in Section 5.3.

A detailed overview of the state of knowledge is given at the beginning of every chapter and the chapters end with a summarising conclusion. Results of this thesis are discussed in Chapter 6.

2. Theoretical background

This chapter provides the theoretical background on the winter-time surface cover of the Arctic ocean. The sea ice that forms and the snow cover it often accumulates have distinct optical properties defining the reflection and absorption of solar radiation at the surface. First, the characteristics of sea ice and snow will be discussed in Sections 2.1 and 2.2. This will be followed by an introduction to the physical description of light propagation in small ice particles with help of the radiative transfer theory in Section 2.3, and with a focus on the reflectance of a snow or ice surface in Section 2.3.3. Finally, different modelling approaches for the reflectance, or the albedo, of snow covered sea ice will be introduced in Section 2.5.

2.1 The sea-ice cover of the Arctic Ocean

Sea ice is the ice that grows and melts within ocean waters. Since satellite multichannel passive microwave imaging systems became available in late 1978 it has been possible to monitor the entire extent of sea ice. The sea-ice cover in the Arctic varies between approximately $15.5 \times 10^6 \, \mathrm{km}^2$ in the winter and $6 \times 10^6 \, \mathrm{km}^2$ in the summer. This means that every year about $9.5 \times 10^6 \, \mathrm{km}^2$ of the Arctic sea ice melts away and freezes again [Meier et al., 2014]. Hence, much of the Arctic ocean is only seasonally ice covered. Figure 2.1 provides satellite derived spatial information on the sea-ice concentration and type that is provided by the EUMETSAT ocean and sea ice satellite application facility (OSI SAF)[1] and illustrates the distribution of the seasonal and multi-year sea ice in the Arctic ocean. Multi-year ice is ice that survived at least one summer melt period. Circulation patterns are the cause for this distribution – the general circulation of the Arctic ocean consists of a cyclonic gyre over the Canada Basin called Beaufort Gyre (BG), a strong flow of polar surface waters out of the basin on the west of Fram Strait from the Transpolar Drift (TD) and a strong flow of warm salty Atlantic Waters (AW) into the Arctic Basin on the east of Fram Strait and across the shallow Barents Sea [Carmack, 1990].

The freeze-up of the Arctic Ocean begins around October when the water temperature drops because the weakening of the solar radiation supplies less heat to the water body. The freezing point of ocean water with a salinity of 34 psu (practical salinity unit) is at -1.86°C Thomas and Dieckmann [2009]. Saline water freezes as crystals of fresh water, excluding the salt from its crystalline structure. Needle-like ice crystals (*frazil*) of about 3 to 4 mm form and accumulate at the surface. In calm

---

[1]http://osisaf.met.no/
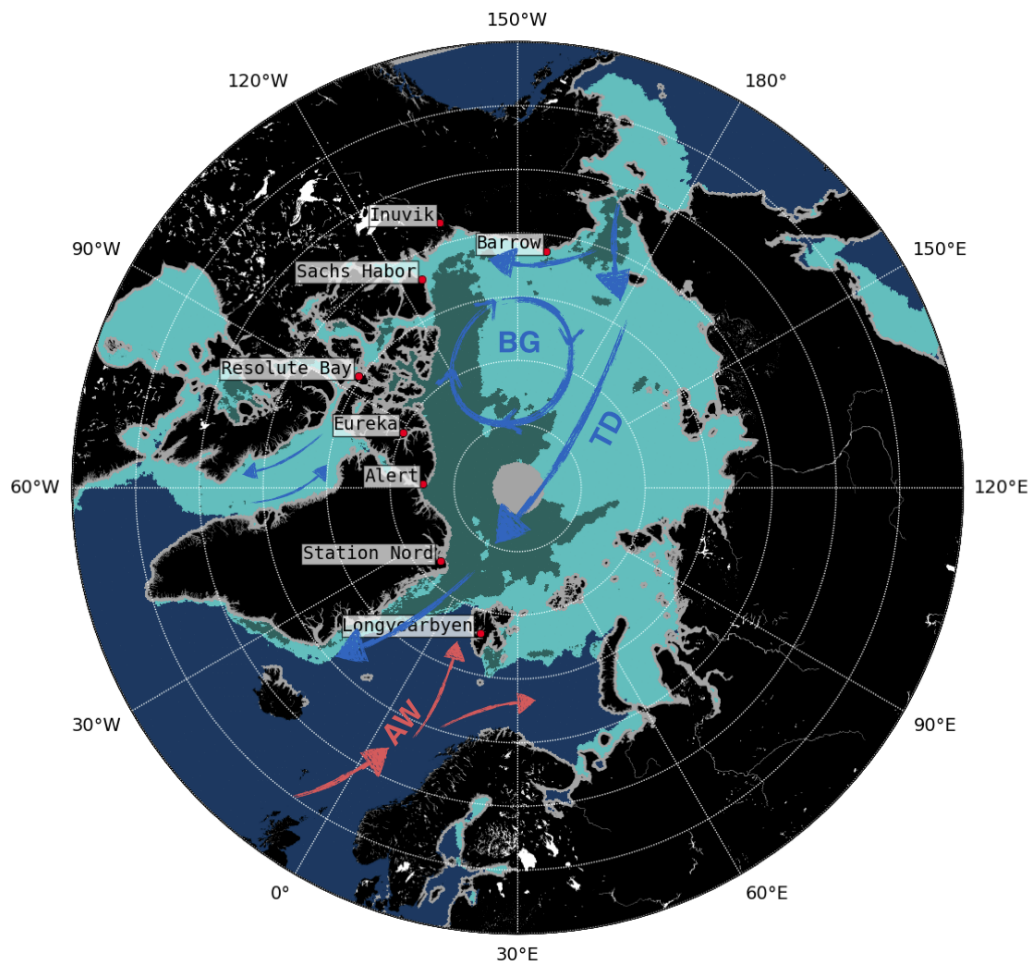
Figure 2.1: Sea-ice extend and type for 14. April 2011 based on a satellite product of the OSI SAF. The light turquoise areas are covered with seasonal sea ice and the darker aquamarine areas indicate sea ice that survived at least one summer. The ice distribution is influenced by cold currents (blue arrows) and inflowing Atlantic Water (red arrows). Note that grey areas mark where no data is available!

waters, frazil crystals form a smooth, thin cover on the ocean surface called *grease ice*. Over time, a continuous sheet of ice forms, called *nilas*, initially being thin and dark (dark nilas) and becoming lighter as it thickens. Wind often pushes the nilas around so layers of it slide on top of others, a process called rafting. This forms lighter bands within the ice. In rougher waters, however, the frazil crystals accumulate into smaller slushy floes, called *pancake ice* because of their shape. The pancakes typically have raised edges from collisions with other ice floes and are easily deformed because of their slushy structure. If the motion of the water is strong enough, rafting also occurs for pancakes. When the ice grows thicker and piles up on itself due to the motion, ridges form. After some hours to a few days, depending on the temperatures of ocean and air, pancake or grease ice consolidates and forms *sheet ice* that continues to grow. All this causes a rather complex stratigraphy of the ice compared to fresh water ice, e. g. on lakes.

Sea ice is very often covered with snow, but while sea ice only needs below-freezing water tem-

peratures to form, it needs three conditions to be met to form a snow cover: low temperatures, precipitation and an ice cover thick enough to support the fallen snow. The first heavy snow falls of the season take place in September [Warren et al., 1999] when mainly multi-year ice exists. Seasonal sea ice misses these snow fall events since it forms later in the season. Thence, often less snow accumulates on seasonal sea ice. But this is only a rule of thumb as the sea-ice cover can also influence the availability of moisture and precipitation. The wind and ocean current driven sea-ice dynamic often causes divergent motion which breaks up the ice. In some places open leads form that will refreeze after some time with thin, smooth ice and eventually will accumulate snow again. A discussion of the complex, heterogeneous surface structure of sea ice with a photograph of an example situation is found in Section 4.3.

A snow cover has strong thermodynamic influences on the sea ice. Yet, it is here only referenced to the discussion of the thermodynamic aspects in the book of Thomas and Dieckmann [2009] in order to focus on the optical properties of sea ice influencing the shortwave energy balance. The optical properties themselves are influenced by many parameters. Mentioned above, new ice changes its look from a darker grey to a lighter one as its thickness increases. Sea ice does not consist of a homogeneous ice volume that will appear clear and dark like lake ice, it rather has many inclusions of salty water (brine) and air. These inclusions scatter sunlight and thus less light is transmitted through the ice cover into the ocean. The light rather gets reflected from inside the ice volume back to the surface. Light scattering defines the reflectance of a medium and the concepts of light scattering in ice and snow will be discussed in greater detail in the following sections. As a result of increased back-scattering of sunlight, sea ice reflects about 50 to 70% of solar light compared to less than 10% for open ocean water (compare Figure 1.1) [Perovich et al., 1998]. A snow cover increases the ratio of reflected light, the albedo, to up to 90%, depending on its microphysical conditions [Perovich et al., 1998]. This microphysical properties along with fundamental optical principles relevant to both, snow and ice, will be introduced in the next sections.

2.2   Microphysical properties of snow

Snow is a complex, highly porous medium consisting of ice crystals and air, as well as, some impurities. Ice crystals form with highly variable microstructural shapes. A snowpack is composed of different types of grains in different layers. Ageing processes change the microstructure of single ice crystals and the stratigraphy of the snowpack as a whole. This section will introduce the microphysics of snow.

Snow crystals are single crystals of ice growing directly from water vapour in clouds. Although all ice crystals consist of water molecules arranged in a hexagonal lattice, snow crystals are often observed with elaborate, symmetrical patterns and, in general, complex structures. Their outstanding variety reflects the fact that many factors contribute to crystal growth, including both large-scale phenomena (e. g. particle and heat transport) and microscopic dynamics (e. g. surface diffusion and chemistry) [Libbrecht, 2005]. Nakaya [1954] was the first to categorize snow crystals formed under
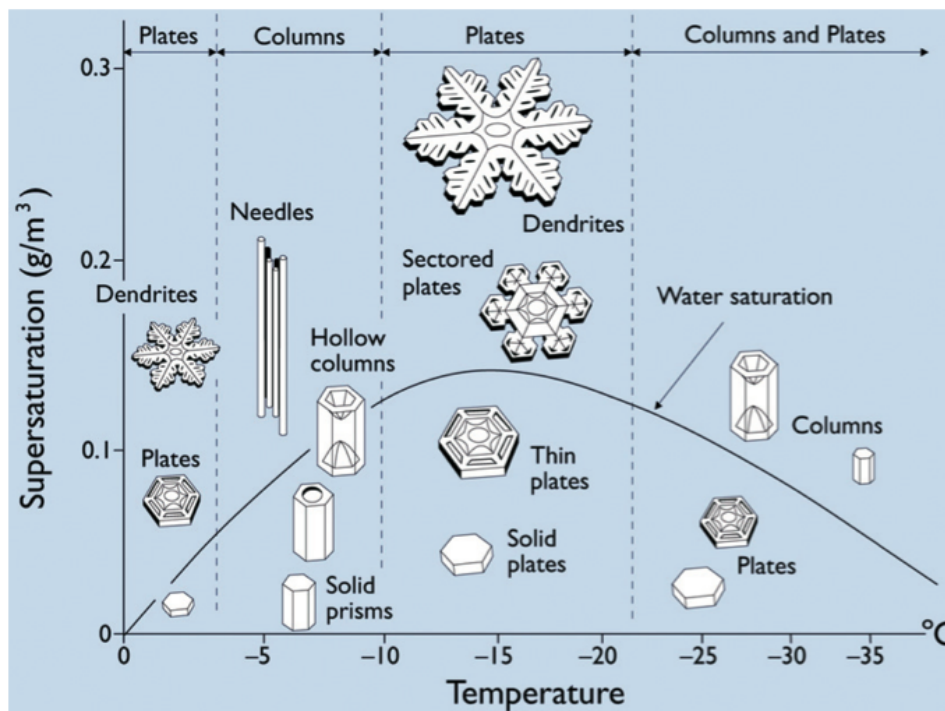
Figure 2.2: Snow crystal morphology diagram, showing different types of snow crystals that grow in air at atmospheric pressure, as a function of temperature and water vapour supersaturation relative to ice. The water saturation line gives the supersaturation of supercooled water, as might be found within a dense cloud. Note the morphology switches from plates ($T \approx -2°$ C) to columns ($T \approx -5°$ C) to plates ($T \approx -15°$ C) to predominantly columns ($T < -30°$ C) as temperature is decreased. Temperature mainly determines whether snow crystals will grow into plates or columns, while higher supersaturations produce more complex structures. This figure was adapted from a diagram in the paper of Libbrecht [2005], see references therein.

different meteorological conditions and also grew crystals in a controlled laboratory environment. The so-called snow crystal morphology diagram shown in Figure 2.2 is based on the ice crystals he observed for different temperature and saturation conditions. He found temperature and saturation relative to ice are the dominating factors controlling crystal shapes: temperature mainly controls whether the shape is more like a column or a plate, while supersaturation of water vapour relative to ice mainly controls the complexity of ice crystals [Nakaya, 1954].

Single *snowflakes* may cluster together and fall as precipitation to the ground. Snow on the ground is in a continuous state of transformation, known as snow metamorphism. It changes the shape and size of ice crystals due to the transport of water vapour in the direction of a pressure gradient. Such a water vapour pressure gradient can be caused only by the shape of crystals (Kelvin Effect) or by strong temperature gradients within a snow layer. Besides these two equi-temperature and temperature-gradient metamorphism processes also a melt-freeze cycle alters the shape of snow crystals [Colbeck, 1982].

Table 2.1: Evolution of snow from *The International Classification for Seasonal Snow on the Ground* [Fierz et al., 2009]. The symbols are for the in-situ observation and illustrate roughly the shape.

crystal	symbol	formation
rounded grains	●	small vertical temperature gradient ($< 10\,\mathrm{K/m}$)
faceted crystals	□	large vertical temperature gradient ($> 10\,\mathrm{K/m}$)
depth hoar	∧	later stage of large vertical temperature gradient
surface hoar	∨	water vapour from the atmosphere deposits onto the surface
rime	∀	later stage of large vertical temperature gradient
rain crust	=	freezing rain falls onto the snow surface forming a thin transparent glaze of ice
sun crust	−	sun melts the snow surface, refreezing forms a thin transparent glaze of ice
wind crust	∅	strong winds acting on the snow breaking up crystals and compacting the surface layer
melt-freeze crust	∞	air temperature oscillating around 0° C causes melting and refreezing

As this thesis is focused on winter and spring conditions with surface temperatures below the melting point, equi-temperature metamorphism is the most important process of the ones listed in Table 2.1. Equi-temperature metamorphism takes place in every snow layer, only more efficient at temperatures close to the melting point. It occurs when the vertical temperature slope in the snowpack is less than $10\,\mathrm{K/m}$. In these conditions, the ice at the convex surfaces of the crystal sublimes into water vapour which deposits on the concave surfaces. This leads to a rounding of the crystals (see Figure 2.3), as they want to reach a stable state by minimizing their surface free energy – which is smallest for spheres. Further, smaller ice crystals have a higher curvature than larger crystals. Thus, the water vapour pressure gradient permits a growth of larger snow crystals at the expanse of smaller ones. The diversity and complexity of new snow is lost after a few days to weeks [Flanner and Zender, 2006].

In typical Arctic conditions, the temperature gradient between the bottom of the snowpack (e. g. sea ice at about -2 to 0° C) and the top of it which is exposed to the cold atmosphere (about -10 to -30° C) may exceed $10\,\mathrm{K/m}$. Thence so-called temperature-gradient metamorphism can occur. The strong temperature gradient induces a water vapour saturation gradient which drives water vapour from warmer crystal surfaces to colder surfaces leading to a faceting of the crystals. The formation conditions of further snow crystal shapes are described in Table 2.1.

Due to the intermittent nature of precipitation, the wind redistributing and compacting the snow and the continuously ongoing metamorphism of ice crystals, a snowpack consists of multiple distinct layers of snow. Each layer may be, despite the grain shape and size, different in its density, hardness, temperature, liquid water and impurity content [Fierz et al., 2009]. Typical radii of snow
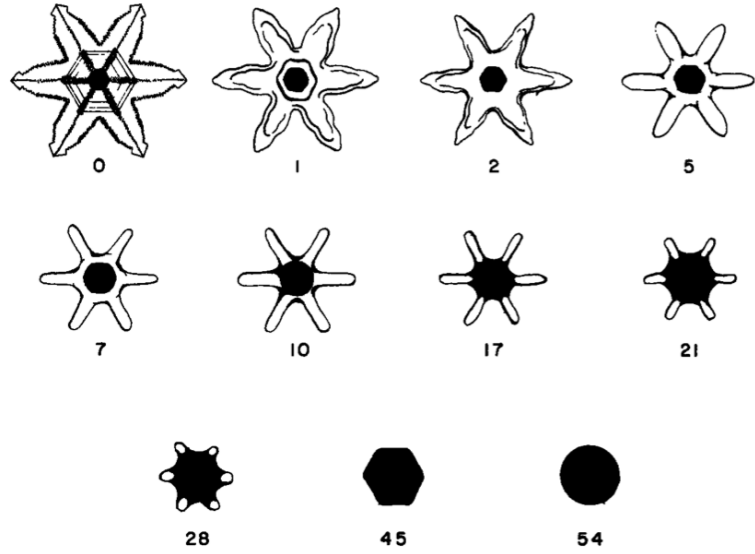
Figure 2.3: Decay of a snowflake to a spherical ice particle due to equi-temperature metamorphism over the course of 54 days. Taken from Colbeck [1982].

crystals range from below 0.1 mm for new snow to 0.5–1 mm for aged snow [Fierz et al., 2009]. The measurement, or estimation, of snow grain sizes is often difficult as grain shapes can be rather complex and reported values are often not sufficiently accurate for purposes of snow optics. There is a lack of standard procedures for field measurements, thus most estimates have a coarse resolution no better than 0.1 mm. The density of snowpacks ranges between $10 \, \text{kg/m}^3$ for fresh dendritic snow to $600 \, \text{kg/m}^3$ for hard wind-packed snow [Fierz et al., 2009]. Typical snowpack densities for snow on sea ice range between $200 \, \text{kg/m}^3$ and $400 \, \text{kg/m}^3$ [Domine et al., 2008, Warren et al., 1999].

A snowpack composed of complex non-spherical particles can be represented optically, regardless of the true shape, with spheres of effective radius r_{eff} [Grenfell and Warren, 1999]. This radius conserves the ratio of the mass M of snow crystals to the surface S of the ice-air interface of crystals in the snowpack. It is defined via the specific surface area (SSA), $\hat{S}$ of ice crystals [Legagneux et al., 2002]:

$$\hat{S} = \frac{S}{M} = \frac{S}{\rho_{\text{ice}} V} = \frac{4\pi r_{\text{eff}}^2}{\rho_{\text{ice}} \cdot 4/3 \pi r_{\text{eff}}^3} = \frac{3}{\rho_{\text{ice}} \cdot r_{\text{eff}}} \tag{2.1}$$

$$\Rightarrow r_{\text{eff}} = \frac{3}{\rho_{\text{ice}} \cdot \hat{S}} , \tag{2.2}$$

with V the volume of ice crystals and ρ_{ice} the density of ice with $917 \, \text{kg/m}^3$ at 0°C. While this theory is of less use when directional reflectance is an important consideration [e. g. Aoki et al., 2000, Painter and Dozier, 2004], it can be utilized for estimation of hemispheric reflectance and is adapted in many recent publications.

One description of the snow grain growth due to equi-temperature metamorphism was found by Legagneux et al. [2004], who gathered snow as it was falling. During their experiment, they kept the snow probe uniformly at -15° C, and observed the evolution of the effective grain radius by measuring methane adsorption. They provide a physical parametrization for the evolution of snow
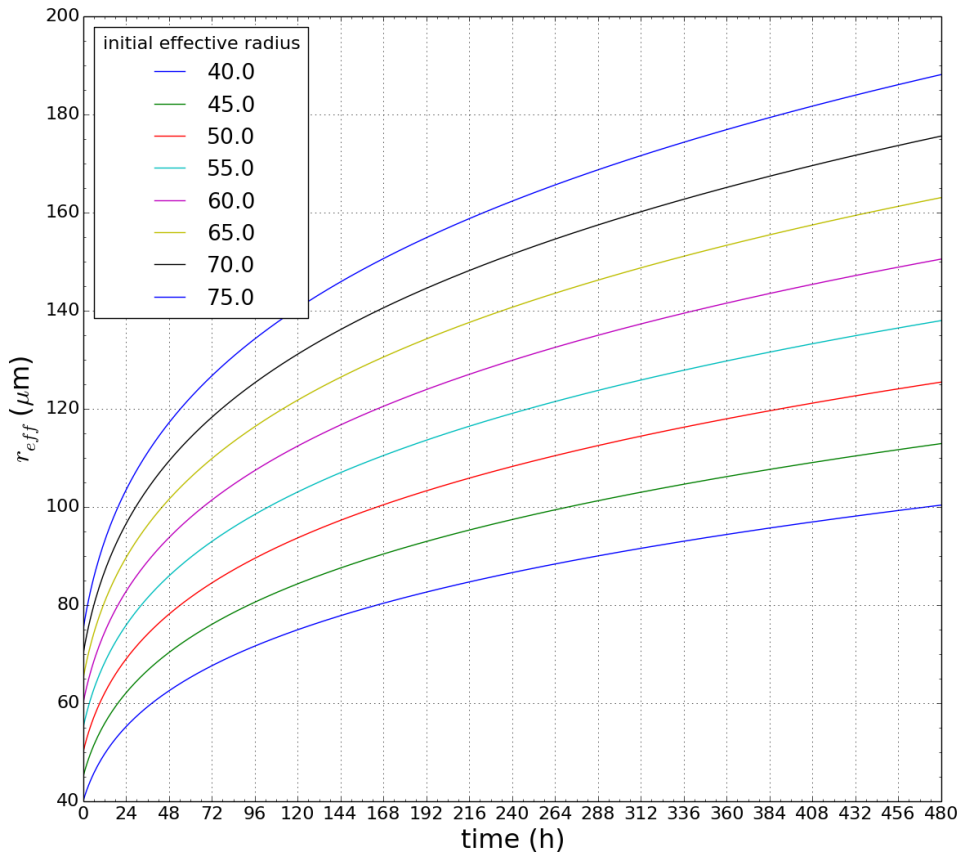
Figure 2.4: Snow grain effective radius (in ʈm) as a function of time – the equi-temperature
evolution of snow grain radius calculated with the parametrization (Equation 2.3) found by
Legagneux et al. [2004] during laboratory experiments with snow samples. The evolution
over the course of 21 days is plotted for 6 initial snow grain radii with values $\hat{t} = 7.1$ and
$\kappa = 4.1$.

grain size:

$$r_{\text{eff}} = r_{\text{eff},0} \left(\frac{\hat{t}}{\hat{t} + t} \right)^{-1/\kappa}, \tag{2.3}$$

where $r_{\text{eff},0}$ is the initial effective radius, t is the time and $\hat{t}$ and κ are empirical parameters. The
temporal evolution of snow grains with 6 different initial radii (Figure 2.4) shows a doubling of r_{eff}
after about 7–10 days. The importance of this parameter for the reflectance of a snow layer will be
discussed in Section 2.3 and 3.3.

2.3   Optical proberties of snow

A snow layer is not a reflecting surface. The reflectance of a snowpack is a result of light penetrating
into the snow volume and escaping from it again. The propagation of light within a snowpack

involves complex interactions of the radiation with many ice crystals. The wavelength dependent scattering and absorption processes for the propagation of light through single snow crystals are described in Section 2.3.1. The principles of geometrical optics and Mie-Theory are discussed. Within a snow layer it is very likely that light interacts with more than one scattering particle. The description of multiple scattering with the radiative transfer equation is discussed in Section 2.3.2 and yields a physical description of the reflectance of a snow layer.

The sedimentation of aerosols and pollutants from the atmosphere onto the snow surface introduces impurities of different optical properties to the snowpack. Some of these impurities have a strong ability to absorb light. These so-called light absorbing impurities (LAI) can significantly change the optical properties of a snow layer if they are present in a sufficient concentration. The optical properties of LAI found in snow on Arctic sea ice are discussed in Section 2.4.

2.3.1 Single scattering

Radiation, thought of as an electromagnetic (EM) wave or a photon, interacts with the medium it propagates through. In fact, this involves many interactions with single particles – the molecules of atmospheric gases and alien bodies, such as aerosols, water droplets and ice crystals. These particles cause scattering and absorption of radiation. The Maxwell Equations describe electromagnetic waves and their interactions. In this thesis, it shall only be referenced to the book of Hulst and Van De Hulst [1957] and other text books of modern physics for a detailed discussion of these equation in order to focus on the understanding of the optical properties of snow crystals and to find a mathematical/physical description allowing for a quick and robust calculation of these properties.

Geometrical optics can be applied to ice crystals as they are rather large compared to the wavelengths λ of solar light [Hulst and Van De Hulst, 1957]. The size parameter $x = 2\pi r/\lambda$ is in the range of about 500 to 2000 for snow crystals of radii between 50 and 200 µm, respectively. A sketch of the propagation of a narrow beam of light through a spherical ice crystal (Figure 2.5) shows that the scattering process involves a splitting of the beam by multiple reflections at boundaries between air and ice (e.g. media with different refractive indices) and refraction.

On the path of the light beam through the solid medium, interaction of the EM wave with ice molecules absorb energy. The refractive index $n = m - im'$ (Figure 2.6) describes the properties of the medium causing refraction and absorption. The refractive index is a function of wavelength and also temperature and state of aggregation of the medium. Its real part describes the phenomena of dispersion while the imaginary part describes the decrease in intensity (see Hulst and Van De Hulst [1957] for more details). The imaginary part of the refractive index of ice, as reported by Warren and Brandt [2008], shows a strong increase from the order of 10^{-9} around 500 nm to 10^{-4} around 2200 nm with local maxima around 1000, 1500 and 2000 nm (Figure 2.6).

Extinction of a beam of radiation caused by the interaction with a particle consists of absorption and scattering. Both are a function of the size and shape of the particle with given refractive
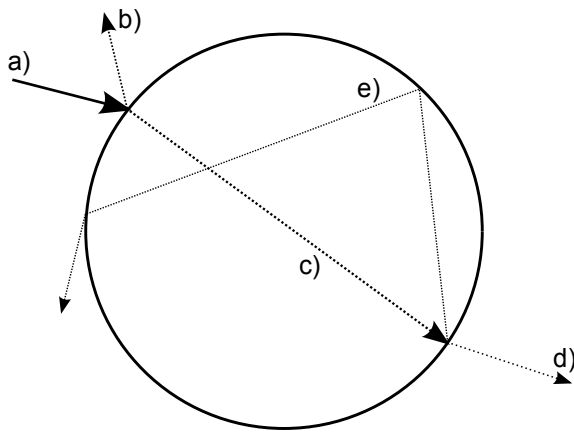
Figure 2.5: Propagation of an incoming beam of light through a spherical ice particle sketched according to the principles of geometrical optics. The incoming beam a) is reflected b) and refracted at the ice-air boundary. Within the ice, absorption takes place proportional to the path length c) at the other ice-air boundary, again refraction d) and reflection takes place. A part of the light is reflected multiple times within the ice particle e). The results of the scattering process are direction changes and extinction of the beam of light.

index. As indicated in Figure 2.5, scattering involves a directionality and a probability of how much radiation leaves the particle under a certain angle ψ_{s} relative to the incident beam of radiation. The directionality is described with the phase function $p(\psi_{\text{s}})$. A measure of the efficiencies of absorption and scattering are the respective cross sections $\sigma_{\text{a}}(\lambda)$ and $\sigma_{\text{s}}(\lambda)$. The sum of absorption and scattering is extinction of the beam, $\sigma_{\text{e}}(\lambda)$ and the ratio

$$\omega(\lambda) = \frac{\sigma_{\text{s}}(\lambda)}{\sigma_{\text{a}}(\lambda) + \sigma_{\text{s}}(\lambda)} = \frac{\sigma_{\text{s}}(\lambda)}{\sigma_{\text{e}}(\lambda)} \tag{2.4}$$

is the single scattering albedo, a measure of how much energy is absorbed within the particle and how much is redistributed through scattering. Theses cross sections and the single scattering albedo can be obtained by applying geometrical optics to an ice particle. This is often done in a ray tracing approach by calculating the paths of an ensemble of rays, e. g. beams of light, through the particle.

Since snow rapidly transforms from dendrites and hexagonal crystals into a more spherical shape, as argued in Section 2.2, also Mie-Theory (after Gustav Mie and Ludvig Lorenz) can be applied. Gustav Mie applied Maxwell's equations to the case of an incident plane EM wave scattered by a sphere in 1908. The equations he derived can be used to obtain the optical properties of independently scattering ice particles. The derivation of these equations can be found in great detail in the book of Kokhanovsky [2006], chapter 2. Figure 2.7 shows the phase function of a water droplet of a radius $r = 100\,\mu\text{m}$ calculated with MiePlot[2] v4.3, a program based on the algorithm proposed in the book of Bohren and Huffman [2008] for calculations of the optical properties of spherical particles according to the Mie-Theory (called *Mie calculations* in the following). Note that water has a refractive index very similar to ice with only a marginal wavelength shift [Kou et al., 1993].

The calculated phase function (Figure 2.7) reveals a strong forward scattering of visible light at water/ice particles of this size. Often, this main direction of scattering is expressed with the

---

[2]MiePlot is available for download at http://www.philiplaven.com/mieplot.htm, last updated January 2014
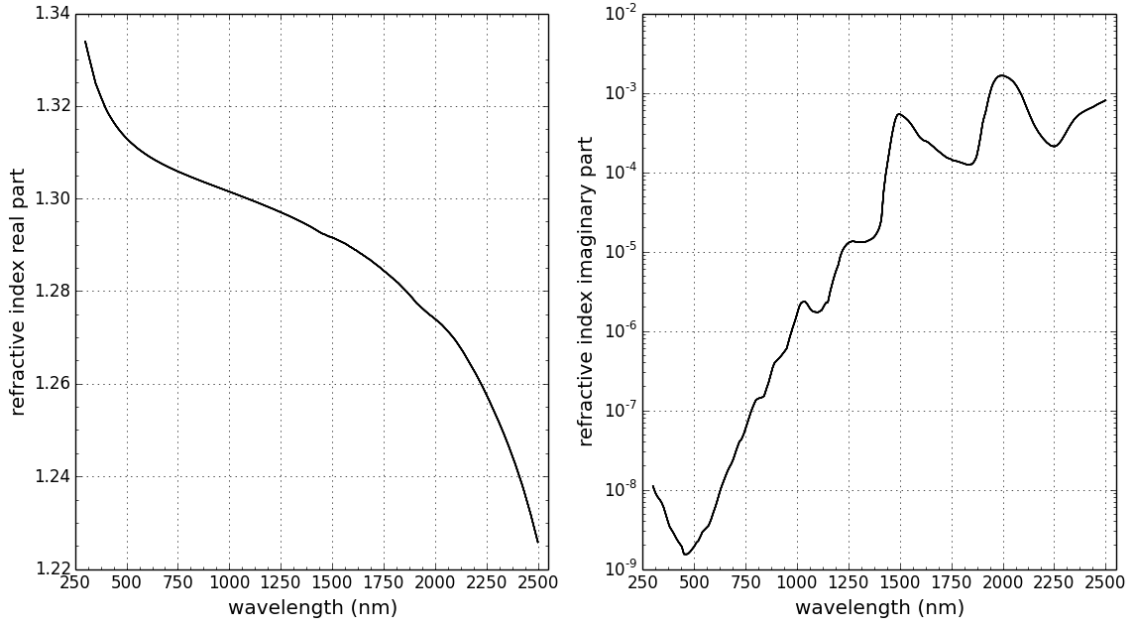
Figure 2.6: Real part m (left) and imaginary part m' (right) of the refractive index of ice, plotted with data from Warren and Brandt [2008] as a function of wavelength (in nm). Notable is the strong increase of m' from the visible to near-infrared light in this semi-logarithmic plot.

asymmetry parameter

$$g(\lambda) = \int_{\Omega} p(\lambda, \Omega) \cos(\theta) d\Omega = \int_{0}^{2\pi} \int_{0}^{\pi} p(\lambda, \theta, \varphi) \cos(\theta) \sin(\theta) d\theta d\varphi \,, \qquad (2.5)$$

which is the phase function $p(\lambda, \theta, \varphi)$ integrated over all solid angles $d\Omega = \sin(\theta) d\theta d\varphi$, e.g. a sphere described with zenith angles θ and azimuth angles φ. It approaches 1 if forward scattering is favoured and -1 if backscattering is favoured. An asymmetry parameter around 0 would be reached for isotropic scattering. Single scattering albedo and asymmetry parameter for spherical ice particles of various radii, representing particles with certain effective radii (Equation 2.2), were calculated with the MIE0 algorithm for Mie-Scattering by Wiscombe [1980] and are shown in Figure 2.8. The single scattering albedo represents the behaviour of the imaginary part of the refractive index (see Figure 2.6) with almost solely scattering occurring below 1000 nm and absorption becoming important for wavelength greater than 1000 nm. Similarly, g shows that forward scattering increases for longer wavelength and both absorption and forward scattering increase with increasing grain size. The mono-disperse Mie-calculation exhibits so-called *ripple effects* that are not observed in natural media containing a range of particle sizes. Averaging the calculated Mie values over a size distribution would smooth the curves shown in Figure 2.8.

The tracing of rays reflected and refracted at the surface of a scatterer according to the laws of geometrical optics can be applied to particles of all shapes. Mie-theory, however, yields accurate results for spherical particles and all particles that can be treated as such. Its equations have been
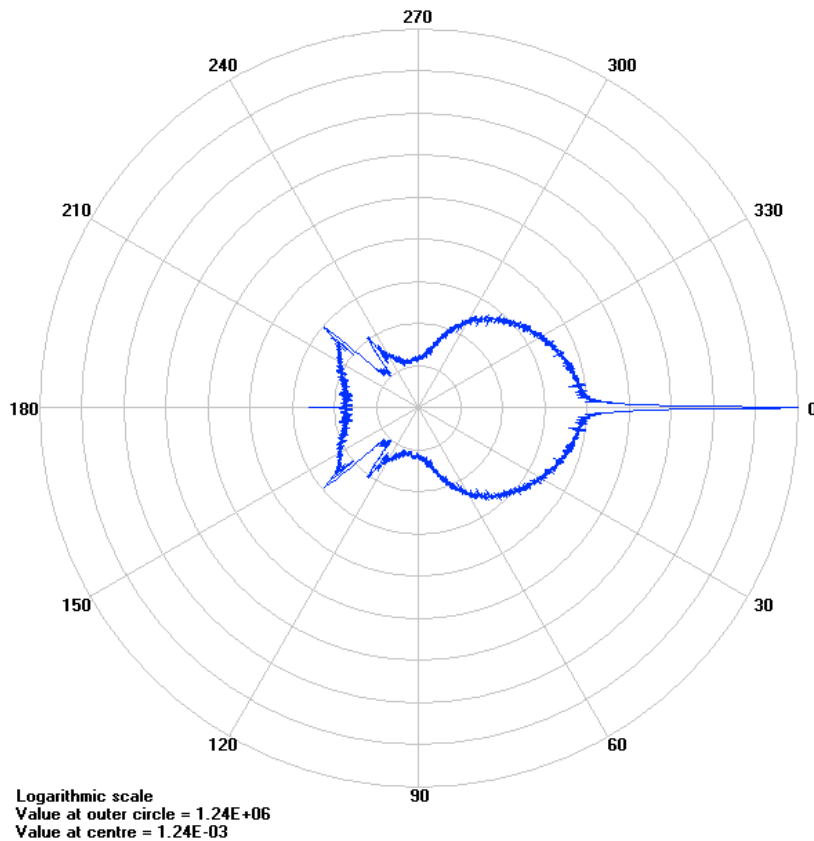
Figure 2.7: Phase function of a water drop of radius 100 µm for blue light (450 nm) visu-
alized as a polar plot of the scattering angle. Note the logarithmic scale (from the centre
outwards) indicating that much more energy per unit solid angle is scattered into the forward
direction. Illumination was realized with parallel, monochromatic, unpolarised sunlight. The
calculations and plot were performed with MiePlot.

implemented in algorithms and can be solved very fast numerically [Wiscombe, 1980]. Full ray
tracing or deterministic Monte-Carlo approaches need more computational effort and the knowledge
of snow crystal shape and size. Because in most cases the shape of crystals is in most cases unknown
or too diverse, one looks for a description of the optical properties that is independent of the
geometrical form. One possibility is the discussed approach to treat all crystals as spheres with the
respective SSA or r_{eff}.

2.3.2   Multiple scattering

Every scattering event of a photon at an air-ice interface is an opportunity to escape the snowpack
due to a change in direction of propagation. But the longer the path length within the ice, the
higher is absorption of energy [Warren, 1982]. Most of the light emerging from a snow surface
has been scattered by multiple snow crystals successively, hence the intensity of the reflected
light is not proportional to the number of scattering particles within the snow layer. Particles

Figure 2.8: Single scattering albedo ω (left) and asymmetry parameter g (right) as a function of wavelength (in nm). The values were calculated for spherical ice crystals of various radii with the MIE0 algorithm. The values are not averaged over a size distribution, therefore especially g shows a ripple pattern.

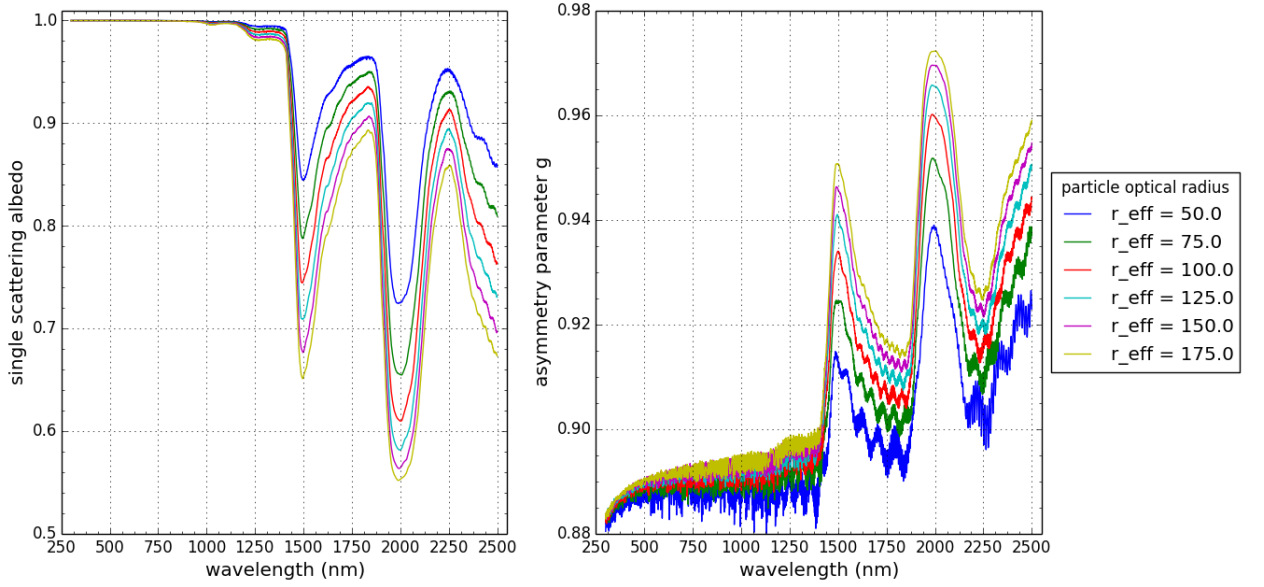scattering light towards the surface may be illuminated by other scattering particles rather than by the direct light source. Finding the intensities of light inside and outside a scattering layer is a complex problem, its solution is usually known as radiative transfer theory. The radiative transfer equation (RTE) describes the change of radiance $L(\lambda)$ as radiation passes through a volume of certain optical properties. In the following, the RTE will be introduced as described in the book of Kidder and Haar [1995] without the consideration of polarization and also without thermal emission, which is not relevant in the wavelength range of visible (VIS) and near-infrared (NIR) light. The RTE describes the change of $L(\lambda)$ with distance s:

$$\frac{dL(\lambda)}{ds} = A + B + C \, . \tag{2.6}$$

The three terms stand for

A: radiation from the beam absorbed by the material,

B: radiation scattered out of the beam into other directions and

C: radiation from other directions scattered into the beam.

The depletion terms A and B have the form $A = -\sigma_a(\lambda)L(\lambda)$ and $B = -\sigma_s(\lambda)L(\lambda)$ and can be combined to $-\sigma_e(\lambda)L(\lambda)$ using $\sigma_e = \sigma_a + \sigma_s$. The source term C is more complicated as all directions must be considered:

$$C = \frac{\sigma_s(\lambda)}{4\pi} \int_0^{2\pi} \int_0^{\pi} L(\lambda, \theta', \varphi') P(\lambda, \theta, \varphi, \theta', \varphi') \sin(\theta') d\theta' d\varphi' \, . \tag{2.7}$$

The phase function $P(\lambda, \theta, \varphi, \theta', \varphi')$, when multiplied with $\omega(\lambda)$, gives the probability that radiance from a direction given by (θ', φ') will be scattered into direction (θ, φ). The phase function is rather

complex, as the example in Figure 2.7 indicates, and is often approximated as a function of the asymmetry parameter g (Equation 2.5).

The path length s in Equation 2.6 can be substituted for the vertical optical depth τ along the slant path:

$$\tau(\lambda) = \int_{s_1}^{s_2} \sigma_{\mathrm{e}}(\lambda)\mu ds \,, \tag{2.8}$$

$$\Leftrightarrow ds = \frac{1}{\mu\sigma_{\mathrm{e}}(\lambda)}d\tau(\lambda) \,, \tag{2.9}$$

with $\mu = \cos(\theta)$. In this form, the change of radiance L along the slant path can be expressed in terms of the optical properties of the medium it passes trough. Using Equation 2.4, the RTE becomes:

$$\mu\frac{dL(\lambda)}{d\tau(\lambda)} = -L(\lambda,\theta,\varphi) + \overbrace{\frac{\omega(\lambda)}{4\pi}\int_0^{2\pi}\int_0^{\pi} L(\lambda,\theta',\varphi')P(\lambda,\theta,\varphi,\theta',\varphi')\sin(\theta')d\theta'd\varphi'}^{\text{term C}} \,. \tag{2.10}$$

Equation 2.10 has to be solved in order to evaluate the radiation that is reflected from the snow volume back into the hemisphere above.

2.3.3   Surface reflectance

The term *reflectance* implies the possibility that the incident radiation is partly reflected from, but also partly transmitted through, the snowpack or absorbed within it. A snow layer has a finite physical thickness z_{snow}. Its optical thickness is defined as [Wiscombe and Warren, 1980]:

$$\tau_{\mathrm{snow}}(\lambda) = \frac{3}{4\pi}\frac{\sigma_{\mathrm{e}}(\lambda)\rho_{\mathrm{snow}}z_{\mathrm{snow}}}{\rho_{\mathrm{ice}}r_{\mathrm{eff}}^3} = \frac{3}{4}\frac{Q_{\mathrm{e}}(\lambda)\rho_{\mathrm{snow}}z_{\mathrm{snow}}}{\rho_{\mathrm{ice}}r_{\mathrm{eff}}} \,, \tag{2.11}$$

with ρ_{snow} being the density of the snowpack. The optical thickness is wavelength dependent since the extinction efficiency $Q_{\mathrm{e}}(\lambda) = \sigma_{\mathrm{e}}(\lambda)/(\pi r_{\mathrm{eff}}^2)$ varies considerably over the spectrum (Figure 2.8). It is likely that the same snowpack is partly translucent for VIS light while it is opaque in the NIR. Hence, a low optical thickness means that the reflected light measured above a snowpack is also influenced by the subjacent ground. One speaks of a semi-infinite optical thickness if an increase of the physical thickness of a snow layer no longer influences the reflected irradiance. An evaluation of this effect can be found in Section 3.3.

The most frequently used reflection quantity is the spectral hemispheric reflectance, or albedo, that is defined in this study following the book of Kidder and Haar [1995] as:

$$\alpha(\lambda) = \frac{E^{\uparrow}(\lambda)}{E^{\downarrow}(\lambda)} \,. \tag{2.12}$$

It describes the shortwave ($280 \leq \lambda \leq 2500\,\mathrm{nm}$) energy balance of a surface as the ratio of reflected ($E^{\uparrow}(\lambda)$) to incident ($E^{\downarrow}(\lambda)$) radiation. The albedo can be expressed as a broadband quantity by

integrating over the solar spectrum:

$$\alpha = \frac{\int_\lambda E^\uparrow(\lambda)d\lambda}{\int_\lambda E^\downarrow(\lambda)d\lambda}\,. \tag{2.13}$$

Here $E^\downarrow(\lambda)$ and $E^\uparrow(\lambda)$ stand for the incoming (i) and reflected (r) irradiance that can be calculated from the respective radiance L_i and L_r by an integration over the upper, or respective, lower hemisphere:

$$E^\downarrow(\lambda) = \int_0^{2\pi}\int_0^{\pi/2} L_i(\lambda,\theta_i,\varphi_i)\cos(\theta_i)\sin(\theta_i)d\theta_i d\varphi_i \tag{2.14}$$

$$E^\uparrow(\lambda) = \int_0^{2\pi}\int_0^{\pi/2} L_r(\lambda,\theta_r,\varphi_r)\cos(\theta_r)\sin(\theta_r)d\theta_r d\varphi_r\,. \tag{2.15}$$

The evaluation of the albedo of a surface is based on the principle of measuring the spectral or broadband irradiance from the lower and upper hemisphere, e. g. the reflected and incoming solar irradiance, and divide both measurements according to the definition given above (equations 2.12 or 2.13). Most commonly two hemispheric receivers with cosine weighting are used or one such receiver is turned to look upward and downward. Setups with two pyranometers are frequently used for broadband measurements in order to obtain the energy budget of a surface integrated over the whole solar spectrum. Because of its characteristic wavelength dependence, snow albedo is often measured with spectroradiometers. One example for spectral albedo measurements will be given in Section 3 and broadband measurements with pyranometers mounted on an aeroplane will be discussed in Section 4. Despite the principle of this measurement being relatively simple, large uncertainties can arise – see the discussion in Section 4.2.4.

2.4 Light absorbing impurities in snow

Kumai [1976] studied samples of snow grains under a microscope and found varying numbers of former aerosols in the them. The number of impurities in the snow corresponds to the typical atmospheric concentrations of aerosols in the different regions the samples originated from. Kumai [1976] could therefore infer that snow flakes have a collection efficiency of about unity when falling from around $500\,\mathrm{m}$ and sweeping up aerosols in their path. Another, less efficient, mechanism of aerosol deposition to the ground is sedimentation.

Among these impurities introduced to the snowpack can be particles from different types and classes of aerosols. Interesting for the following discussion are aerosols that absorb light. Those aerosols, if introduced to the snowpack as light absorbing impurities (LAI) in sufficient concentration C_{LAI}, enhance the absorption of light within the snowpack. Second to none, black carbon (BC), an anthropogenic pollutant originating from the incomplete combustion of fossil fuels and biomass burning, has a very strong ability to absorb light in the UV and VIS. BC absorbs much stronger (relative to mass) than other common LAI like brown carbon and dust [Bond et al., 2013]. The impact of BC to the Arctic climate system is further discussed in Sections 3 and 5.

In order to model concentrations of light absorbing BC within a snowpack, its optical properties have to be known. These properties be calculated according to the Mie-Theory with the spectrally uniform refractive index suggested by Bond and Bergstrom [2006] (n = 1.95 + 0.79i) the effective radius suggested by Hansen and Nazarenko [2004] (0.1 µm) and a mean density of $1.8\,\mathrm{g/cm^3}$ [Bond and Bergstrom, 2006]. For BC in snow, there are large uncertainties regarding the absorptive properties, because typical ratios between internally mixed (particles residing within the ice grains) and externally mixed (particles located outside the ice gains) carbon particles in Arctic snow are not well known. Further, BC particle densities, sizes, and refractive indices vary with production source and residence time in the atmosphere [Bond and Bergstrom, 2006]. Ageing of aerosol layers containing BC often leads to complex coagulations and a coating of carbon particles with non-carbonaceous substances such as sulphur. The typical mass specific absorption cross section (MAC) for fresh atmospheric BC is about $7.5\,\mathrm{m^2/g}$ [Bond and Bergstrom, 2006] and is nearly constant for visible wavelengths and decreases towards longer wavelength [Gardner and Sharp, 2010]. For aged, coated BC particles an enhancement of the MAC by a factor of 1.5 is suggested by Bond et al. [2006]. Most of these pollutants are transported to the Arctic over long distances from Europe and Asia [Barrie, 1986] and have an atmospheric lifetime allowing for these ageing processes, hence an enhancement of the absorption capabilities of Arctic BC is likely.

2.5 State of the art: Modelling approaches

This section especially discusses models that use different approaches to solve the RTE. Some of these models are designed to make the problem feasible for the available computational resources and others to match special use cases as, for example, retrieval algorithms for satellite data. The discussed models simulate the reflectance of a snowpack of known snow layer microstructure (stratigraphy).

2.5.1 Two-stream approximation based models

The greatest advances in the field of snow-albedo modelling have been achieved by the work of Wiscombe and Warren [1980]. Their model utilises the two-stream solution of the RTE with Delta-Eddington approximation for the phase function. It yields a set of equations for the diffuse and direct hemispheric reflectance of a snow layer only depending on the SZA and the optical properties ω, σ_e and g. These properties are obtained from Mie-calculations. Their model is not directly coupled to atmospheric radiative transfer. Diffuse and direct albedo are combined to the resulting surface albedo $\alpha = R \cdot \alpha_\mathrm{dif} + (1 - R) \cdot \alpha_\mathrm{dir}$ with the factor R, the ratio of diffuse to total (diffuse plus direct) incident radiation fluxes. This ratio depends on the specific atmospheric conditions and has to be evaluated by an external model or obtained from measurements. Warren and Wiscombe [1980] investigated the influence of LAI on the spectral albedo by accounting for the additional absorption in the calculation of the optical single scattering properties.

One example for an implementation of the model by Wiscombe and Warren [1980] is the Snow, Ice, and Aerosol Radiative (SNICAR) model [Flanner and Zender, 2005]. SNICAR is a multilayer

radiative transfer model of a snowpack that depends on vertically resolved effective radius, snow depth and density and concentrations of absorbing impurities. Furthermore, the ratio of diffuse to direct incident radiation and bare surface reflectance have to be defined as boundary conditions. SNICAR assumes direct and diffuse incident fluxes that are typical for standard mid-latitude or summit of Greenland winter atmospheres [Flanner et al., 2007]. There is also a single-layer version of this model, SNICAR-Online[3] [Flanner et al., 2007]. This model can be accessed via a web interface, hence it runs with a tested setup and configuration and should produce reliable results. Various versions of SNICAR have been used for publications in recent years. Flanner and Zender [2005] and Flanner et al. [2009] use implementations of the code in general circulation models (GCM).

Also, the model TARTES (Two-streAm Radiative TransfEr in Snow) makes use of the two-stream solution with Delta-Eddington approximation. However, it is unique in the aspect that this model is not utilising Mie-Theory. TARTES is based on the formalism for weakly absorbing media by Kokhanovsky and Zege [2004] to describe the single scattering properties of each layer. TARTES has been initially developed to investigate the influence of the particle shape on the reflectance of a snowpack [Libois et al., 2014, 2013]. TARTES represents the snowpack as a stack of horizontal homogeneous layers. Each layer is characterized by the SSA or effective radius of snow grains, snow density, impurity amount and type. Furthermore, there are two parameters for the geometric grain shape: the asymmetry factor g and the absorption enhancement parameter B. See the publications of Kokhanovsky and Zege [2004] and Libois et al. [2013] for more details on these parameters. The albedo of the bottom interface can be prescribed. The model is accurate in the VIS and NIR for pure snow, as well as for snow containing impurities [Libois et al., 2013]. LAI are represented as Rayleigh scatterers. TARTES has been released as an open source software package (under a GPL license) in October 2014 as initial release version 0.9. The model is written in Python and is distributed via a website of the LGGE[4] (Laboratoire de Glaciologie et Géophysique de l'Environnement).

2.5.2 Discrete ordinate method based models

More elaborate models use the discrete-ordinate (DISORT) method by Stamnes et al. [1988] to solve the RTE for a succession of plane-parallel layers of media with different optical properties. Today, DISORT is frequently used in atmospheric science, astronomy and other fields related to transfer of radiation through optical media. It offers the possibility to calculate direct and diffuse irradiance and radiance with multiple streams. It is possible to couple atmospheric radiative transfer with that in snowpacks, which makes this type of model capable of different use cases. On the one hand, the reflectance of a snowpack can be calculated with accurate representation of diffuse multiple reflections between the snow and the atmosphere. On the other hand, a realistic snowpack can be implemented to a model setup in order to calculate atmospheric radiation parameters, e.g. while re-simulating measurements conducted during winter conditions. Further, utilising

---

[3]SNICAR-Online is available at: http://snow.engin.umich.edu
[4]TARTES is available at: http://lgge.osug.fr/ picard/tartes/

the multiple streams of radiance from different directions, DISORT permits the calculation of a bidirectional reflectance distribution function (BRDF) of snow layers (e. g. Aoki et al. [2000]) if an accurate representation of the phase function is used. DISORT can use approximations of the phase function such as the one formulated by Henyey and Greenstein [1941] or more accurate formulations obtained from Mie calculations or geometrical optics.

For DISORT based radiative transfer, there are no stand alone models like TARTES available with the purpose to calculate the surface albedo of snowpacks. A layer of a DISORT model are set up by defining its single scattering properties and optical thickness. This has to be done for all layers of the optical media which the radiation is penetrating. This includes the atmospheric layers as well as one or multiple layers of snow above the bottom boundary of the model domain.

Several available radiative transfer software distributions of the DISORT code by Stamnes et al. [1988] come with libraries for atmospheric constituents like gases, cloud particles and aerosols. Properties from these libraries may be used to set up the model with an atmosphere and a snowpack. It is also possible, or even necessary, to calculate these optical properties, e. g. for snow containing LAI.

Amongst others, Dumont et al. [2010] use a DISORT model to calculate the spectral albedo of a multiple layer snowpack in order to reproduce their field measurements at Dome C, Antarctica. Gardner and Sharp [2010] calculate the spectral albedo of snow on top of sea ice. Both studies calculate the optical properties of the snow according to the Mie-theory. Marks and King [2013] utilise a DISORT model to calculate the spectral albedo of different types of bare sea ice and sea ice with a snow cover. All three studies feature investigations on the effects of LAI. Xiong et al. [2002] retrieve surface albedo from satellite measurements with the AVHRR (Advanced Very High Resolution Radiometer) instrument (see Section 5.3). A DISORT based model will also be featured in the parameter study in Chapter 3.

2.5.3 Asymptotic solution of the RTE for thick snowpacks

Kokhanovsky and Zege [2004] proposed an asymptotic solution of the RTE adapted to an optically infinite thick snow layer that analytically solves the problem of snow reflectance. This model uses the same approximation of the single scattering properties of snow grains used in TARTES. The following formulation of their equations handles any incident angle θ:

$$\alpha''(\lambda) = \exp\left(-A\sqrt{\gamma(\lambda)\,r_{\text{eff}}}\,\frac{3}{7}(1 + 2\cos(\theta))\right),\tag{2.16}$$

where γ is the ice absorption coefficient calculated from the imaginary part of the refractive index $n'(\lambda)$. This coefficient also accounts for concentrations of BC:

$$\gamma(\lambda) = \frac{4\pi}{\lambda}(m'(\lambda) + 0.2\cdot C_{\text{BC}}\cdot 10^{-9}),\tag{2.17}$$

with λ in nanometres and C_{BC} in ppbw. This description of the optical properties is independent of the geometrical form of the snow crystals. The parameter A accounts for the dependence of the phase function on grain shape. It is empirically determined as $A \approx 6.4$ for spherical ice particles and $A \approx 5.8$ for tetrahedral fractal grains [Zege et al., 2011]. Picard et al. [2009] verified the

equations of Kokhanovsky and Zege [2004] with their ray tracing model (see below) as it shows the same behaviour of the albedo at 1310 nm with increasing size of complex shaped crystals (cubes and tetrahedral fractal grains), as shown in their figure 5c. The demonstrated good agreement makes this simple solution attractive for many scientific purposes as it may be used in a retrieval algorithm for the effective radius of snow grains even if their shape is complex. The set of equations needs low computational effort. Unfortunately, the asymptotic solution is also very restricted to the assumptions that were made. It can only be applied for optically thick snow layers being homogeneous in grain size and shape. This condition is often not met by real snow covers – see an example for snow on sea ice discussed in section 3.3 where the approach by Kokhanovsky and Zege [2004] might produce inappropriate results. The representation of multiple layers with different optical properties is a strength of the DISORT or two-stream methods.

2.5.4 A physically based parametrisation

Gardner and Sharp [2010] provide a parametrisation for the broadband albedo of snow or ice depending on the specific surface area (SSA), $\hat{S}$, of snow grains (related to the effective radius via Equation 2.2). Furthermore, BC content in snow, SZA and cloud optical thickness are parameters influencing the parametrised broadband albedo. The parametrisation is based on a statistical analysis of calculations with their DISORT and BHMIE based snow-albedo model. Their equations are briefly summarised in the following and will be evaluated in Section 3.3.

The broadband albedo is parametrised with a simple asymptotic function:

$$\alpha'_{\hat{S}} = 1.48 - \hat{S}^{-0.07}.$$
(2.18)

The change of broadband albedo due to a concentration C_{BC} of BC in snow measured in ppmw is expressed as:

$$d\alpha'_c = \max\left(0.04 - \alpha'_{\hat{S}}, \frac{-C_{\mathrm{BC}}^{0.55}}{0.16 + 0.6\hat{S}^{0.5} + 1.8c^{0.6}\hat{S}^{-0.25}}\right).$$
(2.19)

The influence of the SZA is expressed as:

$$d\alpha'_\theta = 0.53\alpha'_{\hat{S}}(1 - \alpha'_c)(1 - (0.64\chi + (1 - \chi)\cos(\theta))^{1.2},$$
(2.20)

where $\chi = \min\left(\frac{\tau_{\mathrm{cloud}}}{3\cos(\theta)}^{0.5}, 1\right)$. Finally the increasing effect of the cloud optical thickness τ_{cloud} on the spectrally integrated albedo by shifting the spectrum of the incident radiation is:

$$d\alpha'_\tau = \frac{0.1\tau_{\mathrm{cloud}}(d\alpha'_c + \alpha'_{\hat{S}})^{1.3\,\alpha'_{\hat{S}}}}{(1 + 1.5\tau_{\mathrm{cloud}}},$$
(2.21)

and the resultant broadband albedo is determined by summing all contributing components:

$$\alpha' = \alpha'_{\hat{S}} + d\alpha'_c + d\alpha'_\theta + d\alpha'_\tau.$$
(2.22)

Kuipers Munneke et al. [2011] added an additional term to describe the difference they found while using a model setup with a sub-Arctic winter atmosphere instead of a sub-Arctic summer

atmosphere as Gardner and Sharp [2010] did:

$$d\alpha'_p = 0.03247 \cdot \log\left(\frac{p}{1538.8}\right) ,\qquad(2.23)$$

with the surface pressure p in hPa.

2.5.5   Ray tracing in a three dimensional snow microstructure

Picard et al. [2009] and Xiong and Shi [2014] describe photon tracing in complex computer gener-
ated snowpacks with three dimensional microstructures. They calculate the spectral albedo as the
ratio of photons that escape the model snowpack at the top relative to the number that entered.
Knowledge of snow grain sizes and shapes within a snowpack is needed to use their approaches
and they demand high computational effort. Because of its complexity, it is hardly applicable to
field measurements. Kaempfer et al. [2008] show examples of studying snow microstructures with
computer tomography in the laboratory.

Picard et al. [2009] were able to study the influence of snow grain size on near-infrared reflectance
at 1310 nm and demonstrated its dependence on the shape of snow grains. The authors conducted
a comparison between their model and solutions from the model of Kokhanovsky and Zege [2004]
(see above) that accounts for different grain shapes. They also compared a standard DISORT
model treating snow grains as spheres and applying Mie-Theory. Picard et al. [2009] showed good
agreement of the three model approaches for spherical grains (their Figure 5). Non-spherical grains,
however, show a different slope of the relation between grain size and albedo at 1310 nm. The model
of Picard et al. [2009] and the model of Kokhanovsky and Zege [2004], despite of its simplicity,
agree well for complex grain shapes.

3. Results of a parameter study with a snow-albedo model

In this chapter, model studies are used to calculate changes of the reflectance of snow covered sea ice due to altered microphysical parameters of the snowpack, atmospheric conditions diffusing the incident radiation and the presence of LAI in the snowpack. A model permits the study of single parameters within a controlled environment. Most advances in understanding the physical principles that cause the characteristic spectral behaviour of the albedo were achieved by the model studies of Wiscombe and Warren [1980] and Warren and Wiscombe [1980] and slight improvements of their results and the general understanding are reviewed in Warren [1982]. The incentive of the model calculations in this chapter is to produce a look-up-table with accurate and representative spectral albedo values for further studies. These values shall be representative for the conditions found for snow on top of sea ice in the Arctic. The model results will also be used to explain the behaviour of the albedo and the physical principles based on the current state of knowledge.

For these studies, a DISORT based model of a snowpack coupled to an Arctic winter atmosphere was chosen. The DISORT approach was chosen above the other model approaches discussed in the previous section because it allows the study of thin snow layers. It can be expected that snow on sea ice is often not thick enough to completely mask the influence of the subjacent ground. The model of Kokhanovsky and Zege [2004] does not allow the study of optically thin snowpacks. Further, the direct coupling of snow and atmosphere allows the simulation of multiple reflections between the surface and the atmosphere that can have a significant influence on the amount, spectral distribution and fractioning of direct and diffuse solar radiation incident on the snow surface (e.g. Grenfell and Perovich [2008]). Thus Gardner and Sharp [2010] argue that a more accurate estimation of the spectrally integrated broadband albedo is possible with a DISORT model than with all models based on the equations by Wiscombe and Warren [1980]. These models only account for the fraction of direct to diffuse irradiance incident on the snow surface to calculate the spectrally resolved and broadband albedo but not for changes in the distribution of the spectrum.

There was also a motivation to develop and test a DISORT model setup with a snow layer at the bottom of the model domain because such a model can be used in various further studies involving situations with snow on the ground. The investigations are not limited to surface reflectance. Radiance and irradiance from both hemispheres can be evaluated at all levels of the atmosphere. This feature is necessary to evaluate atmospheric influences on airborne albedo measurements

(Section 4.2.4) with the method of Wendisch et al. [2004]. Therefore, a DISORT approach is more attractive than models like TARTES and SNICAR which are limited to radiative transfer in snow. The setup of a DISORT model developed here for the specific case of an optically thin snow layer on top of sea ice will itself be called a model. For better readability of this chapter, the model will be named SoSIM (Snow on Sea Ice Model).

In Section 3.1 it is described how SoSIM calculates the surface albedo and how snow and atmospheric properties are set up within in the model. Then, Section 3.2 gives an overview of the range of model parameters that were chosen to simulate a non-melting horizontally homogeneous snow cover on top of sea ice. The results of this simulation are presented in Section 3.3. The behaviour of spectral and broadband albedo are described and their variability due to the investigated parameters is quantified.

The principle model approach of SoSIM using the DISORT radiative transfer method is similar to the work of Gardner and Sharp [2010]. SoSIM is also based on the implementation of the DISORT code in the Santa Barbara DISORT Atmospheric Radiative Transfer model SBDART, version 2.4 [Ricchiazzi et al., 1998]. SBDART is a collection of libraries needed to set up radiative transfer simulations of the atmosphere. These libraries are used to setup of the atmospheric layers of the model. However, the specific optical properties for the snow layer cannot be obtained from such libraries. Hence, optical properties of pure spherical ice crystals are obtained with Mie-calculations (Section 2.3). In order to obtain the altered optical properties due to the impurity BC added to the snow crystals in an external mixture, additional calculations had to be implemented to the model. These calculations are done according to the current state of scientific knowledge (see the discussion in Section 3.1). However, these untested results obtained with SoSIM need to be compared against other results to check their plausibility. This is done in Section 3.4, where results are compared with simulations conducted with SNICAR-Online, TARTES and the model by Kokhanovsky and Zege [2004]. Furthermore, spectral albedo measurements from snow covered sea ice near Barrow, Alaska, were provided by courtesy of Richard Brandt from the Atmospheric Science Department of the University of Washington. It is tried to re-simulate these measurements with SoSIM.

3.1   Description and setup of the model

SoSIM is a coupled snow and atmosphere radiation transfer model based on the DISORT solver for the RTE and Mie-calculations with the MIE0 algorithm by Wiscombe [1980]. Its purpose is the study of a changing reflectance of a snow layer on top of sea ice due to the influences of snow properties, changes in atmospheric state and SZA. The setup of a snow layer in SoSIM can be thought of as setting a very dense ice cloud above the ground. A sketch (Figure 3.1) visualises the model layers of this plane-parallel radiative transfer model. The snow occupies one or multiple model layers at the bottom of the model domain. The other model layers above are set up as for usual simulations of atmospheric radiative transfer with a DISORT model. The chosen setup will therefore be described in the following from bottom to top beginning with the snow layer.

Figure 3.1: Sketch of the setup of atmosphere and snow layers in the DIS-ORT model. At the bottom a spectral surface albedo is prescribed describing the reflectance of sea ice. Above the ground, the snow layer is defined. Within the whole troposphere, background aerosol is present and at an altitude of 1 km a thin stratus layer is defined. Direct and diffuse solar radiation are calculated according to the SZA θ.
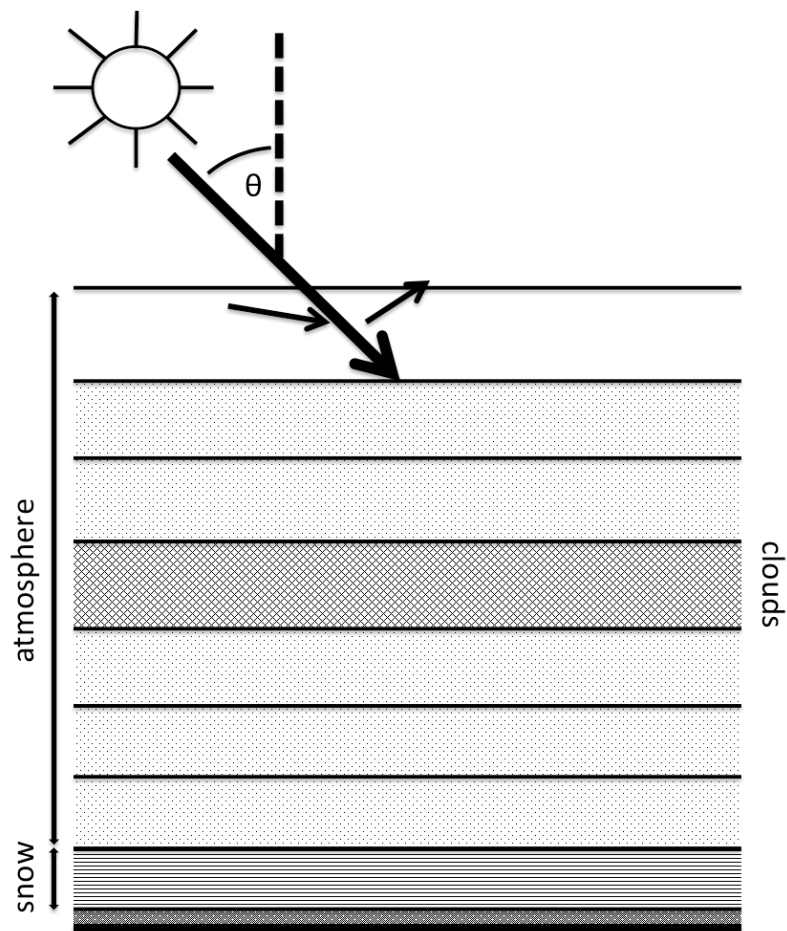
The single scattering properties of snow crystals define the optical properties of the model layers in which snow is present.

SoSIM is based on the implementation of the DISORT code in SBDART. In terms of the snow layers, there are three possible ways to define their optical properties in SBDART:

1. The option *spowder* defines one extra model layer beneath all atmospheric layers where optical properties can be defined that were pre-calculated according to the Mie-theory for ice crystals with a gamma size distribution and effective radii in the range 2 to 128 µm.

2. The options to set up aerosol layers can be used to define one or multiple layers with user defined optical properties in any altitude and of any thickness. This option only allows for one type of aerosol, i.e. only one snow grain size is possible. Density and optical thickness of the layers can be set individually.

3. Minor modifications to the source code of SBDART's user interface would allow to define an arbitrary number of layers with individual optical properties in the DISORT model. These modifications can be done, since SBDART is open source software written in Fortran.

The first possibility is not flexible enough for the investigation of effects of larger snow grain sizes and does not allow for LAI in snow at all. SoSIM utilises possibility 2 or a combination of possibilities 1 and 2. The latter allows to simulate a snowpack consisting of two layers, e.g. a layer of thin new snow on top of aged snow (see Section 3.3). For an evaluation of the effect of thinning snow on top of sea ice, possibility 2 is used in SoSIM.

The third possibility would allow for full flexibility in the investigation of the influence of various snow parameters and the effects of multiple snow layers with different properties. Zhou et al. [2003] demonstrated that models of snow albedo better reproduce field measurements if a multilayer snowpack, with layers having different snow grain sizes and densities, is used. Unfortunately, the time available for this thesis did not allow to do the necessary modifications to the code and to compile and test the program. It has to be noted, that possibility 3 is not specific to SBDART but works for any DISORT code.

The optical characteristics of snow that are used in the respective model layers are determined by mono-disperse Mie-calculations. The MIE0 algorithm with the wavelength dependent refractive index of ice at a temperature of $-3°C$ from Warren and Brandt [2008] (Figure 2.6) delivers these properties. The phase function of the snow crystals is expressed with the approximation introduced by Henyey and Greenstein [1941]. This approximation depends only on the asymmetry factor g and has been shown to provide good accuracy for primarily forward scattering ice crystals [Van de Hulst, 1968]. With the calculated extinction cross section, the optical depth of the snow layer can be determined following Equation 2.11.

If the effect of the LAI BC is to be evaluated, the additional absorption of BC particles mixed (externally) with ice crystals can be expressed by adding the mass specific absorption cross-sections (MAC) for pure ice κ_{abs}^{ice} and that of BC κ_{abs}^{BC} according to the BC mass ratio C_{BC}, following [Brandt et al., 2011] and [Marks and King, 2013]:

$$\kappa_{abs}(\lambda) = \kappa_{abs}^{ice}(\lambda) + \kappa_{abs}^{BC} \cdot C_{BC} \,. \tag{3.1}$$

The MAC of BC, $\kappa_{abs}^{BC} = 7.5 \, m^2/g$, was taken from Bond and Bergstrom [2006]. The absorption of BC has a negligible wavelength dependence [Bond and Bergstrom, 2006]. When BC particles are mixed in snow they contribute little to light absorption in the NIR because in that wavelength range the absorption of ice is relatively high. Dust within snow is not modelled, a choice that can be justified by the fact that the same mass of dust is about 200 times less absorbent than BC [Gardner and Sharp, 2010] and dust lacks sources within the Arctic that could provide high mass concentrations. Organic material, such as algae, and volcanic aerosol can reduce the albedo [Grenfell [1991]; Flanner and Zender [2006]] but are not examined in this study. This study is especially interested in the influence of anthropogenic LAI in the Arctic.

Below the snow layer the spectral albedo of sea ice is prescribed as lower boundary condition in order to represent realistic surface reflection of an optically thin snowpack on top of sea ice. The reflectance of sea ice follows the same optical principle as that of a snow layer [Gardner and Sharp,

Figure 3.2: Spectral albedo of sea ice as a function of wavelength (in nm). This spectral albedo was used to describe the reflectance of the ground beneath the snowpack in the model domain. These values are taken from Figure 6 of Gardner and Sharp [2010]. The albedo resembles a mixture of 0.3 air bubbles per cubic millimetre of ice. The bubbles have a radius of 0.05 mm.
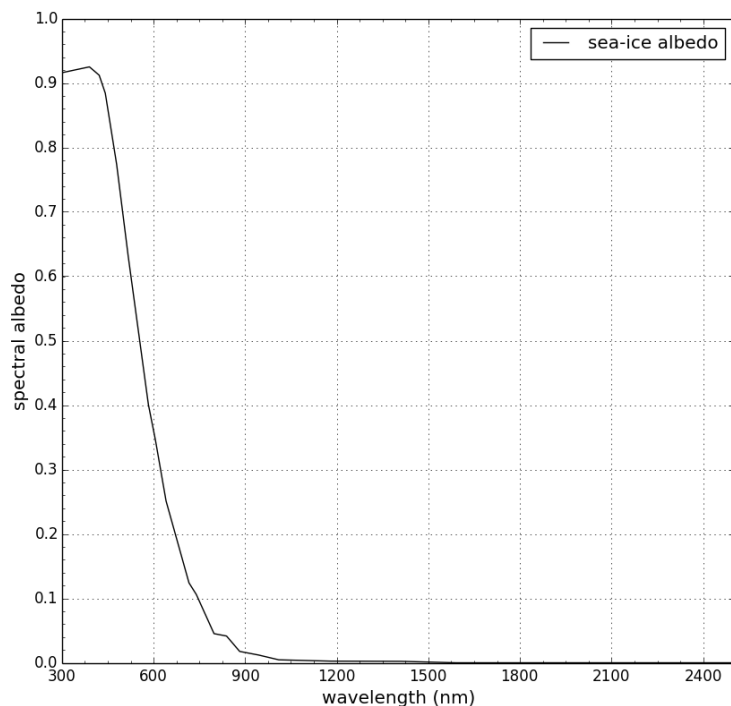
2010]. Impurities within the medium with different refractive indices cause scattering. In the case of sea ice, these impurities are air bubbles and brine pockets within the solid sweet water ice (whereas for snow it is ice particles in air). Since the path of light within ice is longer with lesser scattering events more light is absorbed, compared with a snow layer. In the VIS, light is also partly transmitted through the ice. Both, absorption and transmittance, reduce the reflectance of sea ice. For the spectral albedo of sea ice, this study is following the model result obtained by Gardner and Sharp [2010] shown in Figure 3.2. The spectral sea ice albedo has maximum values of 0.93 in the VIS and shows a steep decrease between about 500 nm and 1000 nm to an albedo value near zero.

The composition of the atmospheric layers is set up with a sub-Arctic winter atmospheric profile after McClatchey et al. [1972] describing the vertical distribution of atmospheric gases. No changes were made to this atmosphere provided with the SBDART package. Furthermore, within the atmosphere, a thin low-level stratus cloud layer with varying optical thickness can be set in SoSIM at an altitude of 1 km. Also, one type of standard background aerosol [Ricchiazzi et al., 1998] is present in the troposphere and stratosphere. Parameters set the optical thickness of the cloud and aerosol layer in SoSIM. Incident solar radiation at the top of the model domain (top of the atmosphere) is described with the SBDART default LOWTRAN-7 solar spectrum by Thekaekara [1974].

The flowchart of SoSIM (Figure 3.3) illustrates the single calculation steps that are needed to obtain all necessary parameters to set up snow layers in the DISORT model domain and then perform the radiative transfer calculations. For each step, the necessary user input (top row) and passing on of
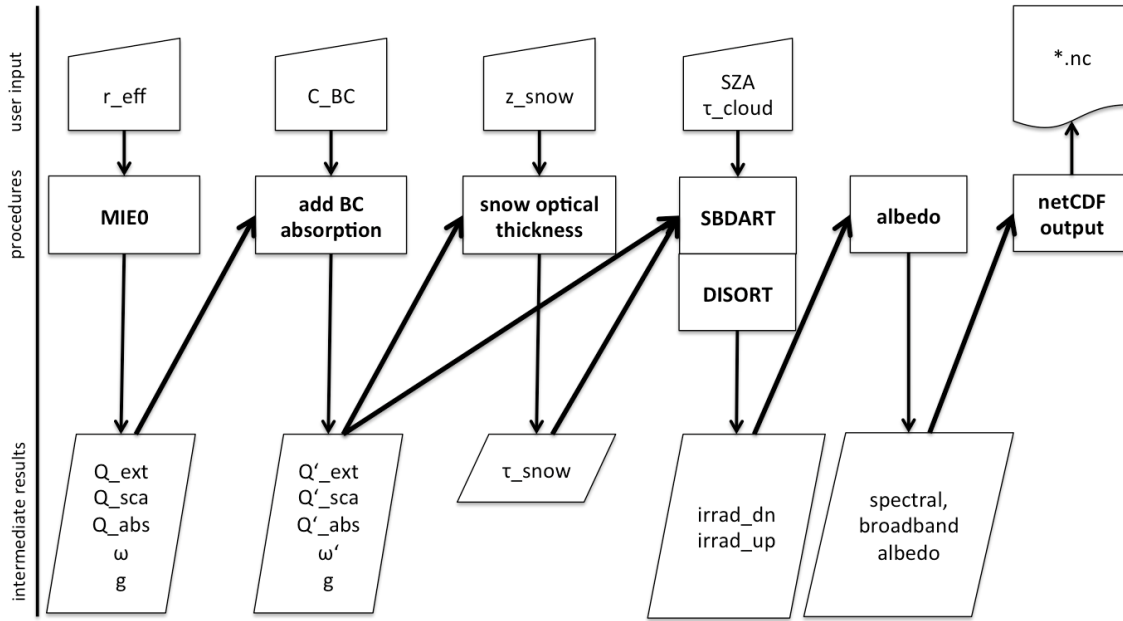
Figure 3.3: This flowchart of SoSIM – to be read from left to right – illustrates the calculation
steps necessary to obtain the surface albedo. The user input that has to be provided (first
row) is shown above the procedures (second row) that calculate intermediate results (third
row) which are passed on to the next calculation step. SBDART does the radiative transfer
calculation and uses some standard parameters (e.g. the atmosphere file) that are not
changed by user input.

calculated values from one procedure to the next (bottom row) is indicated. The first three columns
cover the calculation of the optical properties of a snow layer. The basic single scattering properties
of ice crystals with effective radius r_{eff} are calculated with the MIE0 algorithm. If the snow layer
includes BC, the optical properties are modified (indicated as primed quantities). The optical
depth of the snow layer τ_{snow} is calculated according to Equation 2.11 with the physical depth
z_{snow} as input parameter. These optical properties are used to define the snow layer in SBDART.
Information on aerosol optical thickness (AOD) τ_{aerosol}, cloud optical thickness τ_{cloud} and SZA are
input parameters passed to the model. Other parameters describing the model atmosphere (see
above) are not changed by user input. Finally, the results of the radiative transfer calculation with
SBDART, namely the upward reflected irradiance, the downward irradiance reaching the ground
and their ratio, the albedo (Equation 2.12), are calculated and stored in a NetCDF file. NetCDF
(the Network Common Data Format) is a handy array-oriented scientific data format that became
a de-facto standard in many scientific communities. This format was chosen for SoSIM because it
proved as practical while providing the model output to the data evaluation procedures used in
this study.

By looping the model over a set of different realisations, a look-up table can be created. This has
been done for the set of input parameters that is discussed in the next section. The look-up-table
is used for visualising different results and in order to quantify the influences of changes in the
parameters. The evaluation of effects on spectral and broadband albedo in Section 3.3 is partly based

on this look-up-table but also utilises results directly calculated with SoSIM. The look-up-table is also used in Chapter 5.1.

3.2   Parameters for Arctic-spring conditions

The aim of this study is to understand and quantify the variability of the albedo of snow covered Arctic sea ice. The model study will evaluate changes due to variations of the microphysical parameters of snow and atmospheric conditions within a realistic range that can be found in the Arctic during the months March through May. The parameters used for the calculation of a look-up-table with SoSIM are listed in Table 3.1. The used range of the respective parameters has been collected from the various reports in literature discussed in the following.

Snow grain size
Snow grain effective radius typically varies between below 0.1 mm for new snow to in between 0.5 and 1 mm for aged snow [Fierz et al., 2009]. Gallet et al. [2011] report measurements from several snow pits at Dome C, Antarctica, revealing grain radii between about 75 and 150 µm for aged wind-blown snow crystals in the upper layers of the snowpack. For the calculation of the look-up-table, values of 50 and 75 µm were chosen to represent new and fine grained snow. The range between 100 and 200 µm represents snow aged for up to a few weeks (see the discussion of snow metamorphism in Section 2.2). Larger grain radii between 400 and 600 µm represent snow that was subject to other metamorphism processes listed in Table 2.1. Melting or strong temperature gradients may lead to larger grain types like melt-clusters and faceted grains.

Snowpack depth and density
Warren et al. [1999] present a climatology of snow thickness and density on Arctic sea ice from several years of measurements at different sites. They report that the ice is mostly free of snow during August but snow accumulates rapidly during September and October, moderately during November, very slowly in December and January and then moderately again from February to May. The average thickness of snow on multi-year ice in the western Arctic is reported with in between 30 and 40 cm in April (Figure 9 in Warren et al. [1999]). No snow or very thin snow is found on new ice, e.g. refrozen leads, as snow accumulation has to begin anew. In general, snow thickness depends

Table 3.1: Snow and atmosphere parameters available in the look-up table.

parameter	unit	values									
r_{eff}	µm	50	75	100	125	150	200	400	600		
z_{snow}	cm	1	2	4	8	16	24	30	36	42	50	80
C_{bc}	ng/g	0	10	20	40	75	100	200			
θ	degree	50	60	75	80						
τ_{clouds}	-	0	10								

on the length of the accumulation period in the specific region. Wind causes a redistribution of the surface snow and, as a consequence, thickest snow is found in the wind shadow near ridges. In general, multi-year ice features thicker snow covers than first-year ice [Kurtz and Farrell, 2011].

Typical snowpack densities on sea ice range between $200\,\mathrm{kg/m^3}$ and $400\,\mathrm{kg/m^3}$ [Kurtz and Farrell [2011];Domine et al. [2008]]. An average density of $320\,\mathrm{kg/m^3}$ without much spatial variation is stated by Warren et al. [1999] for the end of the accumulation period (April and May) in the Western Arctic. For the calculation of the look-up-table, the chosen model parameter follows this value.

BC concentrations in snow

Doherty et al. [2010] review a variety of measurements of BC concentrations in snow at different locations in the Arctic in spring ranging from $4 \pm 2\,\mathrm{ng/g}$ at remote sites on sea ice, $8 \pm 3\,\mathrm{ng/g}$ in the Canadian and Alaskan Arctic, $13 \pm 9\,\mathrm{ng/g}$ around Svalbard and up to $34 \pm 46\,\mathrm{ng/g}$ in Arctic eastern Russia. These concentrations are low and concentrations $> 100\,\mathrm{ng/g}$ are only found in the presence of local sources such as heavy industry whereas in populated areas not necessarily high concentrations are found, as Doherty et al. [2010] reports measurements near Tromsø, Norway, of $C_{\mathrm{BC}} = 21 \pm 12\,\mathrm{ng/g}$. Sergent et al. [1993] report larger amounts of BC between about 100 to $300\,\mathrm{ng/g}$ are found in the French Alps and also at other sites in the northern hemisphere, outside the Arctic, highly variable amounts of BC (5-100 ng/g) are found. The look-up-table will cover pure snow, low concentrations of $10\,\mathrm{ng}$ BC per gram of snow and a range up to the quite high concentrations of 100 to$200\,\mathrm{ng/g}$.

Clouds and aerosols

Kylling et al. [1997] report an optical thickness of 10 for a shallow stratus water cloud observed in an alpine valley near Garmisch-Partenkirchen, Germany. This optical thickness is used to model a typical translucent stratus cloud in an altitude of $1000\,\mathrm{m}$ and evaluate its influence on the spectral distribution of the incoming solar irradiance.

The AOD, $\tau_{\mathrm{aerosol}} = 0.3$, is an average of the AOD observed with a sun-photometer during an airborne measurement campaign in the Arctic in 2011 (see Stone et al. [2010] and Section 4 for details). It was chosen for all of the following calculations.

SZA

Four values between $50°$ and $80°$ were chosen for the SZA to give a good representation the range of solar altitudes that can be found in the Arctic in spring at different latitudes. An SZA of $75°$ applies for most measurements taken during the airborne measurement campaign discussed in Section 4 and an SZA of $60°$ was observed during the in-situ measurements on sea ice by Brandt et al. [2008] near Barrow, Alaska, that are discussed in Section 3.4.

3.3 Results of the model study

Aiming to quantify the magnitude of the single influences on spectral and broadband albedo within a controlled model environment, calculations with SoSIM have been performed. The principle behaviour of the spectral and broadband albedo influenced by the parameters discussed below is known and has been described earlier – see the review by Warren [1982] and references therein. Nevertheless, evaluating the calculations with SoSIM allows to calculate the magnitude changes of the albedo for the particular set of parameters resembling Arctic conditions.

Generally, the spectral albedo in the wavelength range $280\,\text{nm} \leq \lambda \leq 2500\,\text{nm}$ (Figure 3.4 top) roughly follows the behaviour of the single scattering albedo ω (see Figure 2.8). Most sunlight in the UV and VIS is reflected from the snow surface as the albedo is close to 1.0 in these wavelength ranges, whereas the albedo decreases with wavelength in the NIR with two very distinct minima in the absorption band of ice around 1500 and 2000 nm.
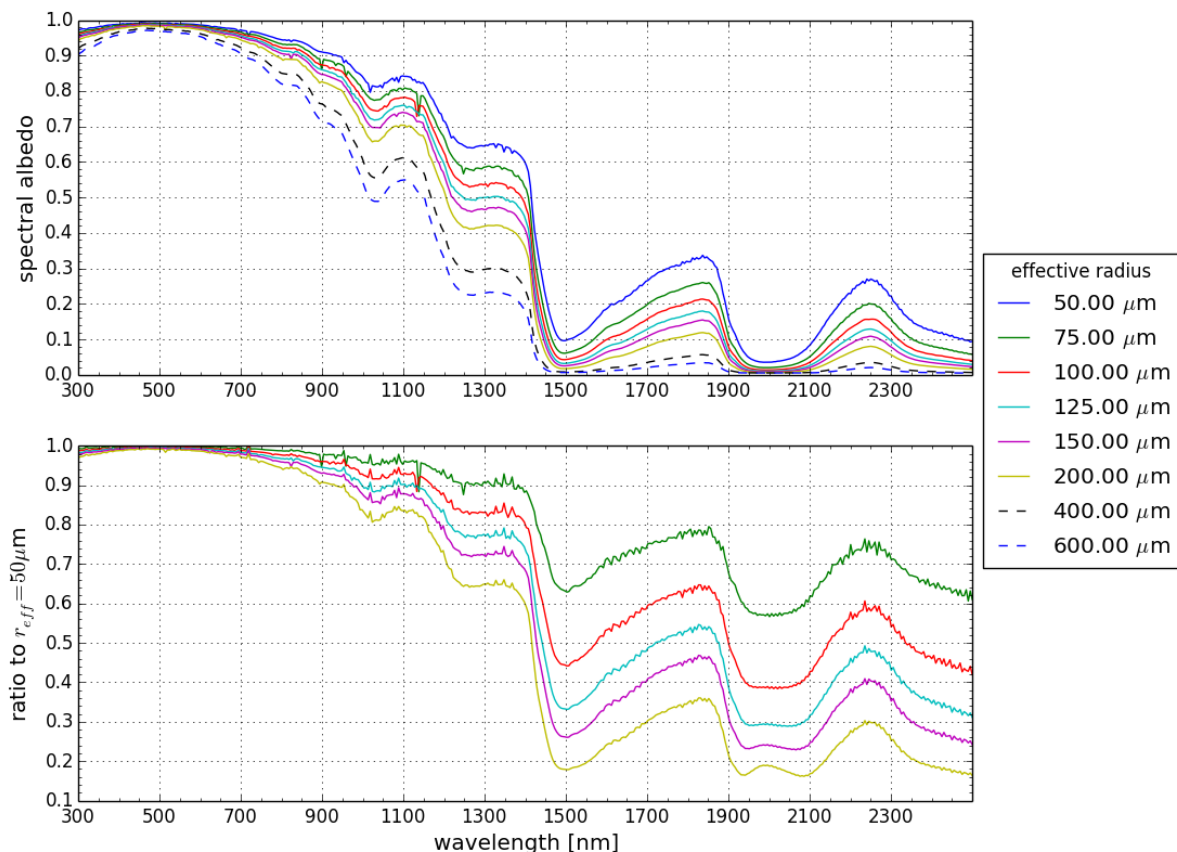
Figure 3.4: The upper figure shows the spectral albedo of a optical semi-infinite snow cover for several snow grain effective radii (r_eff) as function of wavelength (nm). Snow grain size varies in the range of snow ageing under cold conditions (solid lines) and snow close to melting (dashed lines). The lower figure shows the respective ratio to fine grained snow of $r_\text{eff} = 50\,\mu\text{m}$.

3.3.1   Influence of snow grain size

The albedo drops at all wavelengths as the grain size increases, Figure 3.4. This follows an relatively easy principle that a photon has a chance to be scattered (or a ray to be bent) when it crosses an air-ice interface (see Figure 2.5). It has a chance of being absorbed only while it passes through the ice. An increase of the grain size causes an increase in path length that must be travelled through the ice between the scattering possibilities [Warren, 1982]. Recapping Section 2.3.1, the refractive index n describes the propagation of an EM wave through a medium, the real part of the refractive index m indicates the phase velocity, while the imaginary part m' indicates the amount of absorption loss. m' increases with wavelength (Figure 2.6), and vice versa the single scattering albedo decreases (Figure 2.8). Thence, the effects of increasing snow grain size are stronger in the NIR than in the UV and VIS. This is shown in Figure 3.4 (bottom) as the ratio to the spectral albedo of a new snow surface with $r_{\mathrm{eff}} = 50\,\mu\mathrm{m}$ and optical infinite thickness at an SZA of 75°. An increase in grain size through snow grain metamorphism (Section 2.2) leads to a significant change in spectral albedo. For example, the wavelength region around 1300 nm is very sensitive to changes in snow grain size – doubling the grain size reduces the spectral albedo by roughly 20% (Figure 3.4, bottom).

3.3.2   Albedo increase with SZA

Snow shows an increasing albedo as the sun lowers to the horizon (Figure 3.5 top), a behaviour that is true for most surfaces Warren [1982]. The reason for that can be found in the fact, that a photon (or a ray) hits the first snow crystal near the surface at a grazing angle. If the scattering event sends the photon into an upward direction, its chance of escaping the snowpack without being absorbed is greater than it would be if it were scattered from deeper within the snowpack Warren [1982]. This effect is illustrated in Figure 3.6. The increase of albedo with lowering sun is greatly enhanced by the extreme asymmetry of scattering by snow crystals, whereby scattering in the forward direction is much more probable than in other directions (see Figure 2.7 for the polar plot of a phase function typical for a snow grain). The propagation of a photon in a snowpack is dominated by multiple scattering, but with the incidence angle onto the plane-parallel layer approaching a grazing angle, single scattering becomes more important. Figure 3.6 indicates that the coil of the phase function emerges from the snow layer for very high SZA and photons may escape the snowpack after a single scattering event Warren [1982].

The effects of angular details in the phase function of snow grains are smeared by multiple scattering. This favours the approximation of more complex grain shapes with rounded grains that is used in SoSIM. Warren [1982] argue that for a correct representation of the reflection at very low incidence angles, a fully correct phase function instead of the approximations with Mie-Theory and Henyey-Greenstein phase function should be used. Thence, no SZA > 80° are evaluated in this study.

An increasing SZA has almost no effect on the albedo in the UV and VIS, see Figure 3.5 lower left. However, the effect increases with wavelength from about 700 nm. Within the absorption bands of ice around 1500 and 2000 nm, compare Figure 2.6, the decreasing number of interactions with snow
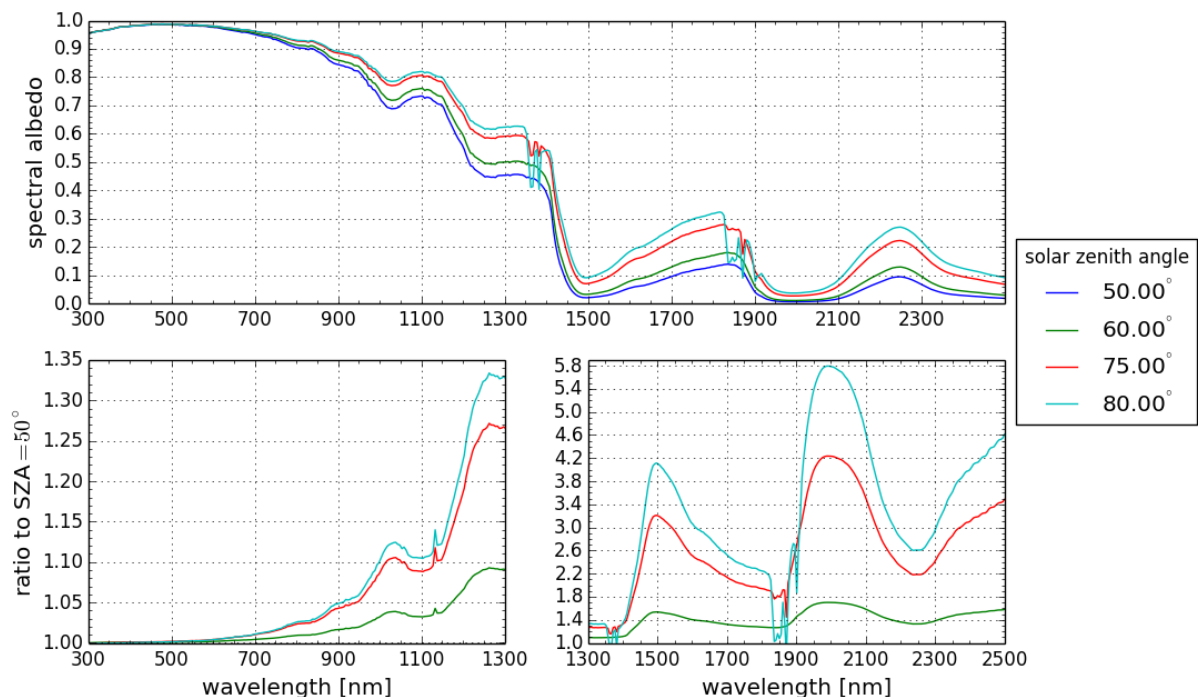
Figure 3.5: The upper figure shows the variation of the spectral albedo of a optical semi-
infinite snow cover of grain size $r_{\text{eff}} = 100\,\mu\text{m}$ for four different SZA. The lower figures show
the change due to a lowering sun as the as the ratio to the spectral albedo at an SZA of 50°.
The figure was split at 1300 nm since the albedo is much more sensitive in the NIR.

grains that photons have at lower solar altitudes, increases the spectral albedo to a multiple of the
value at higher solar altitudes, e.g. lower SZA (Figure 3.5 lower right). From these two studies, it
has to be noted that the albedo of an optically thick snowpack is ultimately determined by the
snow grain size and the SZA, i.e. the time of the day.

3.3.3 Additional absorption of BC

Adding light absorbing BC to a snowpack enhances the absorption of pure ice. With this common
modelling approach (Section 3.1), the optical properties of ice and BC are mixed. This is an
optical bulk approach treating the mixture of BC with ice crystals as a homogeneous volume
of a new material. In nature one would expect an external mixture of an ice particle that
collects smaller BC aerosols or, eventually, ice particles that undergo heterogeneous internal mixing
with BC [Bond and Bergstrom, 2006]. The MAC chosen for modelling the effects of BC has to
account for this complexer optical effects on the microscopic level with a value offering a good
approximation of the average absorption. The effect of BC has been calculated for a MAC
$\kappa_{\text{abs}}^{\text{BC}} = 7.5\,\text{m}^2/\text{g}$ [Bond and Bergstrom, 2006], used as the default value for all other studies in
this thesis. Additionally, the effect of $\kappa_{\text{abs}}^{\text{BC}} = 11.3\,\text{m}^2/\text{g}$ has been evaluated, which represents the
absorption of BC enhanced by a factor of 1.5 due to ageing [Bond and Bergstrom, 2006] (see the
discussion in Section 2.3). BC is evenly distributed within a snow layer and at every single scattering
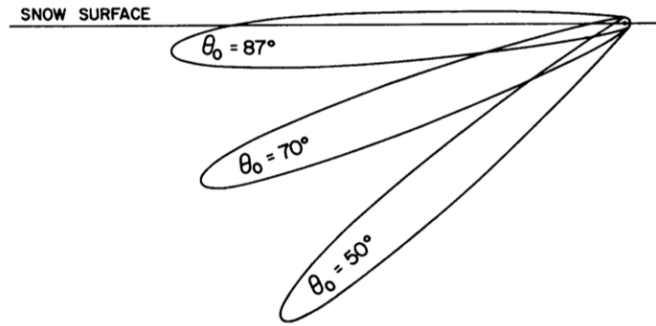
Figure 3.6: Polar diagram of the scattering phase function of a snow crystal at the surface
of a snow layer for three SZA. The phase function indicates the possibility that a scattered
photo will go into a particular direction. Here, it especially indicates the possibility that
it changes its direction of propagation into an upward direction. This figure is taken from
Warren [1982] and the phase functions are calculated for unrealistically small snow grain
sizes ($r_{\text{eff}} = 10\,\mu\text{m}$, $\lambda = 5000\,\text{nm}$) for display purposes. The asymmetry of the phase function
would otherwise become much more extreme for larger r_{eff} or smaller λ [Warren, 1982].

event, a photon interacts with snow including BC.

In Figure 3.7 it is shown how raising the concentration of BC in a snowpack lowers the albedo.
Presented is the ratio to pure snow. Both results shown in this figure were calculated for the same
conditions but an effective grain radius of $50\,\mu\text{m}$ on the left and $100\,\mu\text{m}$ on the right. Concentrations
found in snow on Arctic sea ice are mostly very low with about $10 \pm 10\,\text{ng/g}$ (see previous section).
The change in spectral albedo has its maximum at approximately $450\,\text{nm}$ and is below 1% relative
to pure snow for the expected $C_{\text{BC}} < 40\,\text{ng/g}$. The effect of BC increases with grain size since the
presence of BC enhances the absorption of the whole ice crystal. The spectral albedo is affected
almost only in the UV and VIS, Figure 3.7. This general observation is in good agreement with
other studies, e. g. Wiscombe and Warren [1980] and Gardner and Sharp [2010].

The reduction of the broadband albedo has been calculated for three values of C_{BC} (Table 3.2).
The broadband albedo for a clean snow layer of $100\,\mu\text{m}$ grains, infinite optical thickness and an SZA
of $60°$ is 0.8324. The effect of BC has been calculated for $\kappa_{\text{abs}}^{\text{BC}} = 7.5\,\text{m}^2/\text{g}$ and $\kappa_{\text{abs}}^{\text{BC}} = 11.3\,\text{m}^2/\text{g}$
and the results show the expected stronger albedo reduction of a higher MAC. Thus, the ageing
of carbonaceous aerosol has a considerable effect on its ability to absorb light and reduce the
albedo of snow when it is deposited onto the ground. Most pollutants are transported to the
Arctic via long-range transport, thus ageing processes (e.g. coagulation, coating) are likely to take
place. Models like SNICAR use a MAC of $7.5\,\text{m}^2/\text{g}$ [Flanner et al., 2007] albeit using the MAC
enhancement factor of 1.5 suggested by Bond and Bergstrom [2006] seems realistic, at least for the
Arctic. Therefore, the magnitude of albedo reduction through BC has a remaining uncertainty.
A higher MAC would in fact mean that a smaller amount of BC is needed for the same albedo
reduction.

The strength of the BC effect also depends on snow grain size [Warren and Wiscombe, 1980]. The
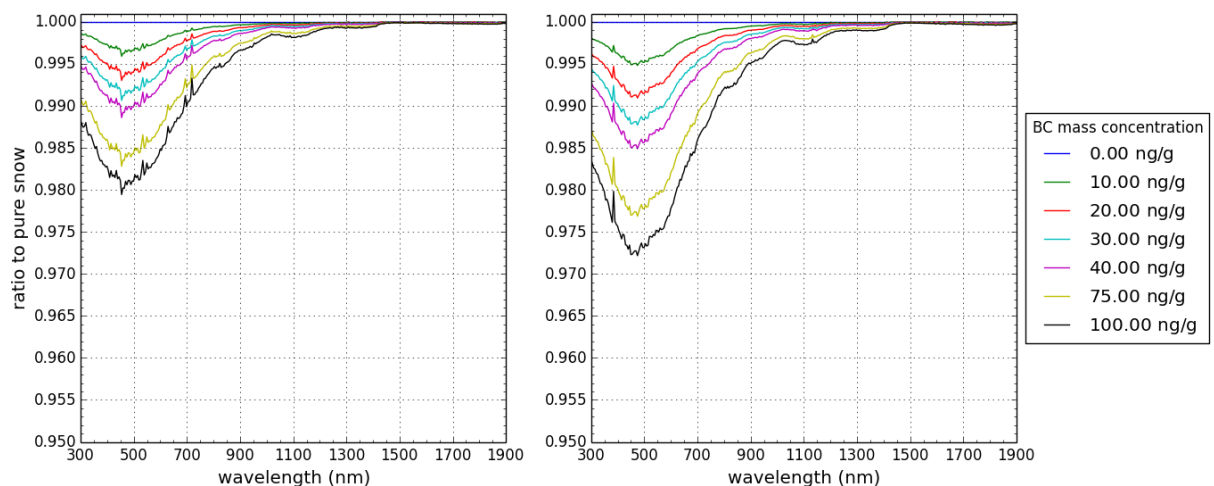difference is shown for two grain sizes in Figure 3.7, left and right. As an example, adding $40\,\text{ng/g}$

Figure 3.7: Light absorbing carbon within the snow deceases the albedo with increasing mass concentration C_{BC}. Shown is the effect on the spectral albedo of a snow layer with grains of $50\,\mu m$ (left) and $100\,\mu m$ (right) effective radius as the ratio to pure snow. The effect is stronger for larger grains. No significant effect is found for $\lambda > 1900\,nm$.

BC to pure snow lowers the broadband albedo by 0.6% for $r_{eff} = 50\,\mu m$ grains and has a stronger effect of 0.8% for snow consisting of larger $r_{eff} = 100\,\mu m$ grains.

3.3.4   Albedo of thin snow covers

Snow on top of sea ice is often thin. Thence, it is interesting to evaluate the effect of a thin snow cover on top of a darker surface. Light penetrates into the snow layer and it may reach the underlying ground after multiple scattering events with snow crystals if the snow layer has a non-infinite optical thickness. The optical thickness τ_{snow} depends on the physical thickness and density of the layer and also on wavelength dependent quantities like the efficiency of light extinction. The optical thickness also behaves anti-proportional to the effective grain radius (Equation 2.11). Light extinction in ice is weaker in the VIS and UV than in the NIR, therefore a snowpack may be semi-infinitely thick, i.e. not translucent, for thin snow in the NIR but not for shorter wavelengths.

Table 3.2: Broadband albedo reduction due to BC, calculated for two different MAC – for a initially clean snow layer of semi-infinite thickness, consisting of grains with $100\,\mu m$ effective radius at an SZA of 60° having a broadband albedo of 0.8324.

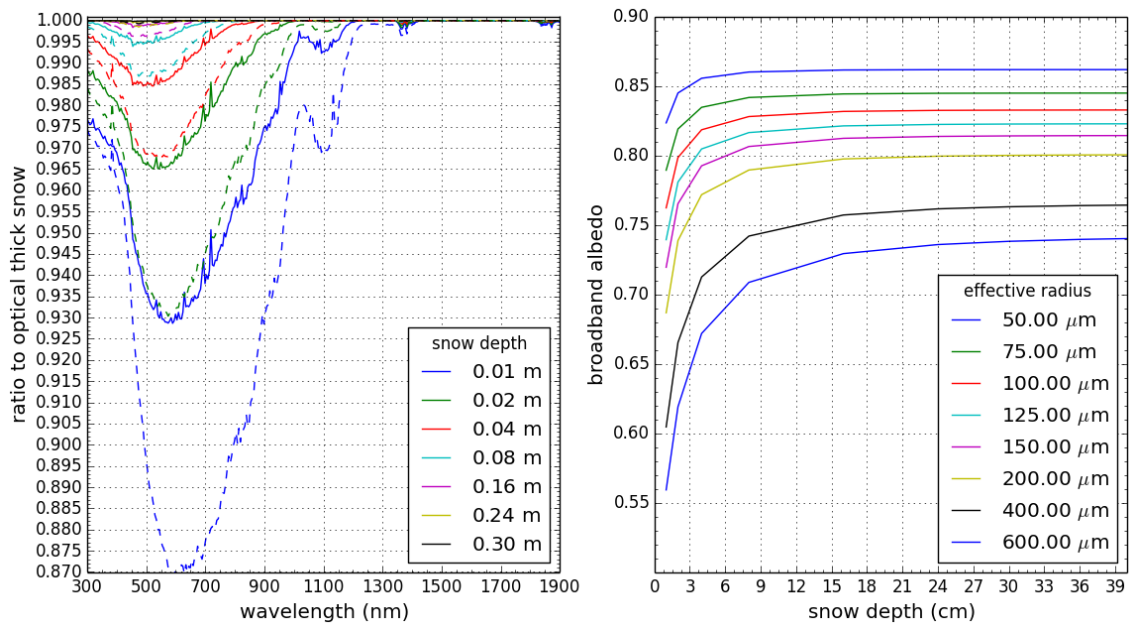|	albedo		change (%)	
C_{BC} | MAC	$7.5\,m^2/g$	$11.3\,m^2/g$	$7.5\,m^2/g$	$11.3\,m^2/g$
$40\,ng/g$	0.8255	0.8230	0.8	1.1
$100\,ng/g$	0.8184	0.8140	1.7	2.2
$200\,ng/g$	0.8095	0.8028	2.8	3.6

Figure 3.8: As snow becomes physically and optically thinner, the underlying ground shines
through and influences the albedo. The optical thickness is a function of wavelength. A
layer is optically semi-infinite thick if increasing its physical thickness no longer changes the
albedo. The left figure shows the spectral albedo for snow of $r_{\mathrm{eff}} = 50\,\mu m$ (solid lines) and
$r_{\mathrm{eff}} = 100\,\mu m$ (dashed lines). The figure to the right shows broadband albedos for different
effective radii. Both figures feature an SZA of $60°$.

The fraction of light that reaches the bottom of the snowpack is influenced by the albedo of the
ground. The sea ice present beneath the snow layer in this study has an albedo of about 0.9 in the
UV and VIS, whereas the albedo shows a steep decrease from about $500\,\mathrm{nm}$ to near zero in the NIR
(Figure 3.2). Thus, if the snowpack is optically thin, its albedo is lower [Wiscombe and Warren,
1980]. The model results presented in Figure 3.8 (left) show that the wavelength range from the
UV to about $1200\,\mathrm{nm}$ is influenced by thinning snow. The maximum of the effect is found around
$500\,\mathrm{nm}$ but shifts towards $600\,\mathrm{nm}$ as snow thins because of the spectrally non-uniform sea ice albedo.
Optical thickness depends on snow grain size and thus the effect is stronger for larger snow grains,
as shown for two examples with 50 and $100\,\mu m$ grain radius.

The spectral response of the surface albedo to thinning snow is very similar to the effect of a
rising BC content within the snow (compare Figure 3.7). Figure 3.9 demonstrates the similarity
of the spectral signatures with an attempt to balance both effects. The ratio has been calculated
from the spectral albedo of two snowpacks with equal microphysical parameters and downward
radiation, but one with $40\,\mathrm{ng/g}$ BC content and semi-infinite thickness, the other with pure snow
and only $6\,\mathrm{cm}$ thickness. It is very close to 1 (deviation $\ll 0.5\%$). The wavelength dependence arises
from the spectral albedo of the surface, whereas BC is a spectrally uniform (grey) absorber. This
confirms the argumentation of Warren [2013] that remote sensing of BC in snow is only possible
with measurements of the spectral albedo, if snow thickness is independently known.
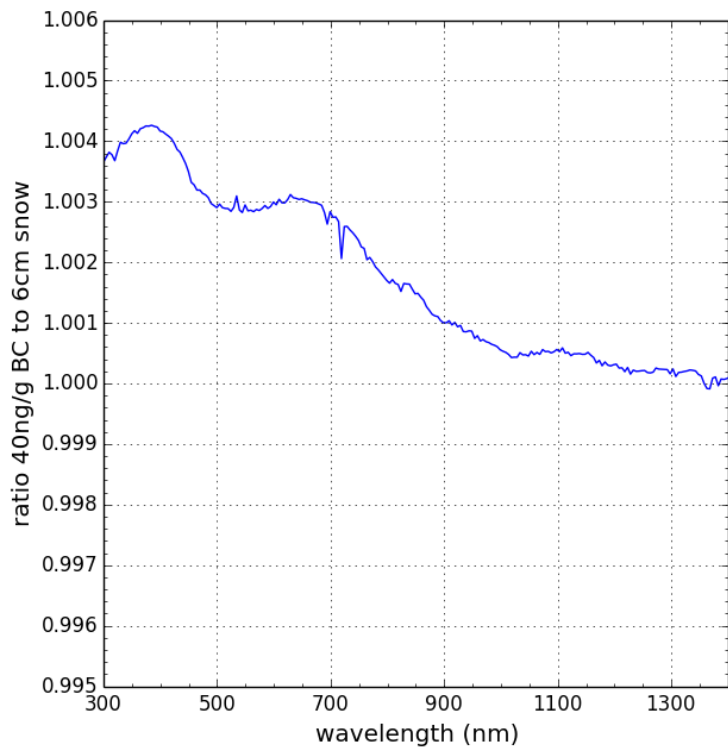
Figure 3.9: Ratio of the albedo of two snowpacks ($r_{\text{eff}} = 100\,\mu\text{m}$ and SZA of $60°$), one with $40\,\text{ng/g}$ BC content and semi-infinite thickness, the other with pure snow and only $6\,\text{cm}$ thickness. With this rough adjustment, a ratio of ≈ 1 could be reached.

Fine grained snow is optically semi-infinite for snow layers thicker than about $15\,\text{cm}$, since the broadband albedo asymptotically approaches its value of a infinitely thick layer and no longer changes once a certain thickness is reached (Figure 3.8, right). This behaviour is described as the asymptotic extinction of radiative flux [Bohren and Barkstrom, 1974]. Below about half of this threshold, the broadband albedo reveals a steep, non-linear decrease. Coarse grained snow has to be thicker to reach a semi-infinite optical depth.

Snow thinner than $1\,\text{cm}$ was not modelled with SoSIM since such snow layers may not be generalised by the assumptions made. The resulting uncertainties are too large. The assumption of spherical grain shapes might not hold near the sea ice. Due to the large temperature gradient between the warm surface and the cold atmosphere, faceted ice crystals grow that have optical properties different to rounded grains (Section 2.2). The approximations made in this radiative transfer model might not produce realistic surface reflection of such thin but complex layers because the angular details in the phase functions of the single snow grains are not smeared by multiple scattering (see the discussion above about reflection at high SZA). Furthermore, as a thin snow layer is almost not compacted by its own weight, the snow density used for the calculations of the look-up table might be to high. Also, new and wind blown snow with a thickness of 1 to $2\,\text{cm}$ might also form patches on the ice rather than a closed snow surface. However, the assumptions should hold for closed snowpacks of more than $2\,\text{cm}$ thickness.

Calculations with SoSIM (not shown) infer that changes of the density of a snowpack, within the typical range found in the Arctic (150 to $350\,\text{kg/m}^3$), only have minor influence on the optical thickness of the snowpack and do not significantly change the its albedo ($< 1\%$). Field measurements confirm the negligible effect of snow density on the reflectance. Bohren and Beschta

[1979] compacted a snow layer with a snow mobile and the reflectance before and after the compression also only changed by 1%.

3.3.5   Effects of stratus clouds

For the interpretation of measurements of a snow surface's albedo it is important to understand the different effects of a cloud layer on the spectral and broadband albedo. A stratus cloud layer with certain optical depth can therefore be set in SoSIM and allows to study these effects. The only effect of a cloud cover on the spectral albedo is, that the incident radiation on the snow surface becomes diffuse. The spectral albedo approaches values observed for purely diffuse radiation at an SZA of about 50°. This SZA is therefore called the effective SZA of diffuse radiation [Wiscombe and Warren, 1980]. In most cases, a higher SZA is observed in the Arctic, which implies a decreasing spectral albedo during an overcast, compared to clear sky conditions (see Figure 3.5).

Clouds also change the spectral distribution of the irradiance that reaches the surface by attenuating light in the NIR more than in the VIS. This effect is often called the *spectral shift* [Carroll and Fitch, 1981]. This effect becomes important when evaluating the broadband albedo, which is defined by integrating both, incoming and reflected irradiance over the solar spectrum (Equation 2.13) as done by pyranometer measurements. The actual distribution of spectral irradiance reaching the surface is always a weighting factor to the albedo. Thus, the broadband albedo becomes higher in the presence of a cloud cover as the higher albedo values in the VIS get more weight than the lower values in the NIR. Table 3.3 shows broadband albedo values simulated with SoSIM for the same setup except for a change from clear sky conditions to an overcast with thin water stratus clouds at an altitude of 1 km. This effect is relatively strong and changes the broadband albedo by a similar magnitude as snow grain metamorphism. It has to be considered when comparing broadband albedo measurements with unknown cloud conditions.

Table 3.3: Increase in broadband albedo from clear sky conditions to an overcast sky with $\tau_{\mathrm{cloud}} = 10$ for three different snow grain radii, semi-infinite thick snowpack and an SZA of 50°.

r_{eff}	50 µm	100 µm	200 µm
clear sky albedo	0.8539	0.8245	0.8058
overcast albedo	0.9080	0.8864	0.8719
change in %	6.0	7.0	7.6

3.4   Model performance and comparison of results

In this section, the spectral and broadband albedo modelled with SoSIM for different test cases is compared to other data to see if the model produces reasonable values. No accurate measurements under a controlled environment were available for this study in order to perform a sophisticated validation. Calculating irradiances in SoSIM is done with SBDART, a DISORT based code and

a library for atmospheric radiative transfer. This well tested modelling tool should yield realistic results of the irradiance reaching the snow cover above the ground. However, to obtain the optical properties of snow grains and BC particles involves calculations with Mie-Theory and further equations which are not part of a standard software. Especially the additional absorption of BC that reduced the albedo is a suspect for uncertainties.

3.4.1 Inter-comparison of models

To check if the spectral albedo values simulated with SoSIM are plausible, a set of results has been compared to other established snow-albedo models SNICAR-online, TARTES, the asymptotic solution model formulated by Kokhanovsky and Zege [2004] and the parametrisation of the broadband albedo of Gardner and Sharp [2010] – see the brief introduction of those models in Section 2.5.

For the inter-comparison of the models, a consistent setup that can be realised with all models has been chosen. The key uncertainties of the implementation of the additional absorption due to BC in SoSIM. The snow cover has been chosen to be optically semi-infinite because not all models can account for a thin snowpack and the effects of the darker surface below the snow. An SZA of 60° was chosen together with clear sky conditions. The resulting spectral albedo for the simulations of a one layer snowpack consisting of spherical grains with $r_{\text{eff}} = 200\,\mu\text{m}$ are presented in Figure 3.10.

Overall, the results of all models agree. Where absorption by BC is relevant, in the range $400\,\text{nm} \leq \lambda \leq 900\,\text{nm}$, all models are well within $\pm 1\%$ relative to the results obtained with TARTES (Figure 3.10, right top). However, there are some differences. Concerning the effect of additional absorption by BC, TARTES does not show the same albedo reduction towards the UV as the other three models. Furthermore, there is a spread of the ratio between each model and the results of TARTES for the three different BC concentrations (marked with different dash patterns) throughout the UV and VIS. This indicates different sensitivities of the models to the same mass concentrations of BC in snow.

SoSIM and TARTES agree well in the region around 1300 nm, where the albedo is very sensitive to both grain size and SZA (compare Figure 3.4). SNICAR deviates from the other models by about 2% in this wavelength range. The differences in the NIR are bigger (Figure 3.10, right bottom). While SoSIM and TARTES show quite similar results, the model of Kokhanovsky and Zege [2004] shows lower albedo values. Differences are most pronounce where the albedo is near zero. None of the other three models show a peak value at 1850 nm that is as strong as in the SNICAR-online result. The reason is not known. One possibility are the different algorithms used for the calculation of the single scattering properties. SNICAR uses the BHMIE algorithm while for the calculations in SoSIM, the MIE0 algorithm is used as a standard. However, using mono-disperse calculations with the BHMIE algorithm in SoSIM does not produce results different to the results obtained with the standard algorithm. The fact that Mie-calculations for SoSIM are done for a mono-disperse grain size distribution whereas SNICAR-online uses a lognormal size distribution does not produce singular differences in the spectral albedo. The agreement between SoSIM and TARTES proves this hypothesis.
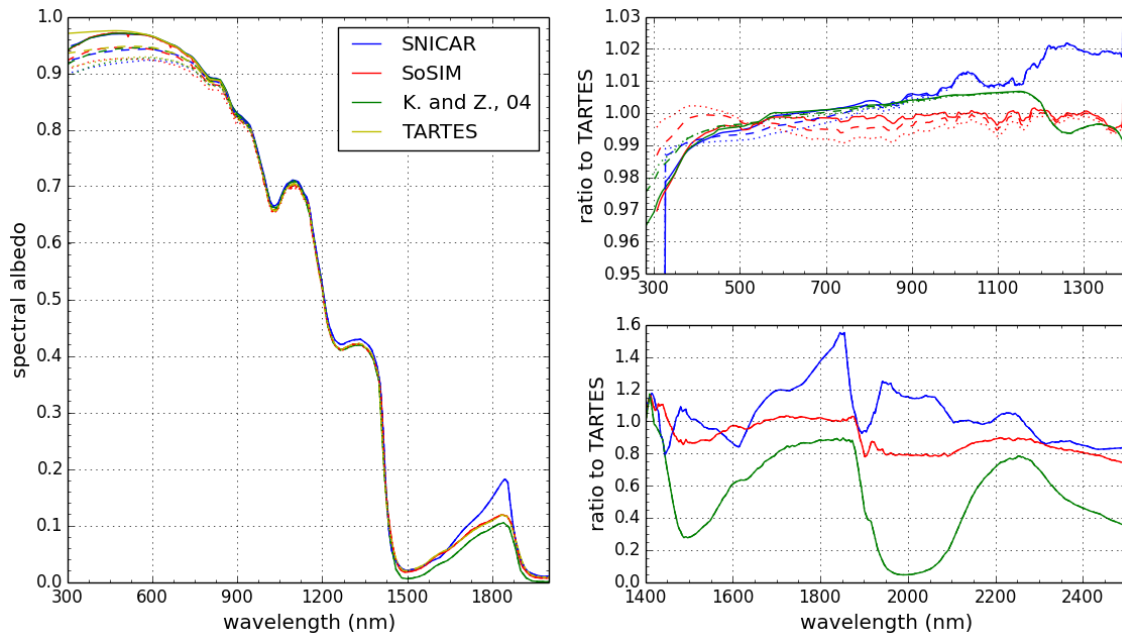
Figure 3.10: Simulations with the same setup have been conducted with SoSIM, SNICAR-online, TARTES and the asymptotic solution model by Kokhanovsky and Zege [2004]. The snow layer was optically semi-infinite (160 cm deep) and consisted of spherical snow grains of $r_{\mathrm{eff}} = 100 \, \mu\mathrm{m}$. The SZA was chosen as 60° with clear sky conditions. The BC content in the snow changed from $C_{\mathrm{BC}} = 20 \, \mathrm{ng/g}$ (solid lines) to $C_{\mathrm{BC}} = 100 \, \mathrm{ng/g}$ (dashed lines) and $C_{\mathrm{BC}} = 200 \, \mathrm{ng/g}$ (dotted lines). The ratio shown to the right is calculated relative to the results of TARTES. The spectral range has been split in order to zoom in on the VIS range (right top). Note that no data is available from SNICAR for $\lambda < 315 \, \mathrm{nm}$.

Comparing broadband albedo values calculated with SoSIM, SNICAR-online and the parametrisation of Gardner and Sharp [2010] for different concentrations of BC in the snowpack and different snow grain radii yields a good agreement of all three models. The calculated values are presented in Table 3.4. SoSIM predicts a higher broadband albedo than both other models for equal snow parameters and SZA. Its predicted values are $< 1.1\%$ higher than the results of SNICAR-online and $< 0.5\%$ higher than the results of the parametrisation after Gardner and Sharp [2010]. This differences might be explained due to the fact that all three models use different setups of the respective model atmospheres including different vertical profiles of temperature, trace gases and aerosols. This changes the spectral distribution of the radiation incident at the snowpack.

3.4.2   Comparison with field measurements

It was also possible to compare SoSIM results with field measurements from the specific use case of snow covered sea ice. Data from spectral albedo measurements were provided by courtesy of Richard Brandt from the Atmospheric Science Department at the University of Washington, USA.

Table 3.4: Change in broadband albedo for increasing concentraion of BC in snow for two different snow grain radii, semi-infinite thick snowpack and an SZA of 60°. Presented are values calculated with SoSIM, SNICAR-online and the parametrisation after Gardner and Sharp [2010], for the latter see Section 2.5.

	SoSIM		SNICAR		parametrisation	
$C_{BC} \mid r_{eff}$	$100\,\mu m$	$200\,\mu m$	$100\,\mu m$	$200\,\mu m$	$100\,\mu m$	$200\,\mu m$
$20\,ng/g$	0.8287	0.7950	0.8200	0.7874	0.8287	0.7957
$100\,ng/g$	0.8186	0.7809	0.8098	0.7730	0.8162	0.7782
$200\,ng/g$	0.8097	0.7685	0.8010	0.7608	0.8065	0.7647

Theses measurements were conducted on the 15.04.2008 on sea ice in Elson Lagoon near Barrow, Alaska. Information about the measurement campaign done together with the Norwegian Polar Institute are published in Brandt et al. [2008]. Their ground measurements were performed with an ASD Inc. (Boulder, USA) FieldSpec spectroradiometer in the spectral range from 350 to 2500 nm. Their measurements are presented in Figure 3.11 (left) as the mean, maximum and minimum (black lines) of measurements at five spots along a straight line and each 50 m apart. Their instrument probably reached the detection limit from around 2400 nm where the spectral albedo shows a steep increase.

New snow had fallen on the 14.04. and the site had a clean, untouched snow cover with a total thickness between 30 and 40 cm. The snow pack obviously consisted of at least two distinct layers – a fresh snow layer on top of a layer of aged snow. The density of the snowpack at the sites was around $150\,kg/m^3$ except for one cite with $422\,kg/m^3$. The SZA during the measurements is stated with about 60° and the sky was clear.

For the re-simulation of the spectral albedo with SoSIM the input parameters for effective radius of the snow grains and BC content in the fresh snow cover are unknown. Hence, several grain sizes were tested to best fit the observations of Brandt et al. [2008].

First, SoSIM was set up with one snow layer and the SZA is set to 60°. From the relatively good agreement (difference < 0.005) of the albedo between 1250 and 1300 nm, the snow grain radius was assumed to be 75 μm, utilising that the albedo is very sensitive to r_{eff} in this region. This realisation is plotted as a red line in Figure 3.11, where the spectral albedo is presented on the left and the difference between measurement and model prediction is presented on the right. To reduce the difference between the curves in the UV and VIS, 20 ng/g BC were added to the model snowpack. Still, a difference between 0.01 and 0.02 is found in the spectral albedo between 450 and 950 nm. Larger differences can be found in the NIR around the local maxima of the spectral albedo at 1800 and 2300 nm.

A second realisation was set up because the SZA during the measurements was stated rather coarse with approximately 60°, "close to the mean incidence angle of diffuse irradiance" [Brandt et al., 2008]. Therefore, an SZA of 50° was chosen for this simulation and r_{eff} had to be adjusted to
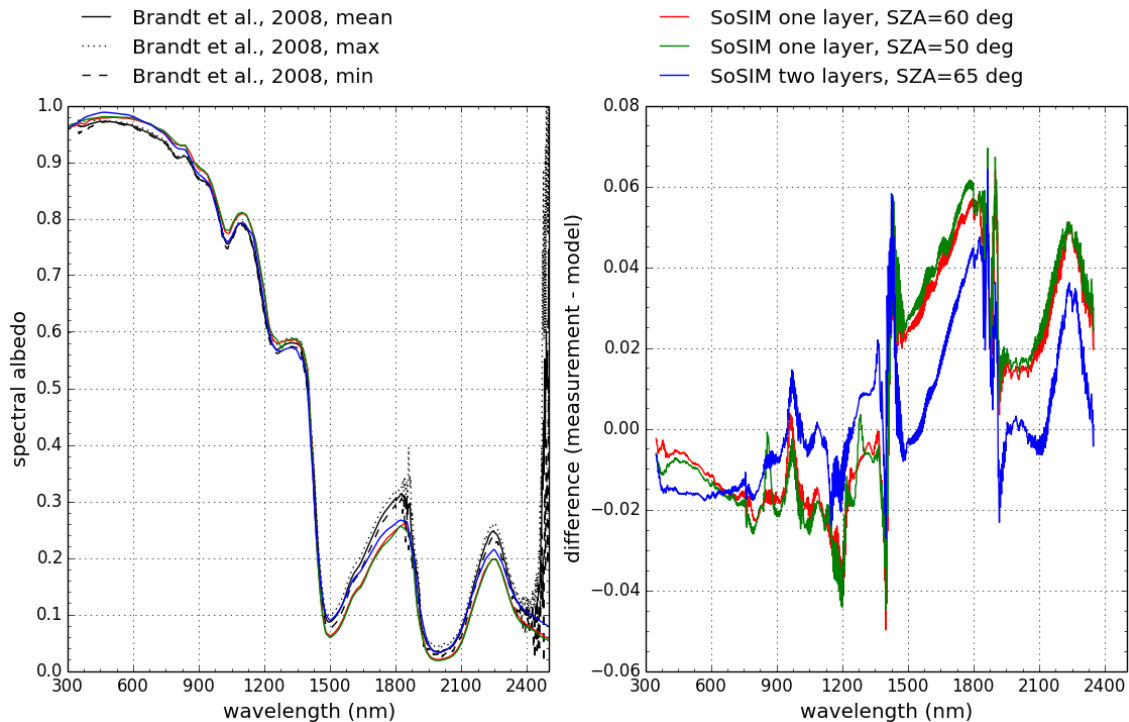
Figure 3.11: Re-simulation of measured spectral albedo from a site on the sea ice in Elson
Lagoon near Barrow on the 15.04.2008 – data provided by courtesy of Richard Brandt, Atmos
Washington, as documented in Brandt et al. [2008]. The measurement data is represented
as the mean, max and min of five measurements along a track on the ice. New snow had
fallen on the day before the measurements. The SZA was about 60° and the sky was clear.

minimise the difference of the albedo between 1250 and 1300 nm. An effective radius of 57.5 μm
produced the best fit. This realisation is plotted in Figure 3.11 with a green line and shows strong
similarity to the first realisation despite different parameters for SZA and r_{eff}. The high differences
for $\lambda > 1500$ nm remains. A test revealed that this high deviation could be minimised by raising
the SZA towards 67°. Unfortunately, tuning of this model parameter decreases the agreement of
the values around 1250 nm significantly.

A third realisation was conducted in order to account for the snow stratification with new snow
on top of aged snow. SoSIM was set up with two snow layers. The lower consisted of aged snow
with 110 μm effective radius and semi-infinite thickness and was covered by a layer of finer snow
grains. The upper layer had a physical thickness of 10 cm and was therefore translucent for shorter
wavelength such that an optical mixture of the upper and lower snow layers was possible. The SZA
could be set to 67° and an effective radius of the $r_{\mathrm{eff}} = 57.5$ μm was needed to balance to albedo
in the spectral region between 1250 and 1300 nm. Three effects we counter acting on the spectral
albedo, namely an increase due to smaller snow grain size, an increase due to a higher SZA and a
decrease due to the less reflective underlying medium. This realisation is presented in Figure 3.11
with a blue line. It shows better agreement from 900 to 1300 nm and around 1800 and 2300 nm. No
BC was added to the snowpack, thus the difference in the VIS shows a different behaviour than the

other two realisations.

The agreement of the spectral albedo between re-simulation with SoSIM and the measurements by Brandt et al. [2008] in the UV and VIS is better than 2% while discrepancies in the NIR are higher (Figure 3.11). A potential reason might be the non-spherical shape of snow grains that were no older than 24 hours. SoSIM is not capable to account for non-spherical grains since it utilises Mie-Theory. The asymptotic solution model by Kokhanovsky and Zege [2004] does account for this detail but is not capable to produce better results than SoSIM for this particular problem (tested but not shown). The reason might be that their model necessarily assumes one optical semi-infinite snow layer with vertically homogeneous snow grain size. TARTES would be capable to account for both, complex grain shape and stratification of the snowpack. However, a brief test showed good agreement but no improvement compared to the results archived with SoSIM. Further tests with TARTES are emphasised but could not be done during the time given for this study (note that TARTES was released in October 2014).

3.5   Conclusion

The Snow on Sea Ice Model SoSIM that was developed for this thesis is capable to investigate changes in the spectral and broadband albedo due to the influences of:

- snow microphysical parameters,
  - the effective snow grain radius r_{eff} or equivalent $\hat{S}$, the specific surface area (SSA)
  - thinning snow
  - snow density
- atmospheric composition causing diffuse radiation,
  - the aerosol optical depth (AOD) τ_{aerosol}
  - stratus clouds with optical thickness τ_{cloud}
- incidence angle of solar irradiance (SZA),
- and light absorbing impurities within the snowpack.

Model results of the spectral albedo were compared with the two-stream models SNICAR-online and TARTES, the asymptotic solution model by Kokhanovsky and Zege [2004] and field measurements of a snow covered sea-ice surface by Brandt et al. [2008]. The model comparison showed an agreement of the albedo reduction in the VIS due to additional BC absorption better than $\pm 1.1\%$. However, the model results reveal a slightly different sensitivity of the UV- and VIS-albedo to equal concentrations of BC in the snow. Other than in the VIS, the albedo is more sensitive to the microphysical properties of the snow near 1300 nm. There the models agree well, except for SNICAR-online which produces about 2% higher values. The relative differences in the NIR are generally higher, especially near the absorption band of ice and water. The calculated broadband albedo is compared with values from SNICAR-online and the parametrisation for the broadband

albedo from Gardner and Sharp [2010] and the agreement is better than about 1%.

The strong influences of the snow grain size and the solar zenith angle (SZA) on the spectral albedo of optically thick snowpacks found by Wiscombe and Warren [1980] have proven to be the dominating effects for the conditions evaluated here. The SZA should be precisely known for any measurement in order to be able to account albedo changes in the NIR to the influence snow grain size. At around 1300 nm, doubling the snow grain size decreases the albedo by about 20%, but a lower SZA may offset this change. Wavelengths in the VIS, around 450 nm, are rather insensitive to to the influence snow grain size. Therefore, measurements of the spectral albedo in both wavelength ranges could be used to derive the size of snow grains with the help the model results. It can be concluded that the expected albedo changes due to variations in snow grain size are in the order of 10% for conditions realistic for Arctic sea ice.

Atmospheric composition can diffuse the solar irradiance reaching the surface. This can be caused by an overcast with clouds or a very high aerosol burden. As irradiance becomes increasingly diffuse, the spectral albedo of a snow surface approaches that of an effective SZA of about 50° Wiscombe and Warren [1980]. If the true SZA is $> 50°$, a change from clear sky conditions to an overcast would lower the NIR snow albedo. The spectrally integrated albedo, however, increases in an overcast situation since the ratio of VIS to NIR irradiance at the ground increases. This weights the high albedo values in the VIS more than the low albedo in the NIR.

Additional absorption by BC in the snowpack reduces the albedo in the UV and VIS while it has almost no effect in the NIR. It could be possible to derive the concentration of BC in snow from spectral albedo measurements if changes in the VIS albedo can be exclusively accounted to BC absorption. However, problematic is the similar spectral signature of BC to that of thin snow on top of a dark surface [Warren and Wiscombe, 1980, Wiscombe and Warren, 1980]. With the model results obtained here it can be shown that the two effects closely resemble each other, e.g. for a snow depth of 6 cm and 40 ng/g BC in snow. These parameters are likely to occur on Arctic sea ice (Figure 3.9). Therefore, measuring BC concentrations is likely to be possible (and relevant) only for optically semi-infinite thick snowpacks. The model study suggests that realistic concentrations of BC (in the Arctic: < 40 ng/g) in a semi-infinitely thick snow layer cause an albedo reduction at 500 nm of about 1 to 2%, depending on snow grain size. Changes of the broadband albedo due to BC are even smaller. Modelling the isolated effect of adding 40 ng/g BC to pure snow resulted in a broadband albedo reduction of $< 1\%$, which is small compared to the effect of snow grain size.

The broadband albedo does not allow to separate different effects. In order to derive any snow parameter from spectral albedo measurements, the influencing parameters must be known with the priority listed in table 3.5, that is based on model calculations showing which albedo changes can be expected during measurements on Arctic sea ice. Parameters with high influence on the albedo have to be accurately known to infer others with smaller influence. A similar argumentation holds if parameters have to be assumed for modelling purposes. The thickness of an optically thin snowpack has to be accurately known. However, the albedo does not change significantly for a snow depths above 20 cm. Small changes of the density of most snowpacks has minor impact on the albedo ($\ll 1\%$). Grain size can probably be derived from spectral measurements by neglecting

Table 3.5: Importance of the snow and atmospheric parameters influencing the (spectral) albedo given with a priority with which they should be measured or derived from spectral albedo measurements.

Priority	Parameter	Source
1.	SZA	calculation from location and local time
2.	snow thickness	assumption or measurement
3.	optical thickness of clouds and aerosols	additional measurements
4.	snow grain size	retrieval from NIR albedo
5.	BC	retrieval from VIS albedo

the small effect of BC, if no high BC mass concentrations ($< 40\,\mathrm{ng/g}$) are expected. Changes of the snow grain size have a strong impact on the spectral albedo, thus if assumptions have to be made, the possible large uncertainties have to be accounted for. The re-simulations of the field-measurements showed, that the SZA should be accurately documented by at least $\pm 1°$ because of its strong influence on NIR albedo. This effect vanishes if no direct radiation reaches the snow surface, i.e. for an overcast sky. The re-simulations also demonstrated the complexity of reflectance of a real snowpack with a vertical structure featuring multiple optical thin layers. Nevertheless, simplifications of a snowpack's stratigraphy are often necessary for modelling. In this context, Picard et al. [2009] showed that the shape of snow crystals has an influence on the spectral albedo. However, the approximation of a diverse snow pack with different crystal shapes and sizes used in this study seems reasonable, since snow grain metamorphism reduces the complexity of grain shapes and the multiple scattering within the snowpack smears the angular dependence of scattering.

When modelling the hemispheric reflectance, or albedo, the exact angular distribution of the reflected radiation is not of particular interest, therefore a description of all snow grains as equally sized spherical particles is feasible [Grenfell and Warren, 1999]. The approximation is favoured by the fact that angular details in the phase function of complex snow grains are smeared by multiple scattering [Warren, 1982]. However, a high SZA or very thin snow reduce the number of scattering events within the snowpack, thus a model utilising the assumption of spherical grains should be limited. SoSIM was not used to model snow below a thickness of $1\,\mathrm{cm}$ and an SZA above $80°$.

4. Evaluation of airborne measurements of sea-ice albedo in the Arctic

In this section, data from airborne measurements provided by the Alfred Wegener Institute Helmholtz Centre for Polar and Marine Research (AWI) in Bremerhaven will be evaluated. Measurements were performed over sea ice in different regions of the Western Arctic and feature a set of quantities amongst which is the surface albedo. The measurement survey especially offers valuable information on the spatial variability of the surface albedo of Arctic sea ice.

An overview on the campaigns during which the measurements were conducted is given in Section 4.1. The broadband albedo measurements conducted during these campaigns are described and discussed in Section 4.2 together with the instrument specifications, calibration processes, post-processing and filtering of the data. Also the uncertainties involved in the measurement setup are analysed in this section, aiming to judge the quality of the data and whether snow parameters can be inferred. Images from a photocamera system are used for evaluations of the surface type and an algorithm for an automated classification the surface types snow, ice and open water is described in Section 4.3. The incentive is to characterise the influence of surface heterogeneities within the footprint of the instruments on the measured albedo. The auxiliary instrumentation aboard of the aeroplane is introduced in Section 4.4 and, finally, time series of the broadband albedo are discussed along with auxiliary data, such as sea-ice thickness, in Section 4.5.

4.1 Campaign outline and focus

The Polar Airborne Measurements and Arctic Regional Model Simulation Project (PAMARCMiP) is an airborne research project organized by AWI in cooperation with several other institutes and companies. Its incentive is to acquire knowledge about physical processes due to current environmental changes in the Inner Arctic, thus the reduction of uncertainties in regional and global model simulations. Measurements of sea-ice thickness, surface radiation budget, aerosol concentration and meteorological parameters are conducted on board the aeroplane Polar 5 in the Western Arctic north of 65° N, whereby the focus is on sea-ice thickness measurements. So far, four PAMARCMiP campaigns were implemented in the spring of 2009, 2011, 2012 and 2013, however the PAMARCMiP'13 campaign was discontinued, since technical problems with the sea-ice thickness instrument occurred [Conrady, 2013].

The Polar 5, a Basler BT-67 aeroplane, is based on the venerable Douglas DC-3 airframe, known from their formerly usage as "Raisin Bomber" and as transport aircraft during world war II. Polar 5 is rebuild and modernized by Basler Turbo Conversion (Oshkosh, WI) with state-of-the-art avionics, navigation systems and turbo prop engines for scientific and logistic purposes in the polar regions. The fuselage provides space for abundant scientific installations as modifications for the AWI include large belly retractable doors (roller-door cabins) several large openings in the cabin, wing stations for antennas and probes as well as a more powerful generator for electrical power. The aircraft has an operational range of more than 2500 km and the ability to land on skies.

For the analyses in this study, radiation measurements were available from the campaigns in 2009 and 2011. According to data filtering criteria (Section 4.2.3), sequences of flight tracks were chosen with three locations used as starting points for the flight tracks, namely Longyearbyen, Alert and Barrow. Longyearbyen is located at 78.22° N, 15.63° E on Spitsbergen, the biggest island of the Svalbard archipelago. Alert (82.45° N, 62.52° W) is located in Nunavut, Canada or more specifically on the northernmost end of Ellesmere Island at a height of 210 m above sea level. Barrow, Alaska (71.32° N, 156.60° W) is the easternmost site used and the northernmost city in the United States of America placed at a height of 11 m above sea level. Furthermore, Station Nord, Eureka, Resolute Bay, Sachs Harbour and Inuvik are used as starting points. The Russian drifting stations NP36, NP38 and NP40 were meant to be used for intermediate landing, but only NP36 was approached [Conrady, 2013].

4.2 Airborne broadband albedo measurements

The albedo is the quantity that will be featured in this evaluation. Parts of the other quantities obtained with the instrument package aboard Polar 5 will be analysed in order to support interpreting the albedo measurements. The shortwave radiation budget, or albedo (see Section 2.3.3), of a surface is calculated from measurements with two pyranometers of type Eppley Precision Spectral Pyranometer (PSP) (Eppley Laboratory Inc., USA) mounted at the top and bottom of the aeroplane fuselage (Figure 4.1).

The top pyranometer sits in the middle of the fuselage and measures the irradiance from the upper hemisphere, which can be interpreted as the direct and diffuse solar irradiance (Figure 4.2 top). In between the middle and rear third of the fuselage the downward facing pyranometer is situated (Figure 4.2 bottom), measuring the irradiance from the lower hemisphere, which can be interpreted as reflected irradiance from the surface. Both sensors are mounted with an angle relative to the hull such that they are almost in a level position when the plane is in the air, flying with regular speed. In the following, the Eppley PSP pyranometers and the handling of the measured data is described. This is carried out in order to gain an understanding of the quality of the obtained albedo data evaluated in Section 4.5.
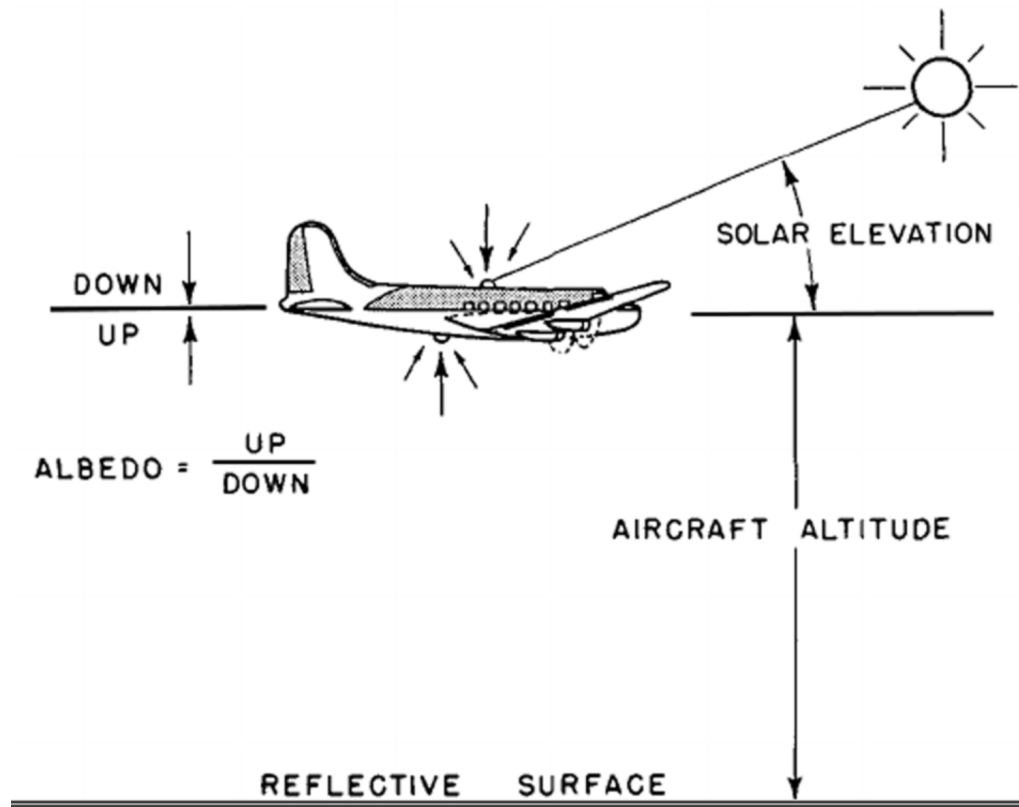
Figure 4.1: The Measurements setup for the airborne broadband albedo measurements with two Eppley PSP pyranometers mounted at the top and bottom of the fuselage of Polar 5. The albedo is calculated as the ratio of the measured upward and downward irradiance. Altitude of the aeroplane and attitude with respect to the position of the sun influence the measurements. Sketch modified after Predoehl et al. [1965]

4.2.1 Instrument specifications

The Eppley PSP Pyranometer is designed to fulfil the World Meteorological Organization (WMO) *First Class* specifications according to ISO 9060 for measurements of direct and diffuse, e.g. sun and sky, irradiance. It utilises a rectangular multi-junction wire-wound Eppley thermopile glued to the back of a sensor disk which is painted black with lacquer optimized for non-wavelength selective absorption. The energy absorbed heats the sensor disk and the attached side of the thermopile while the other side of the thermopile is in thermal equilibrium with the (cooler) metal body of the instrument. Due to the thermoelectric effect (Peltier-Seebeck effect), a voltage signal arises from the temperature difference at the two sides of the semiconductor pile. The Eppley PSP shows linear sensitivity in the order of $10\,\mu V$ per $1\,W/m^2$ with a deviation of $\pm 0.5\,\%$ over the range from 0 to $2800\,W/m^2$. This sensitivity changes by $\pm 1.0\,\%$ over an ambient temperature range from -20 to 40°C [McArthur, 2004]. A pyranometer is a hemispheric receiver, hence the sensor disk and shielding domes of the Eppley PSP are intended to ensure a cosine response to oblique rays. The manufacturer states an accuracy of the cosine response of $\pm 1\%$ between 0 to 70° from the zenith

Figure 4.2: Top and bottom view of Polar 5 showing the built-in positions of: a) top pyranometer, b) top pyrgeometer, c) bottom pyranometer, d) closed roller door with photocamera inside and e) snow-thickness radar (this instrument from Environment Canada was only installed during some flights in 2011). Photographs curtsey Dr. Gerit Birnbaum, AWI
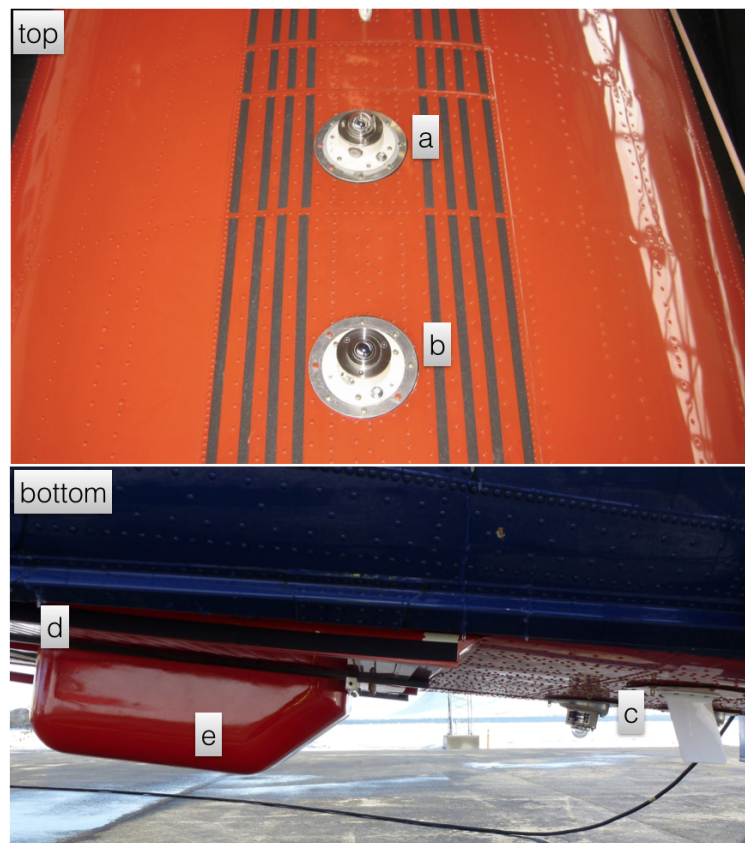
and ±3% from 70 to 80°. The design with two domes mitigates energy loss to the atmosphere due to longwave emission of the sensor disk. The domes are made of clear glass (Schott WG295) uniformly transparent for solar energy between 285 to 2800 nm, thus acting as a filter for thermal infrared. The wavelength range covers 99 % of the energy in the solar spectrum [van Leeuwen and Roujean, 2002].

4.2.2 Instrument calibration

For the campaigns in 2009 and 2011, the same combination of Eppley PSPs was used as top and bottom pyranometers. The serial numbers of instruments and information about the calibration results used to calculate irradiances from the instrument readings are listed in Table 4.1. The pyranometers were regularly calibrated in the summer of every second year. Calibrations on a regular basis are necessary because the sensitivity of pyranometers with this constructions principle may change [McArthur, 2004]. Because of their age of over 20 years and reported problems (scratches, condensation inside the domes) the two Eppley PSPs got replaced in 2012 and the last available calibration of both instruments is from August 2009.

The calibration procedure is done at the *Physikalisch-Meteorologisches Observatorium Davos* (PM OD), the WMO World Radiation Centre in Davos, Switzerland, with the local (latitude: 46.8143° N, longitude: 9.8458° W, altitude: 1588m) sun and sky radiation. Citing the calibration certificate, the pyranometers were calibrated against the readings from a World Radiometric Reference, which

Table 4.1: Serial numbers, built-in position and calibration results for PAMARCMiP campaigns in 2009 and 2011.

serial number	position	date of calibration	sensitivity µV/Wm^{-2}	uncertainty µV/Wm^{-2}
SN26954F3	top	10.08.09	8.04	0.10
SN26953F3	bottom	07.08.09	8.98	0.12

was realised as an absolute pyrheliometer (direct radiation) and a shaded pyranometer (diffuse radiation). During the comparison in August 2009, the instruments received global radiation intensities ranging from 636 to 957 W/m^2, with a mean of 832 W/m^2, from the sun at zenith angles ranging from 27.7° to 50.0°. The comparison was done during (near) clear sky conditions in July (2., 13., 16., 20., 27.-30.) and August (5., 6.). Since the two Eppley pyranometers do not show the same sensitivity, this calibration can be seen as an intercalibration between the instruments and has to be considered during post processing and calculation of the albedo.

According to the Solar Radiation Monitoring Laboratory at the University of Oregon [2000] (SRML), the accuracy of the calibration factor varies with SZA. An Eppley PSP that has been in the field for more than 20 years shows uncertainties of ±3 to 4% at SZA greater than 75°, whereas the uncertainty below 50° SZA is around ±1 to 1.5%. The latter matches the results of the calibrations at the PMOD of the two pyranometers used during the campaign. As reason for the lower accuracy of the calibration factor at higher SZA, deviations from the true cosine response due to imperfections of the domes and, especially for older instruments, scratches in the glass are supposed [SRML, 2000]. The deviation from true cosine response, therefore, can be a function of azimuth angle of the sun relative to the instrument's orientation. Test measurements with a similar pyranometer, a Kipp & Zonen CM21, showed a deviation from true cosine response reaching up to ±3% for SZA between 75 and 85° with a broad spread, while the average over all azimuth angles was about ±1% [personal communication K. Behrens, Deutscher Wetterdienst (DWD) Lindenberg (Feb. 2014)]. These observations match with the instrument specifications given by the manufacturer and it fulfils the WMO first class specifications. The cosine response of the instrument and its deviation from a true cosine response has a strong influence on the uncertainty of its sensitivity. Therefore, an uncertainty of ±3% will be assumed for the top pyranometer. The uncertainty as stated on the calibration certificate is not appropriate since most measurements were conducted during solar elevations $\theta > 70°$.

4.2.3 Post processing, corrections and filtering of the data

The voltage signals of the two pyranometers were logged at 20 Hz resolution with the central data storage system and a synchronised time stamp and geo-reference was added. In order to calculate the albedo from this data set, four calculation and correction steps have to be done during post processing. Completely processed data sets were available for the campaigns in 2009 and 2011, hence post processing was not a part of this study, except for data filtering. Nevertheless,

an understanding of the necessary steps is crucial when judging quality and uncertainty of the processed albedo data. This section will give an overview of these four post processing steps.

Conversion of the voltage signal: As a first step, the measured irradiances for the upper hemisphere $E_{\mathrm{m}}^{\downarrow}$ and $E_{\mathrm{m}}^{\uparrow}$ for the lower hemisphere are calculated from the voltage signals of the top and bottom pyranometer, respectively. For this, the measured signal is divided by the calibrated sensitivity of the respective instrument. Due to the different sensitivities of the two pyranometers, a calibration of the instruments or an intercalibration between them is always necessary in order to calculate the albedo.

The pyranometer sensitivities are not corrected for the temperature of the instruments. According to the manufacturer, the sensitivity can change by about $\pm 1\%$ between the warm ambient temperatures present during the calibration process and the low temperatures occurring during the measurements. Nevertheless, this effect is neglected. Furthermore, the measurements can be influenced by artificial heating of the instrument bodies connected to the fuselage of the aeroplane and longwave emittance cooling the sensor. However, it is assumed that this effect is well compensated by ventilation since most of the instrument body is exposed to the air stream. There is, in addition, an adjustment time of the instruments due to the thermal exchange between thermopile and instrument housing during which the measurements are biased. This occurs whenever the ambient temperature changes as occurring during ascend or descend to a different flight altitude. These sequences of the measurements will be filtered (see below).

Correction of instrument inertia: The second step is a correction of the irradiance signal for the inertia of the pyranometer which is mainly determined by two time constants. There is a short adjustment time of the thermopile to changing radiative flux of $t' \approx 1.0 \pm 0.1\,\mathrm{s}$ for a $1/\mathrm{e}$ relaxation. The recorded signal is a folding of the radiative flux and the response function of the instrument. Because the signal is sampled at $20\,\mathrm{Hz}$ resolution, the irradiance data corrected for the instrument inertia can be calculated with the Newtonian method [Freese, 1999]:

$$E_{\mathrm{m,corrected}} = E_{\mathrm{m}} + t'\frac{d}{dt}E_{\mathrm{m}}\,. \tag{4.1}$$

Correction of flight attitude: The third step is correcting the irradiance measured by the top pyranometer to the value that would have been measured by a levelled instrument. Because of the cosine law (Figure 4.3), the irradiance a pyranometer measures changes with the orientation of the receiving sensor disk to the sun. Ground based pyranometers are easily levelled, whereas the orientation of a pyranometer mounted on an aeroplane has to be concerned due to the pitch and roll movement, that still reaches variations of up to $\pm 5°$ for straight and level flight legs. A correction is possible because the flight attitude of the aeroplane is know from a combination of a high performance inertial navigation system (INS) and four global positioning system (GPS) receivers with sufficient precision. Airborne measurements of solar radiation only became feasible with the availability of those systems. Especially for high SZA $\theta > 60°$, often occurring during measurements
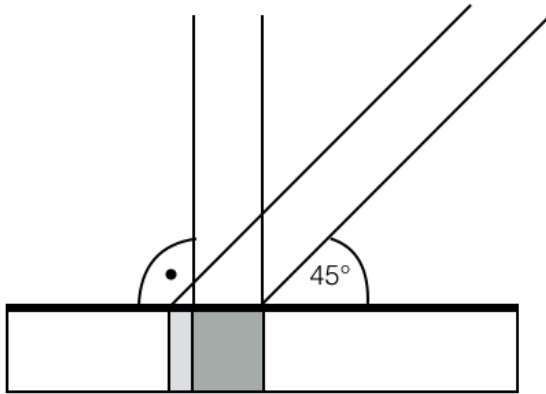
Figure 4.3: A narrow beam of radiation, e.g. the direct sun light, is distributed over a certain area. For lower incidence angles, the same radiation is distributed over a larger area than for a normal incidence angle. The cosine law describes the energy received by a unit area with changing incidence angle.

on the polar regions, the errors without a correction are high. Bannehr and Schwiesow [1993] found an error of 26% in global irradiance for an SZA $\theta = 80°$.

The problem occurs because of the different effects of direct and diffuse irradiance on the measurement signal with variations of the flight attitude. In good approximation, the diffuse sky or reflected irradiance has a homogeneous distribution within the upper or lower hemisphere, respectively. Hence, for overcast situations without direct radiation there would be no effect of small pitch and roll movements less than about 10°, e.g. without significant contributions from the other hemisphere to the signal from the instrument's field of view (FOV). The influence of aeroplane movements to the measured direct irradiance can be described with the flight attitude parameter [Freese, 1999]:

$$C = \frac{\cos(\beta)}{\cos(\theta)} \, , \tag{4.2}$$

where β is the angle between the surface normal of the sensor and the position of the sun as shown in Figure 4.4. The angle β can be calculated from the pitch and roll angles known from the INS [Freese, 1999]. The direct irradiance, E_{dir}, falling onto the sensor with a zenith angle β is weighted with the cosine of the SZA θ. The pyranometer registers the maximum signal when the sun is in the zenith of the instrument ($\cos(\beta) = 1$) and when the sun is at the instrument's horizon ($\cos(\beta) = 0$), the signal of the direct irradiance vanishes and only diffuse irradiance, E_{diff}, is measured. Figure 4.5 demonstrates this behaviour for the measured irradiance, E_{m}, of an upward facing pyranometer as function of the flight attitude parameter $\cos(\beta)/\cos(\theta)$ during a 90° turn with 20° roll angle. When the instrument turns away from the sun ($C < 0$), only E_{diff} is measured, whereas E_{m} equals the global irradiacne $E_{\mathrm{dir}} + E_{\mathrm{diff}}$ when the aeroplane returns to level flight $C \approx 1$. Due to this dependence on C, E_{m} can be split into a correlated part E_{dir} and an uncorrelated part E_{diff} with a linear regression. Freese [1999] derives as a good approximation of the behaviour of the measured signal with small deviations from horizontal flight:

$$E_{\mathrm{m}}^{\downarrow} \approx E_{\mathrm{diff}} + E_{\mathrm{dir}} \cdot \frac{\cos(\beta)}{\cos(\theta)} \, . \tag{4.3}$$

In order to correct the time series of $E_{\mathrm{m}}^{\downarrow}$ for measurements from a not levelled instrument, the time series is split into sequences. There is a small but unavoidable movement of the aeroplane during every sequence and the pyranometer takes different positions relative to the sun such that there is
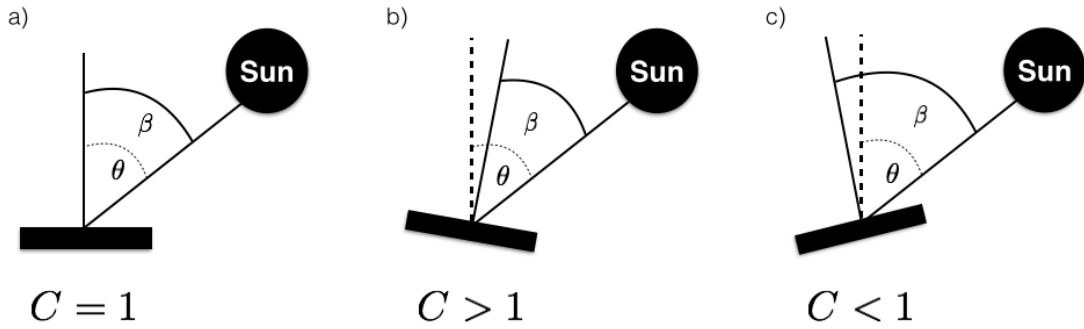
Figure 4.4: Behaviour of the flight attitude parameter C for a) level instrument; b) surface normal of the sensor tilted towards the sun; c) sensor tilted away from the sun.

a correlation of C with the measured irradiance similar to Figure 4.5 but not necessarily spanning the whole range of C. A linear regression is calculated for every sequence individually and the sum of the intercept and slope of the resulting linear regression line equals the correct $E^{\downarrow}$ [Freese, 1999]. This regression method resembles a running average, therefore temporal and spatial resolution is reduced. Also the linear relation between measured irradiance and flight attitude parameter can be used to quantify instrument uncertainties such as linearity of the thermopile and cosine response [Freese, 1999].

The actual orientation of the sensor mounted to the fuselage does not necessarily has to match the INS values of the pitch and roll angle. There might be a static mounting offset η, called *built-in error*, to the angle β that makes the attitude correction dependent on flight direction relative to the sun azimuth. This offset has to be calculated from the angular dependence of the irradiance measured during a special rectangular flight pattern with flight tracks parallel and perpendicular to the sun azimuth. The offsets for pitch and roll obtained by this method are assumed to be accurate. Thus, by subtracting the offset η from β, a correct $E^{\downarrow}$, as measured by a level instrument, can be calculated with the regression method.

Unfortunately, the described flight pattern could not be evaluated for the campaign PAMARCMiP'09, because of a significant influence of clouds. The mounting offset is therefore unknown. Due to the cosine law, quite a large error arises from a built-in error of a few degrees. In order to be able to correct the measurements, η was estimated in post-processing as an average of mounting offsets that were calculated from data of two other campaigns with the same aircraft and instrument. The roll offset was the same for these campaigns but the pitch angle was different by about $1°$. Hence flights parallel to the sun azimuth were affected by this inaccurate correction. Flights perpendicular to the sun, however, are not affected. The combination of pitch and roll angles β with the correction for the offsets η has a maximum error $\Delta\eta$ equal to the maximum standard deviation of either the pitch or roll angles taken into account in order to find the built-in error from other campaigns. By extending the definition of C for the built-in error, Equation 4.2 becomes:

$$C = \frac{\cos(\beta - (\eta \pm \Delta\eta))}{\cos(\theta)} \; . \tag{4.4}$$

In Figure 4.6, $(C-1) \cdot 100\%$, i.e. the error arising from a false correction of the measured irradiance,
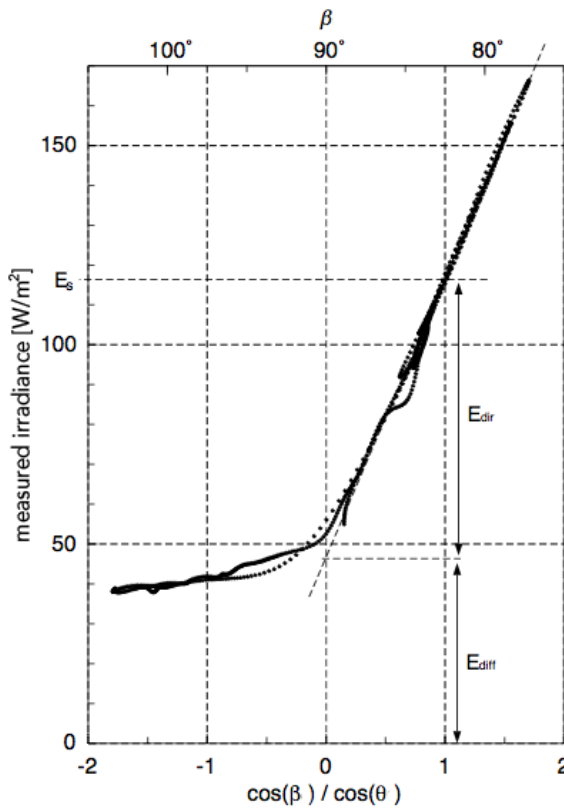
Figure 4.5: Dependence of the measured irradiance on flight attitude parameter $C = \frac{\cos(\beta)}{\cos(\theta)}$. The graph shows data points recorded during a turn while the sun was at $\theta = 82.5°$. The sensor is tilted away from the sun and the signal drops, followed by an increase in measured irradiance while the sensor was pointed towards the sun. During horizontal flight, $C \approx 1$. A correct $E^{\downarrow}$ can be calculated from intercept and slope of the linear regression line. This example is taken from Freese [1999].

is plotted for different SZA as a function of $\Delta\eta$ for the case $\beta + \eta = \theta$. A linear dependency of ΔC is found within the relevant interval of the built-in error, $-2.5° < \Delta\eta < 2.5°$.

Data filtering   As fourth step, segments of the flight legs have to be excluded from further evaluation as they possibly yield inaccurate data. On occurrence of the following events, segments of the time series were excluded or masked within the final data product:

- Clouds are detectable as fast changes in the pyranometer signal that are clearly distinguishable from the smooth changes due to the movement of the aeroplane. Single clouds and overcast situations change the angular response of the measured signal and can be detected during data processing. Cloud events should also be stated in the flight log-file.

- Curves and ascend or descend segments of the flights cannot be corrected for the attitude with the same accuracy than level flights and have been removed from the evaluation within this study.

- The received irradiance from both hemispheres changes with altitude. Flights at high altitudes cannot be used for measurements of surface albedo for the following reasons:

At higher altitudes, the path through the atmosphere for radiation reaching the downward looking pyranometer as reflected radiation from the surface, gets longer. Gaseous absorption as well as scattering at air molecules and aerosols can have a significant influence on the measured irradiance
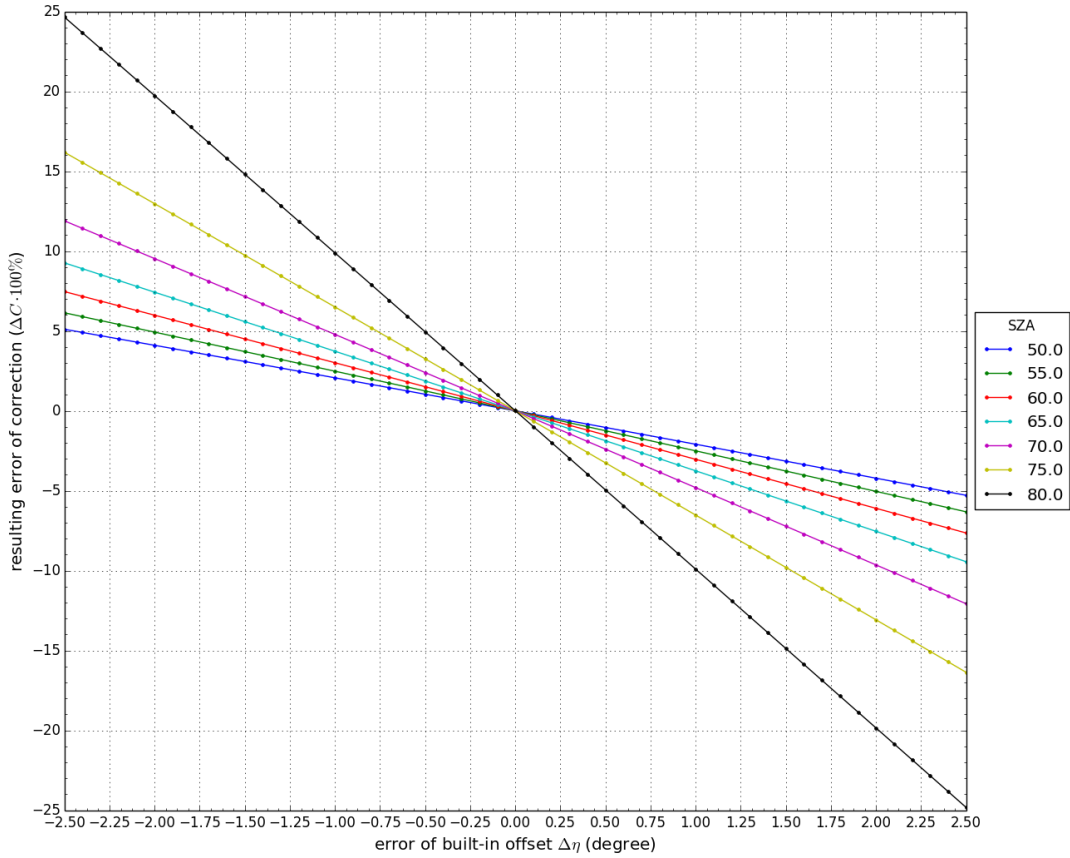
Figure 4.6: The error $\Delta C = C - 1$ (in %) that arises due to an error $\Delta \eta$ in the correction of the built-in offset η. C is used as defined in Equation 4.5. ΔC is plotted for different SZA.

[Wendisch et al., 2004]. It follows from the Lambert-Beer law that downward sky and sun irradiance increases with altitude since the air mass is decreased. Wendisch et al. [2004] find that these two effects do not necessarily balance each other. Rather, they observed a non-linear increase of the measured albedo with increasing altitude over open water and homogeneous land surfaces. They suggest a radiative transfer model based correction:

$$\alpha(\lambda, z_{\text{flight}}) = \frac{\alpha_{\text{calc}}(\lambda, z_{\text{surface}})}{\alpha_{\text{calc}}(\lambda, z_{\text{flight}})} \cdot \alpha_{\text{measured}}(\lambda, z_{\text{flight}}), \tag{4.5}$$

with the albedo $\alpha_{\text{calc}}(\lambda, z)$ evaluated right at the surface and at flight altitude. The true surface albedo has to be found by an iteration process, but the method is insensitive to small deviations [Wendisch et al., 2004].

Figure 4.7 shows broadband surface albedos calculated with SoSIM as a function of altitude. Most striking, a decrease of the calculated albedo with altitude is found above a snow surface in contrast to the calculations and measurements by Wendisch et al. [2004] above darker water and land surfaces. In their case, scattering within the atmosphere added a substantial part to the reflected energy. Hence, the measured albedo is a mixture between the relatively low surface albedo and higher *air albedo*. However, compared to snow, the albedo of air is lower and absorption, as well as, scattering within the column of air between surface and flight altitude, reduces the upwelling radiation. Based
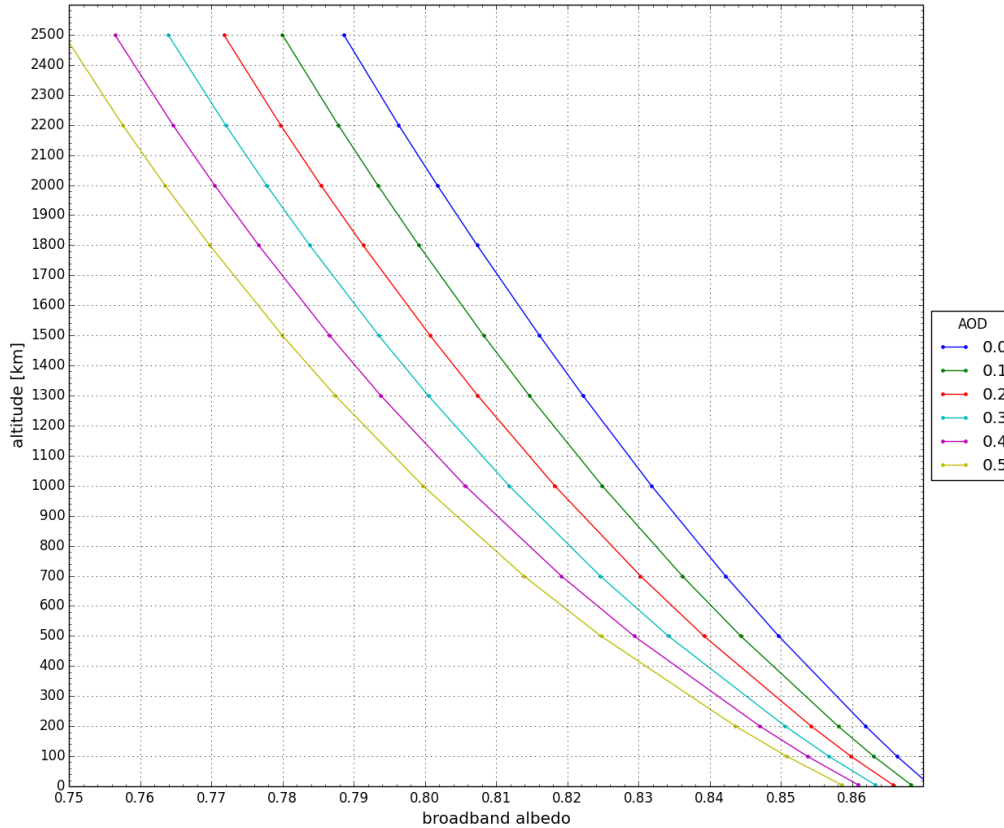
Figure 4.7: Change of the albedo of a homogeneous snow surface that is calculated at different altitudes (in km). Values are simulated with SoSIM for clear-sky conditions and different AOD.

on the calculations shown in Figure 4.7, an albedo change of -0.5 to -0.7% per 100 m increase in altitude is found. This result can be supported with measurement data. From two overpasses of the same measurement track within less than one hour at about 100 and 2200 m above ground level (AGL), a 11% decrease of the measured albedo is found (not shown). This rate of -0.5% per 100 m fits to the predictions of the model. However, discrepancies in the model atmosphere setup and aerosol profiles as well as the larger footprint of the measurement at higher altitudes (see Section 4.3) introduce some uncertainty to this comparison. A realistic altitude dependence of surface albedo can only be determined by a model with accurate knowledge of atmospheric profiles of gases and aerosols [Wendisch et al., 2004] – otherwise, a correction will introduce new uncertainties.

Because of the relatively low and constant altitude (90 ± 20 m AGL) of all sea-ice survey flights done together with sea-ice thickness measurements with the EM-Bird System (see Section 4.4), no correction of the albedo for effects of the atmosphere is done. The expected under-representation of the surface albedo is small ($< 1\%$) compared to other uncertainties of the measurement and it is given a relative value of $-0.5 \pm 0.5\%$. Nevertheless, the data from higher flight legs is excluded from the evaluation in this thesis.

4.2.4 Discussion of the measurement uncertainty

In this section, the overall uncertainty of the airborne broadband albedo measurements will be estimated according to the previous discussions. The broadband albedo is the ratio of two quantities measured by individual instruments. Measuring the downward direct and diffuse solar irradiance with its strong angular dependence involves more sources for uncertainties than the upward diffusely reflected irradiance. Uncertainties arising from the correction of non-levelled instruments therefore only apply for the top pyranometer. Another part of the albedo's uncertainty is the sensitivity of the two instruments. The sign of the individual uncertainties, ζ_i, is unknown, therefore the rules of uncertainty propagation state for the total uncertainty ζ of the measurement:

$$\zeta = \sum_i \zeta_i \,, \tag{4.6}$$

as it has to be assumed that individual uncertainties do not counteract but maximise the error of the calculated ratio. Thus, by adding the individual uncertainties for the instruments' sensitivity and the flight attitude correction, the quantifiable uncertainty caused by the individual measurements can be calculated.

The fact that the sensitivity of the pyranometers may change with temperature will be neglected. The instruments' temperatures are not measured and the true temperature dependence has not been evaluated, e. g. in laboratory tests. The manufacturer states a change of about 1% and it is likely that both instruments show a similar behaviour. Therefore, this uncertainties are assumed to cancel out when calculating the ratio of the instruments readings. Further, due to effects of the atmosphere, it is likely that the albedo measured at an altitude of around 100 m AGL is by $0.5 \pm 0.5\%$ too small. This factor may be added to the total uncertainty of the measurement.

As result, the albedo measurements from PAMARCMiP'11 have a total uncertainty of $\zeta_{\mathrm{P'11}} = (3.0 + 1.1)\% = 4.1\%$ and those from PAMARCMiP'09 have a total uncertainty of $\zeta_{\mathrm{P'09}} = (3.0 + 1.1 + 7.0)\% = 11.1\%$. The uncertainty for the campaign in 2009 is lager than in 2011 because of the missing calibration flight for the attitude correction and the resulting extra uncertainty. The exact sign and magnitude of the uncertainties may depend on the orientation of the sensor relative to the sun. Therefore, the instantaneous contribution of this uncertainty may vary, especially with flight direction (azimuth dependence of uncertainty), and is no static offset that can be easily corrected. As a consequence, small albedo changes cannot be evaluated from these airborne albedo measurements.

Additionally, dirt and ice do accumulate on the unprotected domes of the pyranometers during take off and flight. This may cause a significant measurement error, but its magnitude and sign is hard to quantify. Other measurement equipment and parts of the aeroplane can loom into the FOV of the pyranometer. Only the yaw rudder and the snow-thickness radar (Figure 4.2) are known to have possibly a small influence in the measured irradiance. These parts have a rather low profile within the FOV of the pyranometers and no significant bias to the measurements is expected.

4.3   Investigating the influence of surface inhomogeneities with photographs

The most abundant surface type in the sea-ice region is snow. As one of the goals of this thesis is to understand the influences of snow properties on the albedo of sea ice, a comparison between model values and measurements is of interest. Whereas SoSIM is a one dimensional model and assumes horizontal homogeneity for the reflecting surface, real sea ice shows surface heterogeneities of various scales. The wind and ocean current driven sea-ice dynamics often causes the ice to break up. In some places open leads form that will refreeze after some time with thin, smooth ice and eventually will accumulate snow again (Section 2.1). In other places the ice floes are pushed together or over one another forming very rough surfaces that can cause an angular dependence of the reflected radiation and shadowing of parts of the surface. The range of albedo values found on the sea ice covered ocean stretches almost over the entire interval from close to zero to almost unity.

Photographs may reveal detailed spatial information about the surface. Series of photographs are automatically taken during some of the measurement flights with a Canon EOS 1D Mark III (Canon Inc., Japan) digital single-lens reflex (DSLR) camera. It is mounted downward looking in one of the roller-door cabins in the fuselage of Polar 5 about 1 m in front of the bottom pyranometer, as shown on the left side of Figure 4.2b).

The camera is operated with a wide angel lens with focal length $f = 14.0$ mm. Its FOV depends on the focal length and the dimensions of the sensor, which in the case of the Canon EOS 1D Mark III has an APS-H format of 28.1 mm by 18.7 mm. The FOV for the diagonal of the sensor chip $d_{\text{chip}} = \sqrt{\left(\, (28.1\text{mm})^2 \,+\, (18.7\text{mm})^2\, \right)} = 33.8$ mm is given by:

$$\text{FOV}_{\text{cam}} = 2 \arctan\left(\frac{d_{\text{chip}}}{2f}\right) \approx 100.6° \,. \tag{4.7}$$

The photographs taken with this camera setup are used to automatically determine which surface types, i.e. water, ice or snow, were present underneath the aeroplane. Their spatial distribution determines the measured albedo and knowledge about the areal coverage with each surface type is very useful information for the interpretation of the measured albedo and for a comparison between measurements and snow-albedo model.

One quite typical situation is shown in the photograph (Figure 4.8): multiple large and small ice floes, some are loose and others are frozen together, covered with a bright snow layer just thin enough so some contours are still visible. In between the large floes are some leads with open water and partly covered with a new and very thin ice cover. Open water looks almost black when viewing it from directly overhead. The new ice appears greyish, with darker shades of grey where the ice is thin and almost entirely translucent, changing to a lighter grey where the ice grows thicker.

The heterogeneity of surface types makes it very likely that very different degrees of surface reflectance are found within the footprint of the downward facing pyranometer. The resulting signal then is a weighted spatial average – a folding of characteristics of the sensor with the spatial distribution and magnitude of changes of surface albedo. As an example, given 80% of the area is covered with snow having a high albedo of 0.86 and 20% are open water with a very
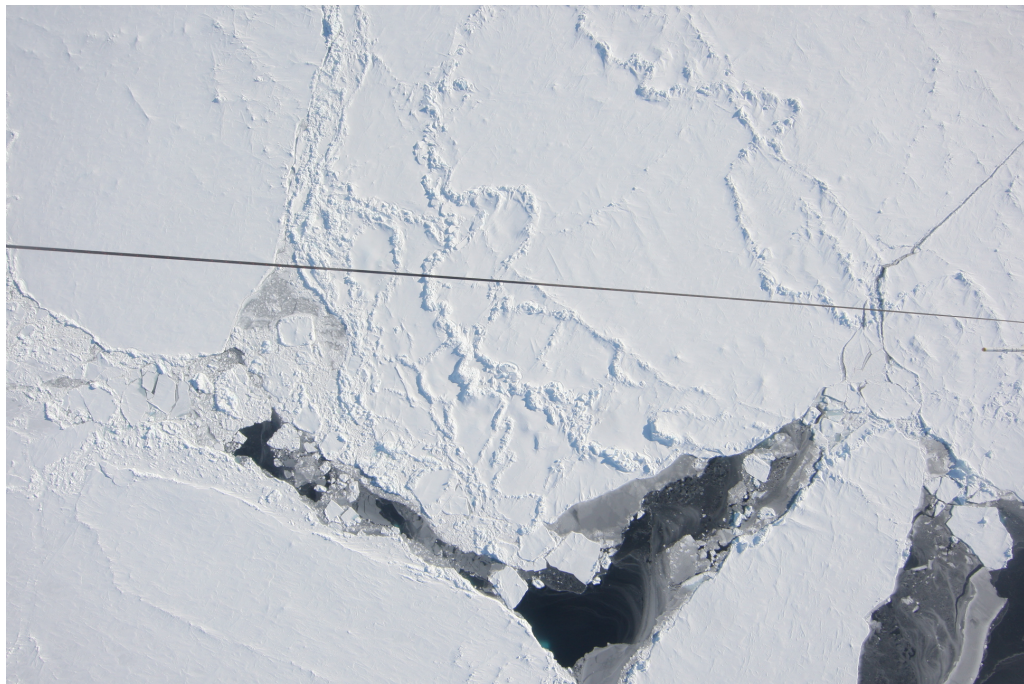
Figure 4.8: This photograph was taken with the camera system during PAMARCMiP'11 on 14.03. and it shows a very typical sea-ice surface with parts of open water, new ice and snow covered thick ice floes. The dark line crossing the image is the towing cable of the EM-Bird.

low albedo of 0.05 (compare typical albedo values in Figure 1.1) results in a measured albedo of $0.8 \cdot 0.86 + 0.2 \cdot 0.05 = 0.7$ (assuming the areal fraction corresponds with the cosine weighting of the pyranometer signal). A comparison between a mixed surface albedo and model values, varying with snow age and LAI content (Section 3.3), might lead to false conclusions. Therefore, it would be best to accompany the measured albedo signal with information on areal coverage of the three dominating surface types snow, bare ice and open water. The realisation for an automated photograph evaluation developed for this thesis will be described in the next section. Note that all available data originates from the time between end of March and beginning of May – the Arctic spring. Surface conditions are even more diverse in the summer months when melting snow and melt ponds are present on the ice. Summer conditions are not treated in this study.

4.3.1 Algorithm for automated photograph evaluation

The algorithm utilises the red and blue colour channels of the photographs taken with the DSLR camera to identify three surface types from distinct brightness differences. It is a fast pixel wise threshold method that calculates binary masks giving information about the relative area covered by one of the surface types snow, ice or water and also shadowed areas in the vicinity of ridges. Threshold value based classifications are simple but widely used approaches [Kidder and Haar, 1995].
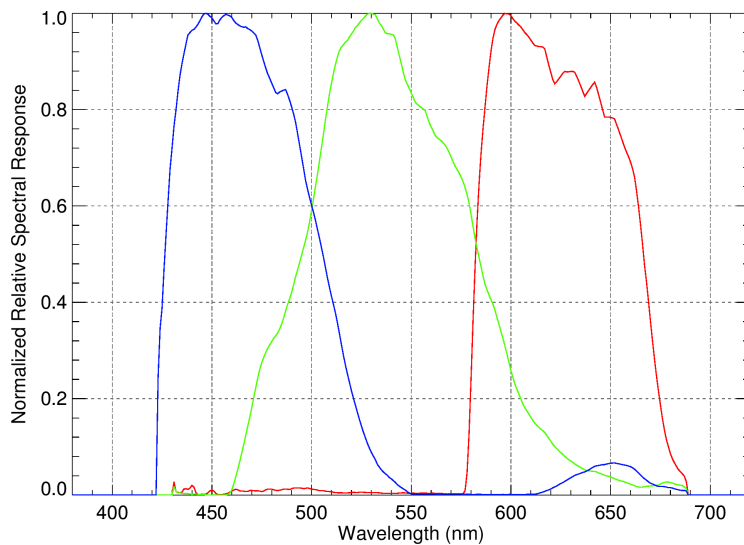
Figure 4.9: Spectral response of JPG images taken with a Canon PowerShot G10. A reflecting plane lit by a monochromatic light source (Bentham monochromator) was captured with fixed exposure and white balance. Each colour channel is normalised with its maximum response. Figure and data courtesy of Christine Pohl, IMuK 2014.

Not only brightness differences as in black and white images can be seen, also spectral information is available from the photographs. Each of the red, green and blue (RGB) colour channels gives pixel wise information about how much light from a certain wavelength band, e.g. a colour, was received by the complementary metal-oxide-semiconductor (CMOS) sensor of the camera. Bandpass filters in front of the sensor pixels, semiconductor response and image processing add up to the spectral sensitivity of the camera. The spectral sensitivity of a camera, a Canon PowerShot G10 with a charge-coupled device (CCD) sensor, used for scientific purposes at the IMuK was measured in the laboratory with a Bentham monochromator (Bentham Instruments Ltd, UK) at 1 nm resolution. Figure 4.9 shows the normalised spectral response of the colour channels in the wavelength range $300 \leq \lambda \leq 700$ nm, indicating that the blue and red channels are responsive in two separated wavelength bands. Therefore they can be used to identify the spectral behaviour of the reflected radiation, which for ice (Section 2.3) means more absorption and less reflection in the red part of the visible spectrum than for shorter wavelength (blue light).

The algorithm works as described in the diagram, Figure 4.10. Step **a** reads the red and blue colour channels as 2 dimensional arrays of count values from an 8 bit JPG image and also calculates and stores the difference between the count values of the blue and red channels in one array. Count values range from 0 (darkness) to 255 (saturation). The JPG format was chosen over RAW images for reasons of storage capacity needed for the image sequences (about 1/5) and speed of the computation. A higher bit rate does not improve the accuracy of the classification. The algorithm could also handle RAW images with higher bit rates but the given threshold values are specific for 8 bit JPG images as they were found in a tuning process with visual control of the outcome of the classification.

The algorithm is written in Python and utilises the concept of data masks to ascribe a pixel to one of the surface types. In step **b** a mask is used to exclude a certain part of the image from the evaluation. As discussed above, during some flight legs of PAMARCMiP'11 a snow thickness radar was mounted underneath the aeroplane near the roller doors (see Figure 4.2). Therefore the red hull
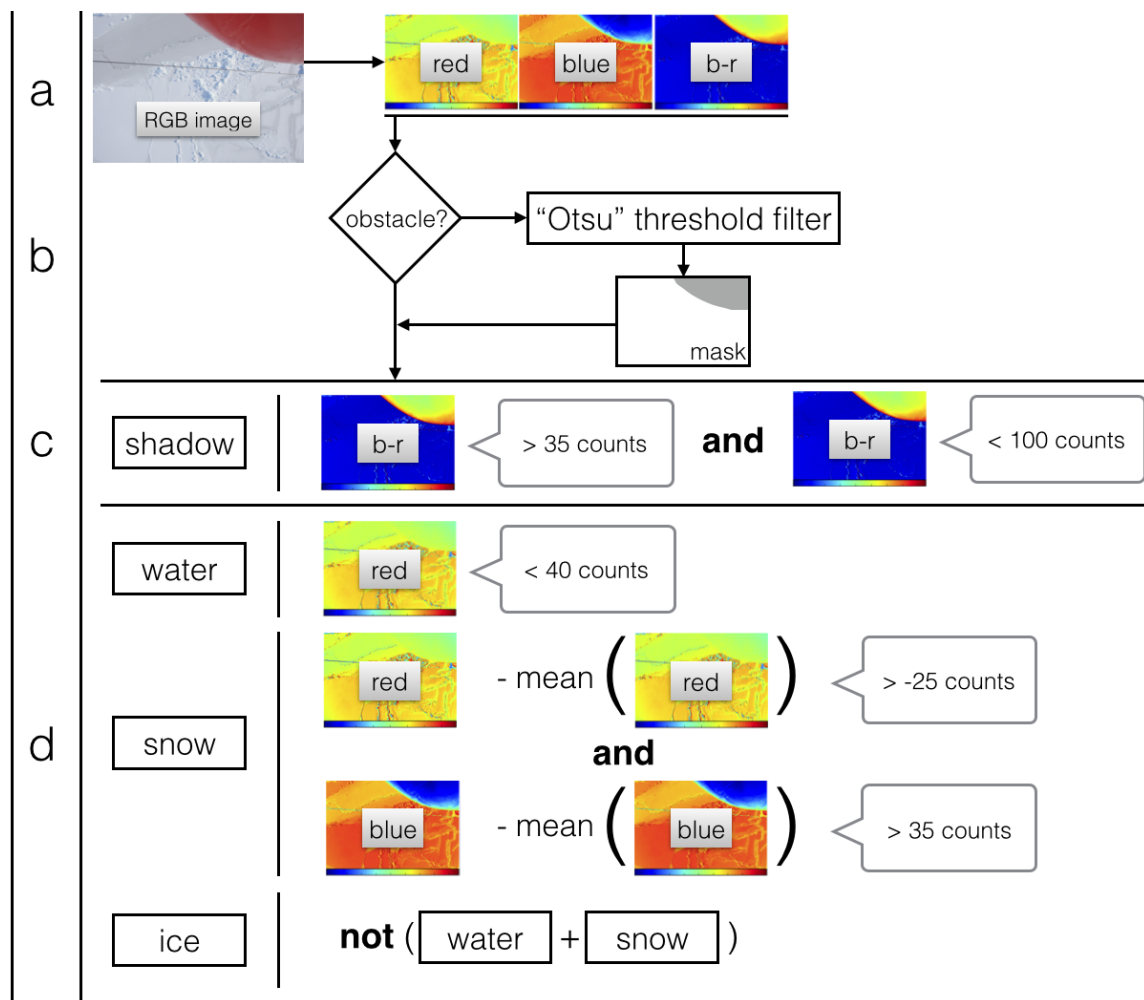
a RGB image → red blue b-r

b obstacle? → "Otsu" threshold filter → mask

c shadow: b-r > 35 counts **and** b-r < 100 counts

d water: red < 40 counts

snow: red − mean(red) > -25 counts **and** blue − mean(blue) > 35 counts

ice: **not** (water + snow)

Figure 4.10: Diagram of the photograph evaluation algorithm. The count values (brightness) of the red and blue colour channels of an RGB image are used, as well as the difference (b-r) of their count values. Shadows are detected and pixels are classified as water, ice or snow according to threshold values of the counts. Thresholds were found in a tuning process.

of this instrument is visible in the right top corner of the respective photographs. Note that flight direction is to the left side of the photographs and the rear of the aeroplane is to the right. This obstacle, if present, can be detected by an algorithm often used in image processing to separate image foreground and background known as Otsu's method [Otsu, 1979]. The classification of the pixels is done in steps **c** and **d**. A Pixel belongs to exactly one surface class (snow, ice, water). With the occurrence of ridges, parts of the surface might be shaded behind outstanding features (sails) depending on the position of the sun. Shadows are detected in step **c** as a fourth, individual class. This utilises that shadows have a well defined peak in the histogram of the $blue - red$ image, e.g. shadows are darker in the red channel than they are in the blue channel. Sails appear blueish if one looks into the shadow since the snow transmits more blue than red light. The relevant range of count values that can identify shadows is bracketed by two criteria (see Figure 4.10). A possible influence of shadows on the albedo will be discussed in Sections 4.5 and 4.6. In step **d**,
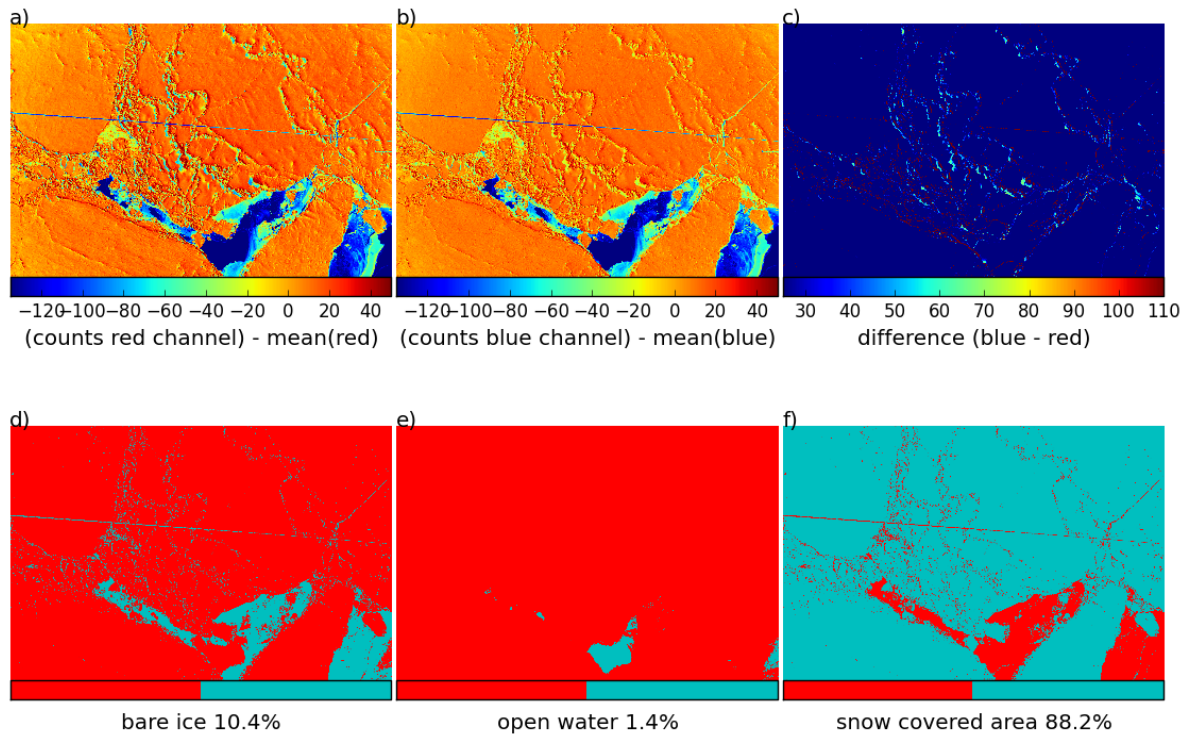
Figure 4.11: Results of an analysis of the photograph shown in Figure 4.8 with the described
algorithm. The images in a) and b) show the red and blue colour channel reduced by the
respective mean value. Image c) shows the difference of the count values from the blue to the
red channel from which shadows can be detected. Images c) through e) show the resulting
classification of each pixel as ice, water and snow, respectively. The areal coverage with each
class is denoted in the image captions.

the classification is done starting with water surfaces. They will appear very dark, with the best
contrast in the red channel. The identification of snow and ice surfaces is much more difficult and
for some cases even impossible with the given information. On the one hand, snow will include
the brightest pixels, but for complex surface structure of the snow layer, there can be significant
brightness variations. Also the photographs show vignetting and therefore a smooth snow surface
will appear darker in the image periphery compared to the image center. On the other hand, ice
may appear in a relatively bright light grey when it grows thicker. Air and brine inclusions can be
effective scatterers (Section 2.1). The algorithm uses both colour channels to improve the contrast.
Underexposure is a problem for threshold based classification. This is solved by subtracting the
mean count value of the channel from each pixel. Snow surfaces are classified by combining two
conditions, one for each colour channel with a logical *and*. Finally, every pixel that has not been
masked as either snow or water is classified as bare ice.

The algorithm performs well for situations with high contrast like the one shown in Figure 4.8.
Situations with closed snow covers but strong brightness variations can cause false classification of
the darker areas as ice. Wide and smooth areas of light, greyish nilas eventually get confused with
snow.

The result of a classification of the photograph (Figure 4.8) is shown as an example in Figure 4.11. The percentage of the total observed area covered by each class has been evaluated by counting the pixels of the respective mask and dividing it by the total number of pixels of the image (excluding masked obstacles). Theses numbers should not be interpreted in terms of a precise measure but they serve as an indicator for rather homogeneous or heterogeneous surface conditions which proofed as valuable extra information for the interpretation of the measured albedo. This data will be used in Section 4.5.

4.3.2   Discussion and interpretation of different instrument footprints

The datasets obtained with the photograph evaluation algorithm will be discussed along with the measured albedo and sea-ice thickness in Section 4.5. An interpretation of the pyranometer signal along with the spatial information captured with the photocamera makes it necessary to understand the different footprints of both systems.

The camera has a $\text{FOV}_{\text{cam}} \approx 101°$ (see calculation above) and its geometrical footprint can be calculated straight forward. The pyranometer has a theoretical FOV of 180° giving it an infinite footprint. Due to the fact that the received radiance is cosine weighted, most of the irradiance signal in fact comes from a narrower FOV. This has been evaluated by numerically integrating finite the solid angles elements $d\Omega = \sin\theta d\theta d\varphi$ weighted with the cosine of the SZA over all azimuth angles and, in increments of 1°, from to the zenith to the horizon. The signal of spherical caps has been calculated by integrating from the zenith up to a certain angle towards the horizon, e.g up to an angle $\theta = 0.5 \cdot \text{FOV}_{\text{cam}}$. Calculating the ratio of this spherical cap to the full hemisphere gives a measure of how much of the total signal of a perfect hemispherical receiver is accounted for (see Figure A.1 in the Appendix). In Figure 4.12 the geometrical footprint of the camera is compared with footprints for a FOV of 100°, 120° and 150°. Theses FOV account for approximately 60%, 75% and 93% of the irradiance signal, respectively, received by a downward looking pyranometer at an image distance equal to the average flight altitude $h = 90\,\text{m}$ AGL. The diameter of each footprint is given by:

$$d = 2h \tan\left(\frac{\text{FOV}}{2}\right) . \tag{4.8}$$

Hence, about 60% of the irradiance signal received by the bottom pyranometer (dark circle in Figure 4.12) corresponds to the surface that can be visually estimated from photographs (red rectangle). For 75% of the signal it is likely that the surface is similar to the photograph although the irradiance is reflected from an area already twice as large as the one with the diagonal of the photograph. The missing 25% of the signal then emerge from a much larger area (compare green circle in Figure 4.12) and an influence of significantly different surface features is possible, e.g. more open water than identified by the automated evaluation of the photograph.

With a speed over ground of about $50\,\text{m/s}$, taking one photo every $3\,\text{s}$ will give an overlap of the images, reducing the area of uncertain surface type to the area about $60\,\text{m}$ left and right from the middle the flight track. For the campaign PAMARCMiP'09 there is only one image each minute while for PAMARCMiP'11 photographs are available every $10\,\text{s}$.
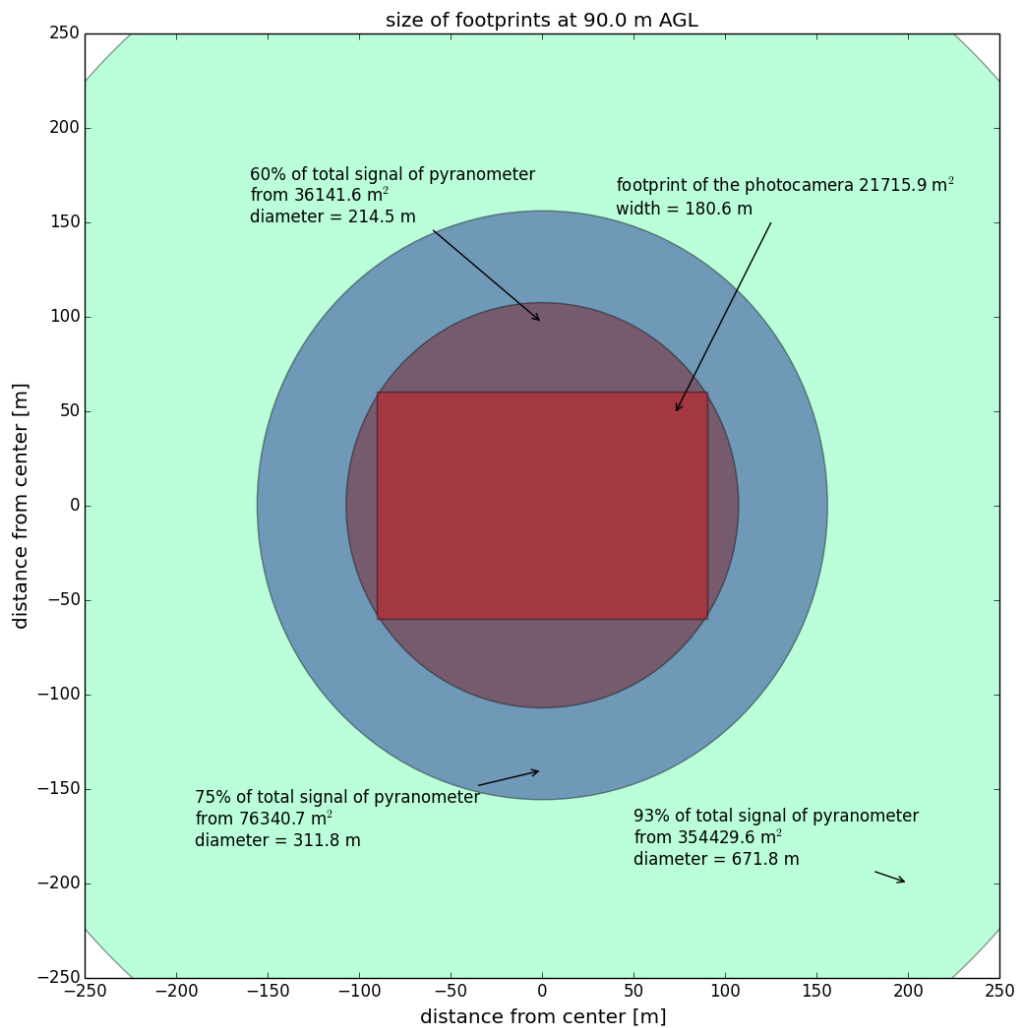
Figure 4.12: Geometrical footprints of the photocamera (red square) and the pyranometer (circles). The pyranometer footprints are shown for FOVs of 100°, 120° and 150° and account for approximately 60%, 75% and 93% of the irradiance signal, respectively.

4.4 Additional measurement systems

Besides the albedo measurements and photocamera system, there is a set of instrumentation measuring parameters of atmospheric state, airborne pollutants and surface conditions, with a strong focus on sea-ice thickness measurements with an EM-Bird system. Some of these measured parameters can yield additional information, useful for the interpretation of the albedo. The instrumentation aboard Polar 5 is arranged for specific scientific purposes. An overview of the changing equipment during the campaigns can be found in Herber [2012]. The instruments that delivered data used in the next sections are described in more detail in the following.

Meteorological parameters as pressure, humidity and temperature, as well as wind speed and direction are evaluated here to check the stability of the conditions during the measurement flights. An AIMMS-20 (Aventech Research Inc., Canada) sensor mounted below the right wing of Polar 5 measured the conditions at flight altitude and a dropsonde launcher delivered vertical profiles giving information about the actual stratification of the generally stable atmosphere.

Stone et al. [2010] make use of the sophisticated instrumentation for aerosol measurements aboard of Polar 5 during the campaigns. The *aerosol rack* contains four instruments, which are measuring atmospheric aerosols, namely a NOAA Continuous Light Absorption Photometer (CLAP), a Model 3563 Integrating Nephelometer (TSI Inc., USA), an Ultra-High Sensitivity Aerosol Spectrometer (UHSAS, Droplet Measurement Technologies, USA) and a Single Particle Soot Photometer, SP2 (Droplet Measurement Technologies). The SP2 is able to measure BC mass concentration, as well as the size and absorption cross section of single BC particles. See the paper of Schwarz et al. [2006] for more detailed information about the SP2. Additionally, an 8-channel Sun photometer system with a solar tracker measures aerosol optical depth (AOD), see Stone [2002] and references therein for more information on this system. Conclusions drawn from these measurements will be cited in the following discussion.

Information on surface conditions are most useful for the interpretation of the measured albedo. A Heitronics KT 19 infrared pyrgeometer (Heitronics Infrarot Messtechnik GmbH, Germany) measures the surface temperature and is used to check whether the temperature at the surface approached the melting point. The KT 19 has a circular footprint of about 3 m in diameter at an altitude of 90 m AGL. Its data is available as a 30 s average.

Further information about the character of the surface is derived from sea-ice thickness measurements with the EM-Bird system. The EM-Bird is a torpedo-shaped 3.5 m long body towed with a cable about 60 m below the aeroplane in an altitude of about 20 m above the sea-ice surface. Sea-ice thickness sounding with the EM-Bird system takes advantage of the very low electrical conductivity of sea ice (0 to 50 mS/m), while sea water is a very good conductor (2400 to 2700 mS/m). The EM-Bird generates a low-frequency primary EM field by its transmitting coil. The EM field penetrates the sea ice almost unaffected, while it generates eddy currents in the sea water below the ice. These eddy currents, in turn, induce a secondary EM field whose strength is measured with the receiving

Figure 4.13: The EM-Bird system measures the distance h_w above the ice-water interface as the field strength of a secondary EM field and the distance h_i above the ice with a laser altimeter. Difference of distances gives the ice thickness z_i. Here, σ denotes the conductivity of the media. From [Haas et al., 2009]

coil of the EM-Bird system. The strength of the received field is directly related to the distance h_w between the receiving coil and the interface between sea water and ice underside Haas et al. [2009]. This is sketched in Figure 4.13. In order to determine the thickness of the sea ice z_i, a laser altimeter measures precisely the height h_i of the EM-Bird above the sea ice. The difference $h_w - h_i$ gives z_i. In the case of snow covered sea ice, it is not possible to discriminate thickness of ice and snow, therefore the EM-Bird system always measures the total snow and ice thickness $z = z_i + z_s$. The System can measure at 10 Hz resolution. With a typical flight speed during low altitude operation of 120 knots, this correspondents to a point spacing of approximately 6 m. The laser altimeter itself measures at 100 Hz resolution but it's data is not processed and stored separately. Haas et al. [2009] demonstrated a good agreement within ±10 cm between EM-Bird derived sea-ice thickness and drill-hole measurements. Nevertheless, the system is likely to underestimate very thick ridges and structures with horizontal dimensions below the spacing between sampling points. The footprint of the EM-Bird system is about 40 to 50 m in diameter at common operational altitudes. For more information on technical details, the retrieval algorithm and validation see the paper of Haas et al. [2009] and references therein.

4.5 Measured variability of Arctic sea-ice albedo

The focus of this evaluation of measurement data is to study the variability in the albedo signal from representative examples. There will be two flight legs discussed in this section, which have been chosen out of 16 data sets from PAMARCMiP'09 and 19 from PAMARCMiP'11 for the availability of data from pyranometers, EM-Bird and photocamera. Few flight legs showed overlapping time series from these three instrument groups with a number of theses data records being affected with data gaps. Few but representative examples satisfy the goals of this particular study. The sequences from the two flights discussed below are from very different ice regimes, including thick consolidated multi-year ice north of Ellesmere Island, Canada, and broken first- and multi-year ice with refrozen leads in the Fram Strait.

All flights were operated during fair weather with clear sky conditions. Single cloud events were removed from the data. The two sequences of the flights presented below are free of clouds. The surface temperature and vertical temperature profiles (not shown) were measured with the KT-19 sensor and dropsondes, respectively. The data reveal that temperatures at and near the surface were well below the melting point ($< -20°$C) whenever measurements were taken above the sea ice. The KT-19 measurements were only available at 30 s resolution, thus leads could not be detected from this data set and therefore the surface temperature is not evaluated in more detail.

Flight 14.04.2011, Alert

On 14.04.2011 Polar 5 started from Alert and headed for a north-easterly course. The section of the flight leg used in the evaluation is marked as red line in a map of the area with Alert on the northern coast line of Ellesmere Island (Figure 4.14). Also information on monthly mean sea-ice concentration is provided as a layer in the map. This spatial information from an SSMIS instrument is provided by the OSISAF. Mean sea-ice concentration is mostly close to 100%. The route of this flight leg was chosen in a way that it covers a section parallel to the track of an overpass of the Cryo-Sat II satellite on the same day. These two datasets will be discussed together in Section 5.1.

The processed and filtered time series of albedo and total ice plus snow thickness is displayed in Figure 4.15. Because the EM-bird measurements made it necessary to go to higher altitudes for recalibration of the EM signal, gaps are found where higher flight segments were excluded from the data. For each flight segment the albedo values (blue curve) have been averaged with mean values indicated as a dashed line and standard deviations as a blue shaded area around the mean. The first two segments show strong variations with amplitudes of about 0.03 around a mean of 0.82 and 0.83 respectively. A slightly higher mean value of 0.84 was observed during the third segment together with less variation, whereas a lower mean value of 0.81 is observed for the last segment. In this last segment, the signal does not show the same pattern of increases and decreases, but drops in two instances to an albedo of 0.79 and 0.77.

The sea-ice thickness (green curve) has been averaged over 3 s ($\approx$150 m) and the respective standard deviation is shown as a grey shaded area around the mean. Thicker ice is observed during the
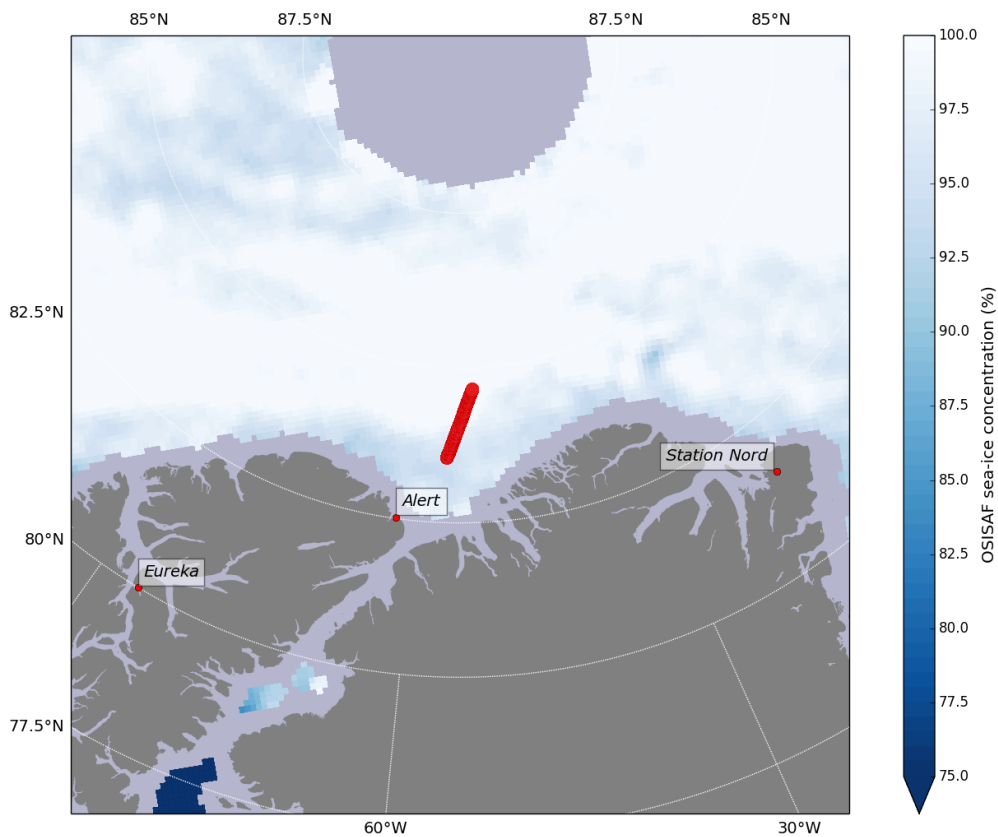
Figure 4.14: This map shows the flight track for the flight on 14.04 of PAMARCMiP'11 as a
red line. Polar 5 started and landed in Alert. Sea-ice concentration from an OSISAF product
for this day indicates mostly consolidated sea ice north of Ellesmere Island and Greenland.

first two segments with means around 5 m. Spikes with values twice as high as the mean value
occur frequently during these segments indicating areas where the sea ice formed ridges. The most
pronounced ridges with a measured thickness of over 20 m can be found around 15:38 UTC. A
photo of the ice at this position (Figure 4.16a) shows heavy deformation of the surface. The surface
topography is much rougher where sea-ice dynamics forced ice floes to collide and slide on top of
others, compared to rather undisturbed ice with a thick snow cover as in the photograph shown in
Figure 4.16b. This image is representative for normal surface conditions during this flight leg. The
average thickness of snow on sea ice in the Western Arctic is about 30 cm and a thickness of 20 to
40 cm is realistic for one season of snow accumulation on the ice (Section 3.2). Less snow is found
on new ice and ridges favour snow accumulation in their vicinity. Figure 4.16a and b show wind
beaten snow surfaces of probably above average thickness.

Very thin ice appears in two instances during the fourth segment of the measurement flight, coinci-
dently with the drops in albedo around 16:12 and 16:14 UTC. This events have been marked with
green vertical lines in the graph. The automatic evaluation of the photographs reveals a broken
snow cover (red vertical line) for the second event of thin ice. A photograph of this area is provided
in Figure 4.16c showing multiply broken up ice floes with refrozen leads covered by greyish grease
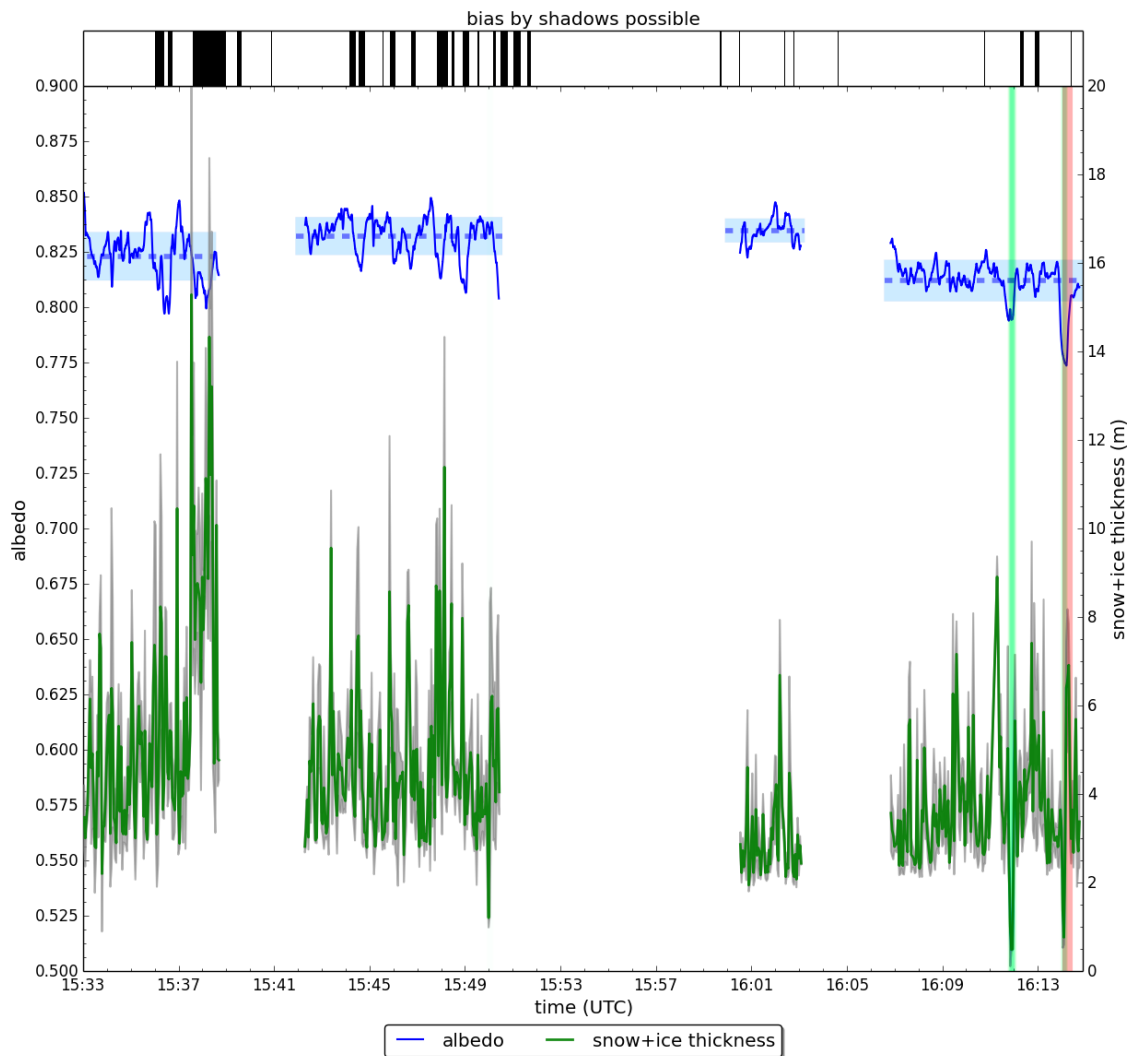
Figure 4.15: Evaluation of the broadband albedo and sea-ice thickness along the northward flight leg from 14.04 of PAMARCMiP'11. Gaps in the data are mostly a result of ascends to higher altitudes. Black bars at the top of the figure indicate events significant influence of shadows on the sea ice. Vertical bars in light green indicate events of thin ice and vertical bars in light red indicate events when ice or open water covered a significant share of the area seen in the photographs of the sea ice surface.

ice. The snow cover, where present, is thinner and an estimate of the area covered with darker new ice can hardly be given for this complex ice situation. However, it can be assumed that within the footprint of the bottom pyranometer (compare Figure 4.12) multiple surface types were present and therefore the measured albedo drops to a value representative for a mixture of snow and greyish ice.

The black bars in the top section of Figure 4.15 indicate sequences where a high areal coverage of shadows has been identified from photographs (Section 4.3). They coincide with dropping albedo signal and peaks in sea-ice thickness. The albedo signal shows a sinusoidal behaviour in the vicinity

Figure 4.16: Photographs of the sea-ice surface captured on the flight leg of 14.04.2011. Image a) was taken at 15:34:40 UTC and shows heavily deformed sea ice; image b) was taken at 16:11:48 UTC and shows sea ice with a relatively smooth and thick snow cover; image c) was taken at 16:14:12 UTC and shows leads refrozen with darker and lighter greyish nilas and snow covered thicker ice floes. The round red obstacle is an instrument gondola and the dark line in the middle is the towing cable of the EM-Bird.

of shadowed areas. Due to this sinusoidal behaviour, albedo values of the complete flight leg show a bimodal distribution (Figure 4.17) around a mean of 0.824 ± 0.013. The albedo distribution is tailed towards lower values. The distribution of the total snow and ice thickness exhibits a skewed distribution that is tailed towards thicker ice. Most of the sea ice during this flight leg was 2 to 6 m thick (mean value 4.40 ± 2.20 m) but also thinner ice was observed.
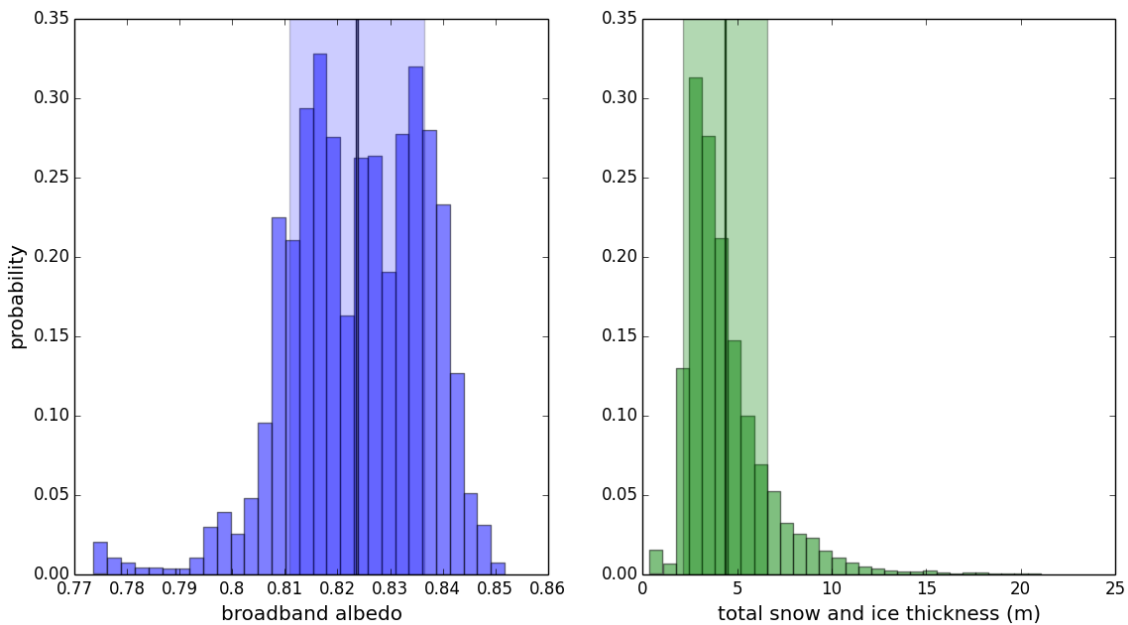
Figure 4.17: On the left in blue is shown a histogram of the broadband albedo values along the whole flight track from 14.04. of PAMARCMiP'11 and on the right in green a histogram of the sea-ice thickness for the same track. A dark vertical line indicates the median of each distribution and a shaded are indicates the range of one standard deviation.

Flight 05.04.2009, Longyearbyen
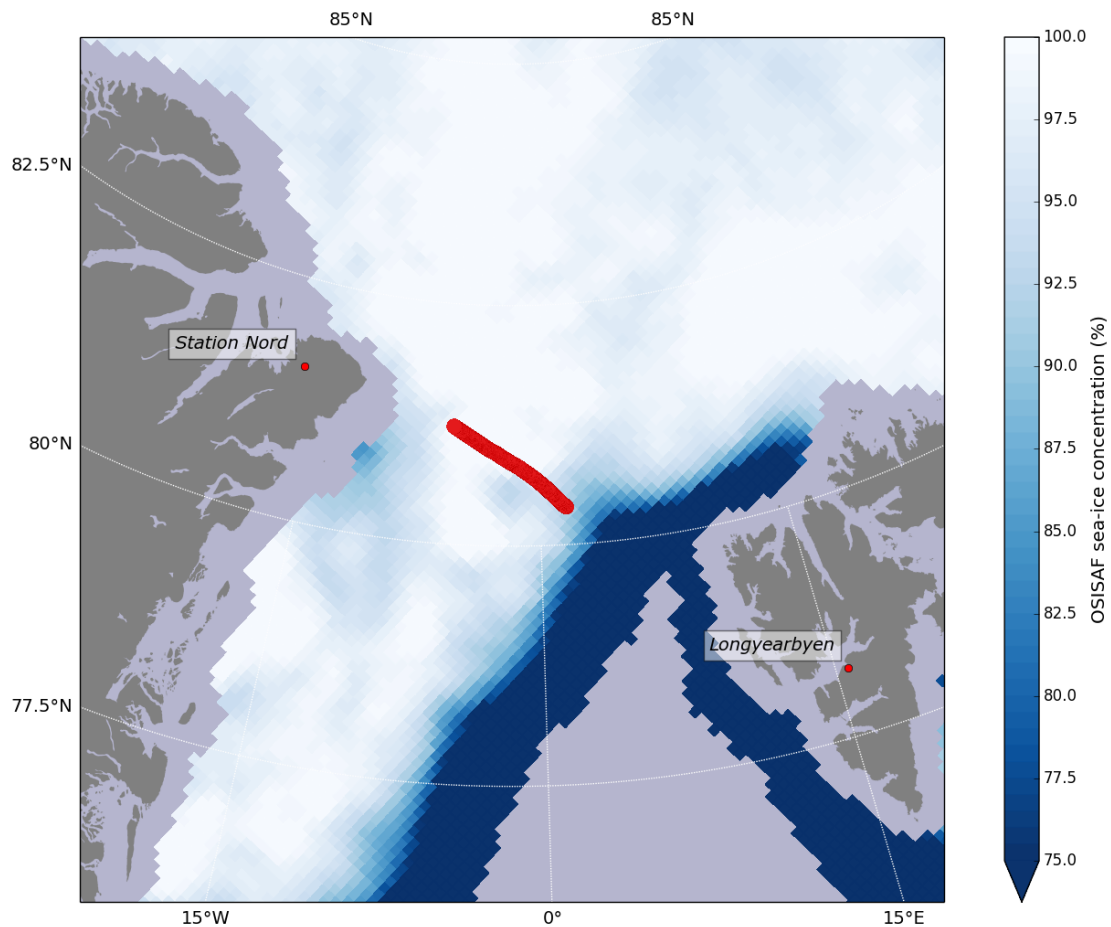
Figure 4.18: This map shows the flight track for the flight on 05.04 of PAMARCMiP'09 as a red line. Polar 5 started and landed in Longyearbyen. Sea-ice concentration from an OSISAF product for this day indicates broken ice in the middle of the Fram Strait and more consolidated ice closer the the east coast of Greenland.

The sea-ice survey on 05.04.2009 started from Longyearbyen on the Svalbard archipelago to cross the Fram Strait in a north-west direction towards the north-eastern tip of Greenland and returning to Longyearbyen at a higher altitude (Figure 4.18). Mean sea-ice concentration shows mixed conditions for this flight leg. Due to the prevailing winds and ocean currents, the Fram Strait is an outlet of the Arctic ocean, see also Figure 2.1. Thick ice from the multi-year ice region of the western Arctic drifts southward through the strait. Converging and diverging motions generate divers ice conditions in this area as pressure ridges, as well as wide leads and new ice will form.

According to these expected sea-ice conditions, the albedo measured in the Fram Strait shows diverse behaviour (Figure 4.19). The variability is large and values ranges from 0.36 to 0.94. This is especially applicable to the first two segments of the flight leg, while the third segment only shows minor variation with a standard deviation of 0.01 for a mean of 0.90. Again, the time series
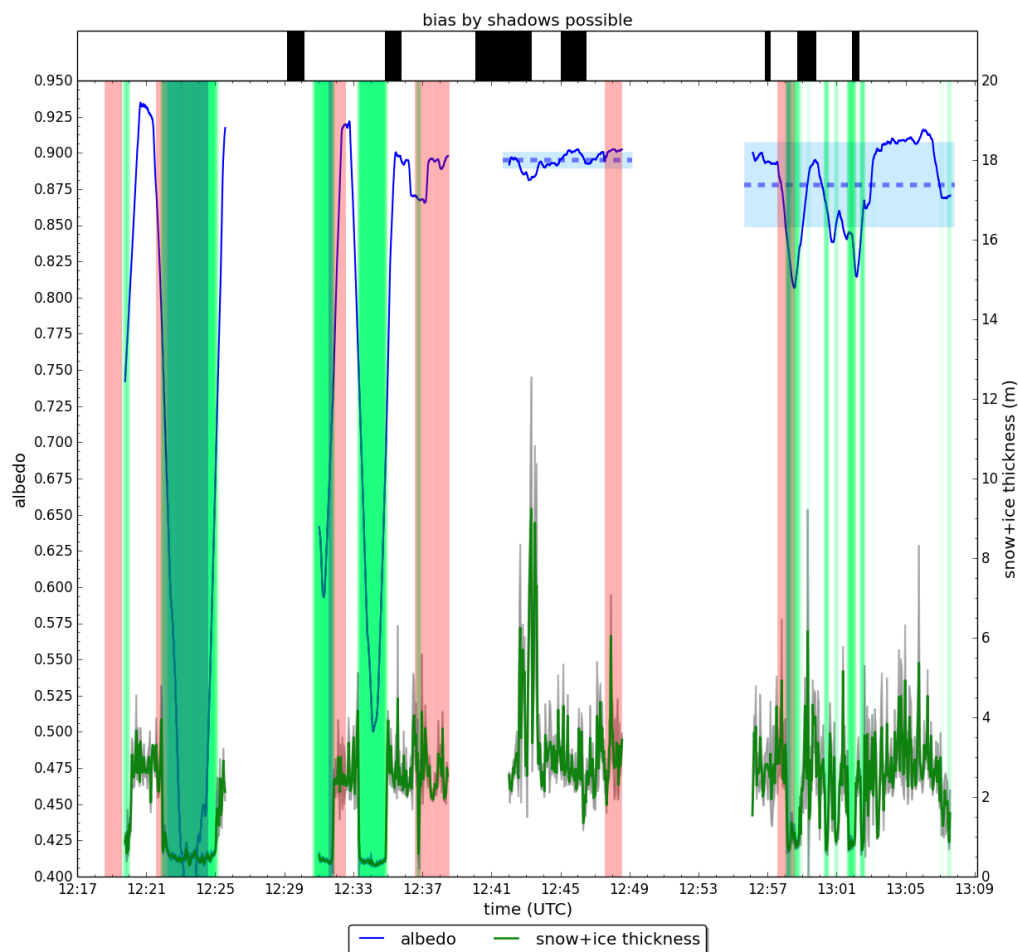
Figure 4.19: Evaluation of the broadband albedo and sea-ice thickness along the north-west flight leg from 05.04 of PAMARCMiP'09. Black bars at the top of the figure indicate events significant influence of shadows on the sea ice. Vertical bars in light green indicate events of thin ice and vertical bars in light red indicate events when ice or open water covered a significant share of the area seen in the photographs of the sea ice surface.

has gaps where the aeroplane was flying above 120 m. During every sequence, except the third, sea ice thinner than 1 m was detected (green vertical lines). In contrast to the sea-ice conditions observed near Alert on 14.04.2011 (discussed above), much wider refrozen leads are observed during this flight. The two consecutive photographs (Figure 4.20a and b) were taken at 12:23 and 12:24 UTC showing entirely bare ice and some open water. The footprint of the bottom pyranometer seems to be covered to a high degree with darker ice and water, rather than light snow. Hence, the measured albedo drops to values below 0.5. This lead stretches over a distance of approximately 9 km along the flight track. The extend across the track is unknown. Since the footprint of the measurement is about 700 m in diameter at an altitude of 90 m above the ice (Figure 4.12), it could be possible to estimate the albedo of bare ice from this segment. However, the photographs that are only available at a temporal resolution of 1 minute do not allow to characterize the surface properly in order to select a homogeneous part of the flight leg. Also the accuracy of the automatic

Figure 4.20: Photographs of the sea-ice surface captured on the flight leg of 05.04.2009. Image a) and b) were taken at 12:23:23 UTC and 12:24:23 UTC, respectively, and show parts of a large lead or polynya that is only partly refrozen with thin new ice without a snow cover. Whereas image a) shows a heterogeneous surface with areas of open water and also some thicker ice floes, image b), taken further west, shows rather homogeneous grey nilas with some rafting. Image c) was taken at 12:45:23 UTC and shows a closed thick snow cover with some wind erosion. The dark line in the middle is the towing cable of the EM-Bird.

evaluation of photographs suffers from the lower temporal resolution, compared to the campaign in 2011. The red vertical lines, indicating areas not fully covered with snow, were plotted wider for the sake of visibility but they are not representative for the timespan respective to their width on the time axis.

The fourth segment of this flight leg shows the same behaviour as discussed above for the flight leg from 2011. Small leads will cause the albedo to drop as the measured albedo is a result of a mixture of snow and ice of different thickness. The average over this segment gives a mean albedo of 0.88 ± 0.03, thus reaching values of more than 0.91. The overall distribution of sea ice thickness (Figure 4.21, right) shows a bimodal distribution. Thin ice was observed often, the mean thickness was $2.3 \pm 1.5\,\mathrm{m}$ and and the distribution is not tailing to higher values as much as for the multi-year ice observed near Alert.

Compared to the flight leg from 2011 (Figure 4.17, left), the maximum albedo values (Figure 4.21, left) are more than 8% higher and the mean value is more than 7% higher that observed in 2011. Even an undisturbed snow cover on sea ice, as found during flight segment three (see photograph in Fig 4.20c for 12:44 UTC), looking very similar to the conditions observed for most of the flight leg from 2011, reveals significantly higher albedo values. The differences cannot be explained by a significantly higher SZA in 2009 since for both measurement flights the SZA was $75° \pm 0.5°$. According to the evaluation of simulations with SoSIM in Section 3.3, broadband albedo values above 0.9 do not appear at this SZA for any realistic snow grain size. It is therefore likely that these measurements are erroneous. Comparably high values can also be found for other flight legs of the campaign PAMARCMiP'09. The uncertainty in the built-in offset correction due to the missing radiation box pattern (see Section 4.2.3) is an error that might explain this discrepancy in the order of 5 to 10%. Nevertheless, this flight leg gives valuable information on the variability of the albedo for highly heterogeneous surface conditions. Absolute values are most likely wrong and must not be used for conclusions concerning annual or regional variability.
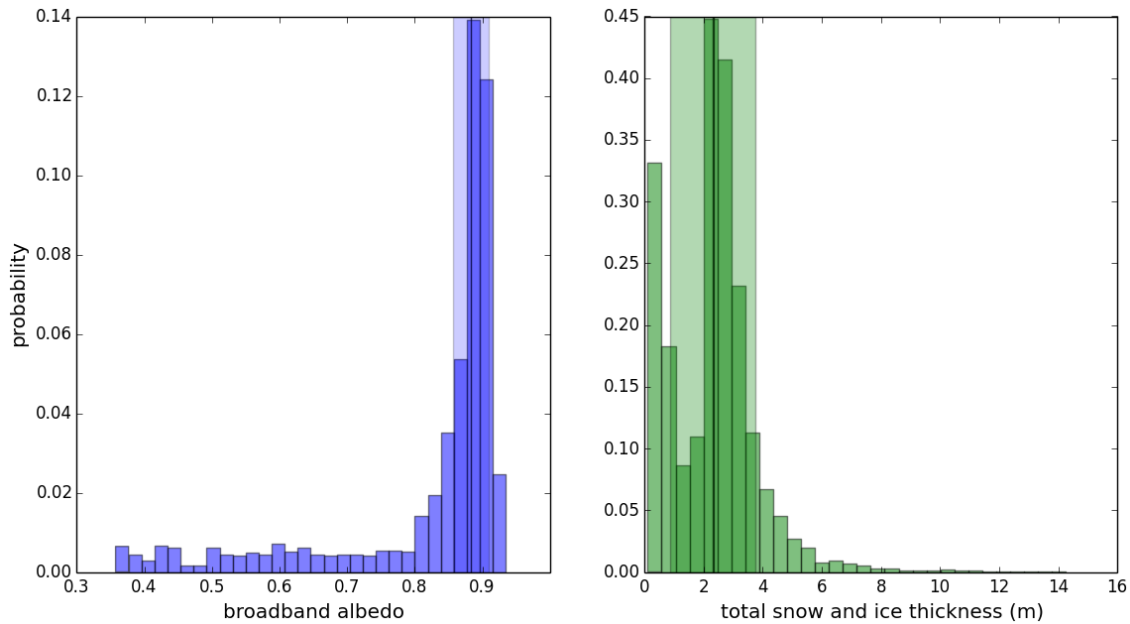
Figure 4.21: On the left in blue is shown a histogram of the broadband albedo values along
the whole flight track from 05.04. of PAMARCMiP'09 and on the right in green a histogram
of the sea-ice thickness for the same track. A dark vertical line indicates the median of each
distribution and a shaded are indicates the range of one standard deviation.

4.6   Conclusions

The accuracy of the measurements has been evaluated. Due to the individual measurement
uncertainties of the upward and downward irradiance, the albedo calculated from these measurements
has a relative uncertainty composed of several contributors. Because the measurements were
performed at relatively high SZAs (about 75°) compared to the calibration process (about 30° to
50°), a higher instrument uncertainty than stated on the calibration certificate is assumed for the
pyranometer affected by direct solar irradiance. The relative uncertainty of the obtained albedo
values could be quantified to at least 4.1%. Due to the uncertainly known built-in offset for the
campaign in 2009, an extra uncertainty of 7.0% applies for this campaign. These uncertainties are
large compared to the expected variability of the broadband albedo induced from changes in snow
grain size (in the order of 10%) and BC content in the snow (in the order of 1%) (Section 3.3).

It is known that airborne albedo measurements are influenced by the backscatter radiation of the
atmosphere below flight altitude [Wendisch et al., 2004]. Simulations with SoSIM revealed that the
measured albedo over a highly reflective snow surface will decrease non-linearly with altitude of the
sensor above ground level. The non-linear trend depends on vertical profiles of scattering gases
and aerosols [Wendisch et al., 2004]. For the relatively low operational flight altitude during the
measurements (90 m), the expected underestimation of the surface albedo is low ($-0.5 \pm 0.5\%$).
The small variations of the flight altitude of about ± 20 m have minor impact. A correction of
the measurements by model calculations is possible but might introduce new uncertainties due to

unknown atmospheric state. Hence, no correction is suggested for measurements at low altitudes.

During the measurement flight on 14.04.2011 near the cost of Ellesmere Island, the mean broadband albedo ranged between 0.82 and 0.84. The SZA during this measurement sequence was between 74.5° at the beginning and 75.5° to the end. The albedo observed during the flight legs shows strong variations with an amplitude of about 0.03 at a wavelength of kilometre scale. This variation seems to be induced by the topography of the sea ice. It coincides with areas where shadows were detected. Sequences of smoother ice revealed less variation. The large spatial scale of this variation and the fact that it has both, a positive and negative bias compared to the mean albedo signal, indicates that not single ridges influence the signal. The reflectance of a surface with rough topography can have a strong angular dependence [Warren et al., 1998]. The pyranometer seems to be positively biased by the irradiance reflected at the flanks of ridges in the distance. Ridges cause a negative bias when the instrument is looking into shadowed areas from directly overhead. The albedo drops coincidently with the detection of shadows from photographs. Since the viewing geometry of the instrument is very different to the low angle of the sun above the horizon, the measurements do not represent the real shortwave energy balance of the surface. Despite the angular dependence of the reflectance, most of the energy is redistributed into the upper hemisphere [Warren et al., 1998]. Pyranometer measurements cannot give a unbiased estimate of the instantaneous surface energy balance, but the effects of surface roughness are considerably attenuated by the spatial average over the whole footprint of the instrument [Gallet et al., 2011] and by averaging over longer time intervals. Mean values are therefore considered as representative for the area, the line measurements were performed in. Still, by selecting a certain route through the area, that features only parts of the present surface types, the mean values may be biased. Over the whole flight leg of about 140 km, mean values of both rough and smooth segments varied between 0.81 and 0.84. An albedo variation on a larger spatial scale seems also to be present, which might be caused by changes in snow conditions.

Albedo data from PAMARCMiP'09 cannot be evaluated in terms of absolute values because of a systematic error that causes values about 7 to 8% too high. A false correction of the built-in offset might explain most of this error. Nevertheless, the flight leg from 05.04.2009 demonstrates the influence of differently scaled surface inhomogeneities. Leads (covered with new ice or open water) cause a drop of the albedo signal. The minimum depends on the size of the lead and on the fraction of open water. Shadows and reflections due to ridges cause a sinusoidal behaviour of the measured albedo signal. Albedo measurements with a hemispheric receiver have a large footprint, especially in the case of airborne measurements (Figure 4.12). The resulting albedo measurement is a folding of the spatial distribution of different surface types and the signal-weighting of the sensor (see discussions above), thence the albedo is averaged over a certain area. Measurements from both flight legs showed that the heterogeneity of the surface has the strongest influence on the albedo. For the albedo measurements at the sites in the Beaufort Sea and Fram Strait, sea-ice dynamics caused for most of the strong and high frequent variation of the measured albedo. No flight leg revealed a possibility to quantify the albedo of snow free sea ice with measurement undisturbed of other surface types.

Following the conclusions of Chapter 3, the microphysical properties of the snow define the mean sea-ice albedo of an undisturbed spatial average. In order to see if SoSIM can reproduce the mean albedo of such an undisturbed snow cover on sea ice as observed during the flight on 14.04.2011, a model study is conducted. Table 4.2 lists a range of parameters that were used as model input and the resulting broadband albedo. None of these parameters were measured directly, nor could they be derived from broadband albedo measurements. The latter is not possible because of the high relative measurement uncertainty and high superimposed variability of about 3.5%, compared to the low expected albedo changes. Thus, the input parameters are not certainly known. The SZA during the flight was $75 \pm 1°$ and the data is filtered for clear sky conditions only. The AOD $\tau_{\mathrm{aerosol}} = 0.3$ corresponds to the mean AOD observed during this flight. The evaluation of the photographs inferred that a thick snow cover was present in the area (except for the two refrozen leads). Hence, for all calculations, $z_{\mathrm{snow}} = 40\,\mathrm{cm}$ was chosen to represent a optical semi-infinite snow cover and to be in good agreement with the average snow thickness in the area reported in the climatology of Warren et al. [1999]. It was assumed that the snow cover consisted of aged snow crystals, about 1 to 3 weeks old, with $100\,\mu\mathrm{m} \leq r_{\mathrm{eff}} \leq 200\,\mu\mathrm{m}$. Also the presence of BC in the snow could have been possible. The concentrations in this analysis, as listed in table 4.2, account for no, normal and very high concentrations of BC. The broadband albedo measurements from the flight leg near Alert, averaged over a longer time sequences reveal values between 0.81 to 0.84. The re-simulation of the situation with SoSIM show fairly good agreement. Although no exact input parameters are known, the assumed range of parameters yields model results in the observed albedo range. It can thus be concluded that SoSIM may reproduce the mean albedo values observed during the flight leg from 14.04.2011. Values as high as widely measured during the campaign in 2009 could not be reproduced by SoSIM for the prevailing clear sky conditions except for an unrealistic setup (very low sun and very small snow grains).

Table 4.2: Model parameters for a re-simulation of the measurement conditions during the flight on 14.4.2011 near Alert.

r_{eff} µm	C_{BC} ng/g	z_{snow} cm	SZA degree	broadband albedo
100	0	40	75	0.8443
100	10	40	75	0.8425
100	20	40	75	0.8409
125	0	40	75	0.8343
125	10	40	75	0.8322
125	20	40	75	0.8304
150	0	40	75	0.8258
150	10	40	75	0.8235
200	0	40	75	0.8119

4.7   Possible improvements for the measurement setup

Photographs   of the surface have proven to be a valuable source of information on surface conditions. Due to the many parameters able to alter the albedo significantly even for a homogeneous surface (see Section 3.3), albedo measurements should rather not be interpreted if the surface conditions within the footprint of the sensor are unclear. Taking photographs with a temporal resolution of 1 Hz would result in an overlap of the pictures and no information is lost along the flight track, given the average speed over ground of 50 m/s and an altitude of 90 m AGL. The $f = 14$ mm wide angle lens delivers distortion free images, a *fish-eye* lens would improve the areal coverage of the photographs and would have similar viewing characteristics as the pyranometer.

Furthermore, imaging of the sky would be an advance since clouds could be detected. Knowledge about cloud conditions would ease the post-processing of the radiation measurements and would possibly increase the availability of the data for cases of uncertain sky conditions. Logging of cloud events during the campaign could be automated with cloud detection algorithms. Amongst others, Heinle et al. [2010] propose a cloud detection algorithm working with photographs of the whole upper hemisphere captured with a fish-eye lens. There is also ongoing development at the IMuK (Institut für Meteorologie und Klimatologie, University of Hanover) for such a system.

Spectral albedo measurements   would significantly increase the amount of information that can be derived from the measurements because of the characteristic spectral behaviour of the snow-albedo. The parameter study with SoSIM in Section 3.3 demonstrated the distinct spectral characteristics of certain influences on the albedo. For example the effective snow grain radius could be inferred from the strong sensitivity of the spectral albedo between 1250 and 1350 nm (Picard et al. [2009] suggest 1310 nm) relative to the low sensitivity near 450 nm (compare Figure 3.4). Vice versa, BC affects the UV and VIS but not the NIR. In the broadband albedo measurements, these characteristics are smeared, such that single influences cannot be distinguished. SoSIM can be used to develop a retrieval algorithm following the work of Li et al. [2001]. Alternatively, Zege et al. [2011] utilise the model by Kokhanovsky and Zege [2004] for a retrieval of snow grain size and BC content from spectral albedo data.

For these measurements, different array-spectroradiometers could be used. Favoured would be instruments covering the VIS and NIR (400 to 1400 nm, with good signal-to-noise ratio). While wavelength accuracy is of secondary importance, temperature stability is a concern since the temperatures inside the cabin of the non-air-conditioned Basler BT-67 vary considerably. An extra climate box for the instrument should either not be necessary or optimized for weight because of the limited payload of the aeroplane. An alternative to array-spectrometers are multichannel filter instruments since for the purpose of snow grain size retrievals only few (at least two) wavelength bands are necessary. Used for such measurements could be a technique for the active stabilization of the entrance optics introduced by Wendisch et al. [2001]. Its advance is that no temporal and spatial resolution is lost due to correction algorithms for the flight attitude as described in Section 4.2.3.

Snow-thickness measurements   would either need a high resolution in the centimetre range in order to resolve thin snow below about 20 cm or the measurements could ensure that the snowpack is semi-infinitely thick. The latter could also be achieved by the visual control of photographs. Only with this information, retrieval calculations are feasible due to the non-linear reduction of the albedo with thinning snow (Figure 3.8).

5. Estimating the climate impact of a changing sea-ice albedo

The albedo of land and ocean surfaces, as well as clouds and aerosols, control how much solar energy is absorbed on earth and is available for heating the planet and driving the climate system. In the Arctic, snow and ice are the predominant surface cover governing the energy balance. Via the ice-albedo feedback, the state of the Arctic's cold climate is very vulnerable to perturbations in the energy household. Anthropogenic influences on the climate system of the Arctic have many facets. The IPCC (Intergovernmental Panel on Climate Change) Assessment Reports employ the term *radiative forcing* for an externally imposed perturbation in the radiative energy budget of the climate system [Ramaswamy et al., 2001]. Besides changes in surface albedo, also an altered solar irradiance incident upon the planet or the increasing concentrations of long-lived greenhouse gases like carbon dioxide or methane can cause such perturbations. This study will focus on perturbations of the surface albedo. A decreased albedo is a surface forcing to the radiative energy budget and causes an imbalance that has the potential to change climate parameters and lead to a new equilibrium state of the climate system [Ramaswamy et al., 2001]. A surface forcing by a changed albedo cannot be directly translated into a radiative forcing in the sense of the definition used in the IPCC Assessment Reports. It states that a radiative forcing is the change in net solar and longwave radiation at the tropopause after allowing stratospheric temperatures to readjust to a radiative equilibrium [Ramaswamy et al., 2001]. The estimation of the radiative forcing of a changed surface albedo therefore necessarily embodies modelling of all relevant aspects of the climate system, i. e. using a global circulation model (GCM).

In this chapter, a model will be developed, able to estimate the surface forcing by BC and other changes to the albedo of snow covered sea ice – especially focussing on regional differences of the forcing. The model has been formulated based on the findings of causes for the variability in sea-ice albedo from Chapters 3 and 4. This model is able to predict, e. g. re-analyse, the spatial distribution of the albedo for the entire Arctic sea-ice cover. The model is an approach to apply the albedo calculated with SoSIM to heterogeneous surfaces. This is realised by accounting for the variability of a spatially averaged sea-ice albedo using information on the mean state of sea-ice and snow cover from satellite observations and climatological maps. This model is an alternative to satellite products that calculate the albedo from measurements of reflected radiance [Xiong et al., 2002]. Besides estimating the spatial distribution of the sea-ice albedo in the Arctic, the model has the aim to quantify the

surface forcing due to snow parameters altering the albedo. The model approach will be described in 5.1 and used to calculate the surface forcing of a changed snow albedo on Arctic sea ice in Section 5.3.

After evaluating different effects causing the natural variability of the sea-ice albedo in the two previous chapters, this chapter will focus on the effects of BC. BC is in the sense of its origin both, an externally and anthropogenically imposed perturbation to the Arctic climate system. In contrast to greenhouse gases, BC aerosol is a short-lived climate forcer. It has only an atmospheric lifetime of several days to a few weeks since it is removed from the atmosphere by sedimentation and wet deposition. Thence, reducing BC emissions will result in a faster response of the climate system as changes to carbon dioxide emissions. The pathways of BC into the Arctic and possible effects on the local climate are discussed in Section 5.2.

5.1   Model of spatial sea-ice albedo variability

The results from the parameter study with SoSIM and the evaluation of the measurement campaign, Chapters 3 and 4, are the base for this model. The studies revealed that the snow microphysical parameters are responsible for the mean surface albedo, while the thickness and topography of the sea ice, caused by its divergent and convergent motions, are responsible for strong variations in the spatially averaged albedo. Therefore, a source of information on these parameters would enable a model to predict the average surface albedo of sea ice in a certain region. Such a model for spatial albedo variations in the Arctic is formulated and tested in this section. It is intended for spring conditions and uses the available information on snow thickness and sea-ice conditions while making reasonable assumptions for other snow parameters, atmospheric state and SZA.

The model is based on data from the CryoSat-2 sea-ice thickness data product released by the AWI. The product is available online[1] since June 2013 [Hendricks et al., 2013]. CryoSat-2 is in operation since late 2010 and sea-ice thickness measurements obtained during the PAMARCMiP campaigns are used for validations of the satellite derived data. The CryoSat-2 product provides sea-ice freeboard and thickness information retrieved with the SAR/Interferometric Radar Altimeter (SIRAL) payload of CryoSat-2. For the altimeter measurements, SIRAL utilises synthetic aperture processing to enhance the resolution along the satellite track (Figure 5.1) and reaches an operational footprint 250 m wide along track and an effective footprint across track of 1650 m [Rebhan et al., 2003]. Since additional information about the surface is needed in order to evaluate the radar echo, the satellite product also includes gridded information on snow depth and density as well as sea-ice concentration and type. Till this day, there is no source for reliable, Arctic wide spatial information on snow thickness and density. The climatology after Warren et al. [1999] is the only source that provides Arctic wide snow thickness and density based on in-situ measurements from soviet drift stations between 1954 and 1991. However, since multiyear ice is shrinking rapidly in recent times adjustments based on airborne snow radar data have been applied to the climatology
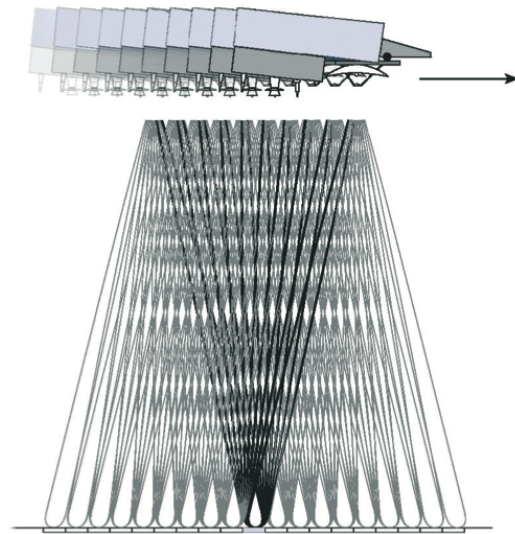
---

[1]http://www.meereisportal.de

Figure 5.1: Synthetic aperture processing enhances the resolution of the CryoSat-2 satellite along its track. The footprints over a flat surface are adjacent rectangular areas about 250 m wide along track and 1650 m across track; figure and specifications from Rebhan et al. [2003].

to accommodate these changes Kurtz and Farrell [2011]. The climatology provides monthly data but does not reflect interannual variabilities. Furthermore its spatial resolution is coarse and hence it is not featuring strong variations on a regional scale. The additional sea-ice information are taken from OSI SAF products, which are based on a multi-sensor approach, processing Special Sensor Microwave/Imager (SSM/I) and Advanced Scatterometer (ASCAT) data. Both instruments have a footprint of approximately 12.5 by $12.5\,\mathrm{km}^2$ [Eastwood, 2014]. All data of different spatial resolution are interpolated and gridded onto an EASE2.0 grid [Brodzik et al., 2012]. This grid is based on a polar aspect spherical Lambert azimuthal equal-area projection resulting in equal sized grid cells, in this case sized 25.0 by $25.0\,\mathrm{km}^2$.

The map of the monthly mean sea-ice thickness in the Arctic released with the CryoSat-2 product is processed from several along-track measurements. The number of revisits at a certain point depends on the orbital characteristics of CryoSat-2. During PAMARCMiP'11 on the 14.04.2011, Polar-5 flew in coincidence with a CryoSat-2 overpass over sea ice north-east of Alert. This track has been evaluated in detail in terms of the available data from the airborne measurements in Section 4.5. Data from the CroySat-2 track is plotted in Figure 5.2 in respect to the distance from the southern end of the parallel track measurements, as shown in Figure 4.14. This distance has been calculated from the succeeding latitude and longitude positions of the geo-referenced measurement values. Along this track, the snow depth from the climatology of Warren et al. [1999] shows only a minor increase from the south to the north, Figure 5.2a). The sea-ice appears to be thicker closer to the coast where the presence of ridges potentially increases the spatial average of the detected sea-ice thickness. CryoSat-2 detected several areas of very thin ice, i.e. refrozen leads, along the whole track with average thickness below 1 m, Figure 5.2b). Open leads are not detected by CryoSat-2. The sea-ice concentration, Figure 5.2c), has a minor increase from 95 to 100% towards the north, which might indicate that the areas of open leads in the sea ice become smaller. This observation is in contrast to the thinner sea-ice thickness observed towards the northern end of the measurement track of PAMARCMiP'11. This difference shows that is has to be kept in mind for the further
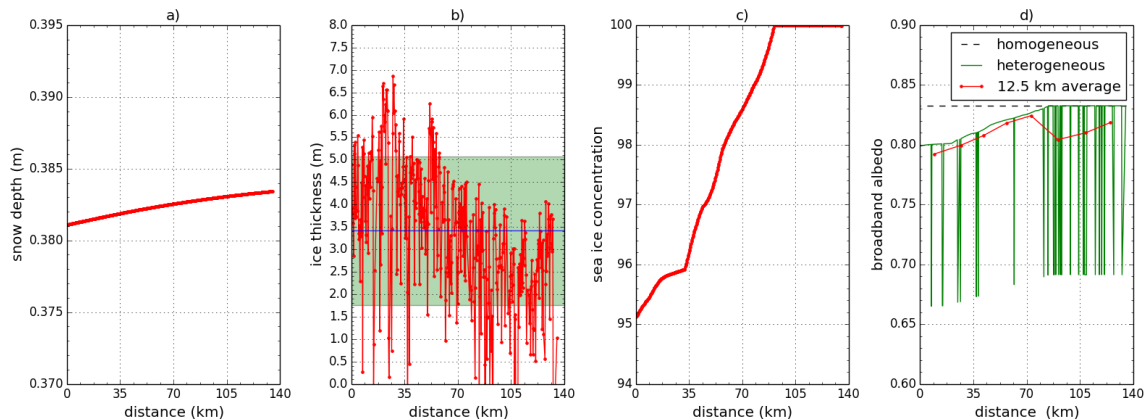
Figure 5.2: Data from the CryoSat-2 sea-ice thickness product plotted along the same track
as flown during PAMARCMiP'11 on 14.04.2011 north-east of Ellesmere Island (see the map
in Figure 4.14 and its description in Section 4.5). Data is plotted against the distance from
the southern end of the track. It is shown in a) snow depth; b) sea-ice thickness, with the
median thickness indicated as a blue line and an area of ± 1 standard deviation is shaded in
green; c) sea-ice concentration and d) the albedo calculated from the look-up-table obtained
with SoSIM (dashed line) according to the snow depth and a assumed density of the snow
pack of $320\,\mathrm{kg/m^2}$ and snow grain size of $r_{\mathrm{eff}} = 100\,\mu\mathrm{m}$, as well as a SZA of $75°$. Further,
an albedo altered due to the sea-ice conditions is plotted in d) with a green line and that
albedo averaged over $12.5\,\mathrm{km}$ of the line measurement with a red line.

interpretation that the sea-ice concentration is measured for a much larger footprint than the sea-ice
thickness observations.

The first approach to model a spatially averaged broadband surface albedo is done for sea-ice thick-
ness measurements along a satellite track for which parallel measurements from PAMARCMiP'11
on the 14.04.2011 exist. Airborne measurements of the sea-ice thickness and albedo of this track
north-east of Ellesmere Island (see the map in Figure 4.14) are described in Section 4.5. The model
can be tested and tuned with the data from PAMARCMiP'11. Therefore, the albedo is calculated
such that it matches to the conditions found during measurement flights in order to be able to
compare model results and measurements. In a second approach, the model can be applied to
gridded data on sea-ice information of the whole Arctic. For both approaches, the model calculates
an albedo in three steps, looking up the available information at each grid cell in the CryoSat-2
product:

1) Information on snow depth is used to chose an albedo from the look-up-table calculated with
   SoSIM that is described in Section 3. For all other parameters influencing the albedo, the
   following assumptions are made:

   - A snow grain size of $r_{\mathrm{eff}} = 100\,\mu\mathrm{m}$ is chosen to resemble medium aged snow (or a mix-
     ture of new snow and old snow within the footprint) following the assumption made
     by Hansen and Nazarenko [2004]. There is no source for information on snow grain size.

Although the albedo shows strong variation with r_{eff}, the chosen radius can be justified for a temporal and spatial average of the snow conditions because snow metamorphism equalises snow grains. A potentially higher or lower local grain size must be discussed as an uncertainty of the modelled albedo.

- The density of the snow pack is $320\,\text{kg/m}^2$, which is in good agreement with the mean snow density from the snow climatology of Warren et al. [1999] in the Western Arctic and for April. Small density variations have negligible impact on the albedo.

- A SZA of 75° is used to match the conditions during the measurement flight. For better comparability of the calculated albedo, the SZA is not altered with latitude. Also satellite derived surface albedo products normalize the albedo to one specific SZA.

- The albedo is calculated for clear sky conditions and an AOD of 0.3, as observed on average during PAMARCMiP'11. This reflects a certain ratio of direct to diffuse incident radiation at the surface.

2) If thin ice $z_{\text{ice}} < 100\,\text{cm}$ is detected within a grid cell, this is evaluated as the presence of a refrozen lead without snow accumulation. The resulting albedo within this grid cell is a mixture of 50% ice and 50% snow. The broadband albedo of a refrozen lead is assumed to be 0.6 [Perovich et al., 1998].

3) Sea-ice concentration within the grid cell is used to mix the albedo of snow covered ice and the albedo of open water areas (assumed to be 0.06 [Perovich et al., 1998]).

An estimate of the spatially averaged albedo along the track is calculated in step 1) according to the snow conditions. It is plotted in Figure 5.2d) as a dashed black line and is fairly constant over the whole distance since the snow thickness according to the climatology only changes by a few millimetres. The albedo altered through steps 2) and 3) is plotted as a green line and as a red line, the latter representing an average over 12.5 km of the track. The albedo of the undisturbed surface is 0.83 while the albedo with respect to the surface inhomogeneities has a lower median albedo of 0.82. This value can be compared to the observations from the airborne measurement campaign presented in Section 4.5. There, a median value of the measurement sequences between 0.82 and 0.84 was observed, thus the modelled albedo lays at the lower end of this range.

The measured and modelled albedo show qualitative differences. There is a different trend along the track and the model result shows a large number of local minima which cannot be found in the measurements, where the albedo only considerably dropped below 0.8 during two overpasses of refrozen leads. The different trend might be an issue of the different footprints. The strongest mode of the albedo variation is introduced by the sea-ice concentration, which is measured by an instrument with a much larger footprint, thus the satellite observation not necessarily resembles the conditions observed at the flight path taken during PAMARCMiP'11. The different variability might have two main reasons. On the one hand, the pyranometer measurements involve temporal and spatial averaging, therefore they are not able to resolve albedo changes on the same scale on which the SIRAL measures sea-ice thickness changes. On the other hand, it has to be taken into account that there are several gaps in the airborne measurement data because the aircraft had to change to a higher flight altitude. Some of these data gaps coincide with leads, hence the full
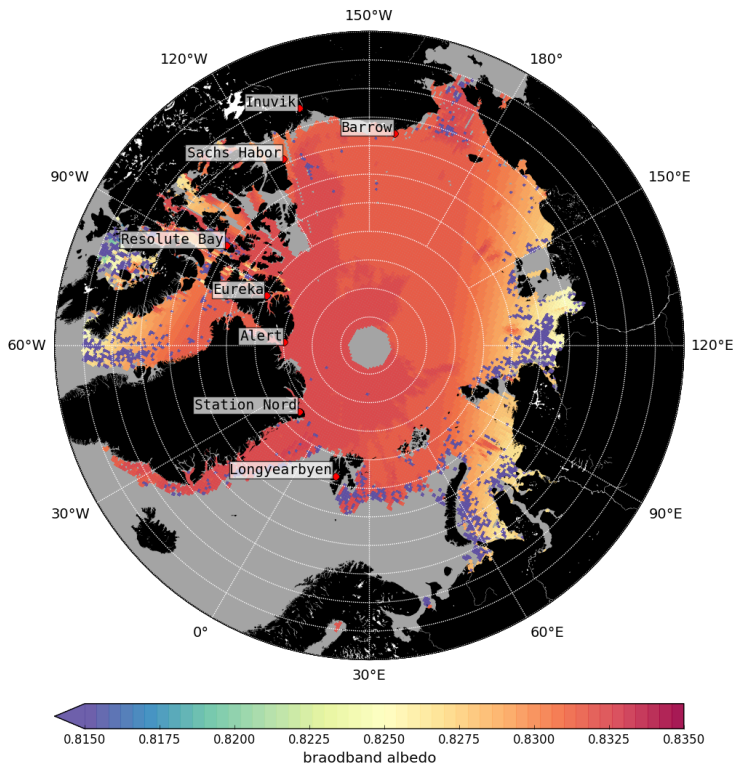
Figure 5.3: Intermediate result after applying steps 1) and 2) to the gridded snow and sea-ice information. This map represents the sea-ice albedo distribution due to snow depth variation and detection of thin ice only. Variation of the albedo due to thin ice applies to few grid cells visible as points with very low albedos.

variability of the albedo cannot be estimated from these airborne measurements. Therefore it has to be concluded that this model is not able to produce spatially averaged albedo values representative for the small scale of the SIRAL instrument's footprint, i.e. about 0.25 by 1.65 km^2. The goal of the model based on this sea-ice data can only be to introduce a variability, e.g. a reduction, to the albedo of a homogeneous snow cover in a way that the albedo averaged over a greater area has a lower value that accounts for the heterogeneity of the surface in this area. This scale cannot be lower than the 12.5 by 12.5 km^2 resolution of the sea-ice concentration data. For an average over a greater area, it can be concluded that this model produces spatially averaged albedo values in a realistic, reasonable, range. A comparison to other data averaged over a different area is not trivial.

By applying the model approach described above to the gridded data sets of the CryoSat-2 sea-ice thickness product, an albedo map for the entire Arctic sea-ice cover can computed. An intermediate result of the albedo distribution after applying only steps 1) and 2) is shown in Figure 5.3. The map of the full result (Figure 5.4) resembles the surface albedo for the mean sea-ice conditions in April 2011.

When comparing the full result (Figure 5.4) to the intermediate result (Figure 5.3), it becomes evident that the sea-ice concentration has the largest influence on the albedo of each grid cell. Figure 5.3 shows a minor variation of the albedo due to snow thickness. This variation follows the snow thickness climatology by Warren et al. [1999]. The snow thickness distribution has been altered to account for the fact that there is more snow on multi-year ice than on the seasonal ice cover. Hence, there is a difference of about 0.01 in the surface albedo between the two ice regimes
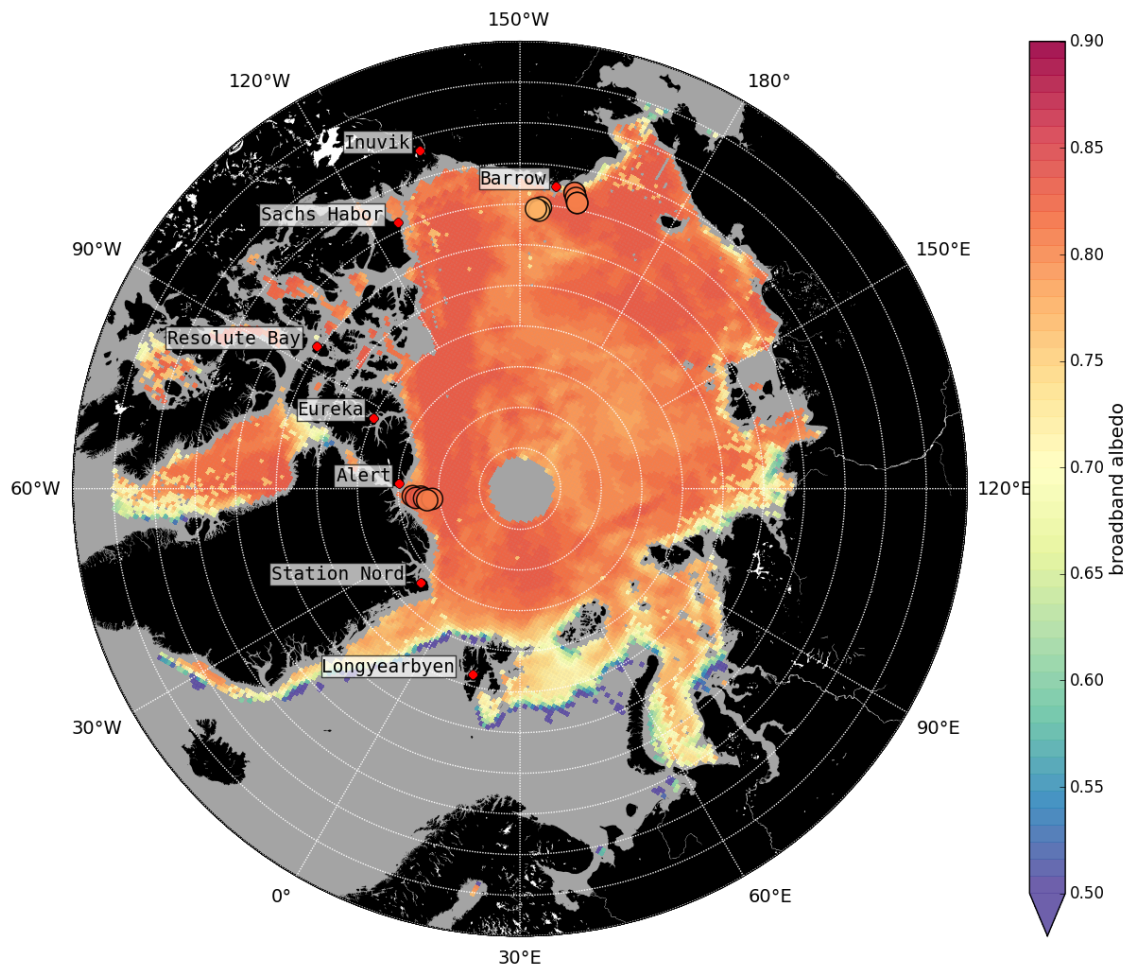
Figure 5.4: Map of the modelled sea-ice albedo in the Arctic for monthly mean sea-ice and snow conditions of April 2011. The circles near Alert and Barrow stand for averaged line measurements from PAMARMiP'11.

(compare with the map in Figure 2.1). The detection of thin ice in step 2) has only modified the surface albedo of a few grid cells – found as albedo values below 0.8 in Figure 5.3. Leads and thin ice seem to be smoothed by the spatial and temporal average.

The circles in Figure 5.4 represent three measurement flights from PAMARCMiP'11, and match the color scale on the right. The data from these line measurements has been averaged over segments of 18 km to represent the average albedo along the track. The flight leg near Alert from 14.04.2011 has been analysed and discussed in Section 4.5. The legs near Barrow from 01.04 and 02.04. are not presented in detail in this study, since the availability of the additional data, e. g. photographs and EM-Bird measurements, is rather sparse. Nevertheless, the albedo data has been processed and filtered in the same way as that from Alert. The respective grid cell for the center position of the flight segment, over which the flight leg has been averaged, was looked up from the gridded data with the help of a search algorithm. This way, one model and one measurement value can be compared in order to use those three flight legs as a validation of the model.
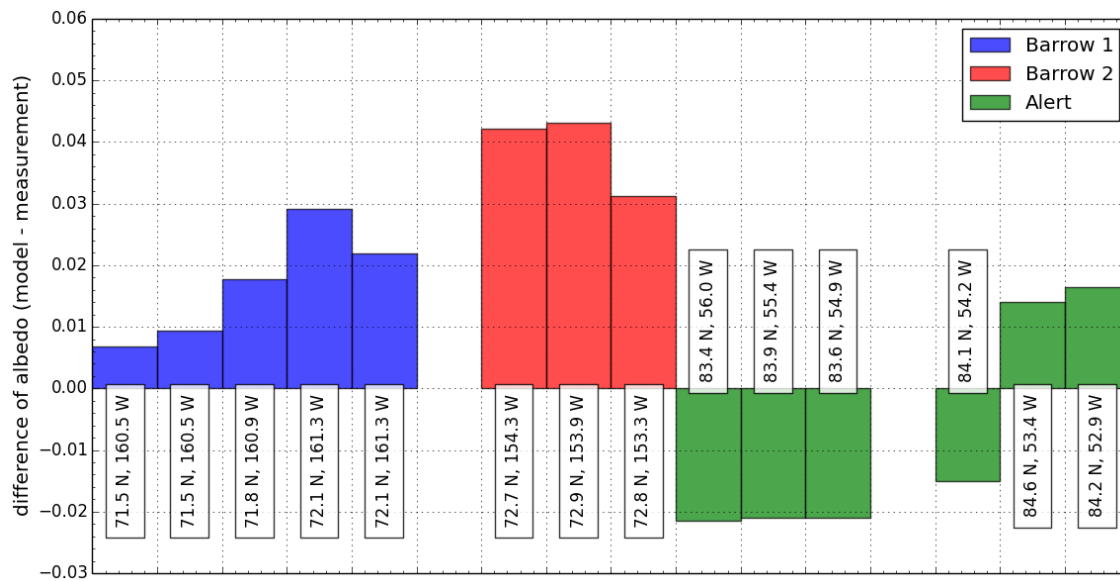
Figure 5.5: Difference between model results and measurements. Measurement values are averaged over segments of the flight legs from 01.04. (Barrow 1), 02.04 (Barrow 2) and 14.04. (Alert) of the campaign PAMARCMiP'11. Model values are taken from the respective grid cell matching the coordinate of the middle of the flight segment. No bars are shown where only few data points were available for the average.

The difference between model and measurement values for each point is shown in the bar diagram (Figure 5.5). For the westerly flight leg near Barrow (*Barrow 1*), the model seems to predict higher albedos. The difference between modelled and measured albedo increases with increasing distance from the coast. Generally lower albedo values are found in the region of the easterly flight leg (*Barrow 2*). This is shown by both, model predictions and observations, but the model predicts a higher albedo than actually observed. The evaluation of photographs (not shown) reveals a very thin snow cover on the ice in this particular area. Probably new consolidated ice was present at the time of the measurement flight. The sea-ice concentration within this area is lower, indicating divergent motions of the ice and formation of new ice, which initially is not covered with snow. This thinner snow cover is in contrast to the input values for the model from the climatology. Thence, the instantaneous observations differ from the model calculations for the assumed average snow conditions. Other than for seasonal ice, for the multi-year ice area near Alert, the model shows lower and higher values than observed during the campaign. The model predictions, mostly influenced by the sea-ice concentration, show an opposing trend when compared to the albedo measurements in Figure 4.15. The sea-ice thickness from EM-Bird measurements and the instantaneous CryoSat-2 measurements on the track (Figure 5.2) also would rather infer a different behaviour of the sea-ice concentration.

This comparison showed the limitations of the model due to the uncertainly known input parameters and the problems involved in validating satellite data with instantaneous data sets with much smaller footprint. The difference along the track near Alert is in the range of ±2.5%. If data would be available averaged over comparable temporal and spatial scales, the deviation would potentially

be lower. Still, it has to be at least accounted for an error of $\pm 1\%$ for the spatially averaged albedo analysed by the model. The model has only been applied to the conditions in April and validations with measurements are limited to two regions in the western Arctic.

As an alternative to the albedo distribution obtained by the model, satellite products exist for which the albedo has been calculated from measurements of the reflected radiance at few narrowband channel in the VIS and NIR. One example that will be discussed here is the surface albedo (SAL) product of the climate monitoring SAF (CMSAF) in the EUMETSAT network. The broadband albedo values for the sea-ice area are derived from narrowband measurements with the Advenced Very High Resolution Radiometer (AVHRR) channels 1 and 2 (0.58-0.68 µm and 0.725-1 µm) by the narrow-to-broadband conversion algorithm by Xiong et al. [2002]. The satellite derived quantity is the black-sky surface albedo. It is the integral of radiation reflected from a single incident direction towards all viewing directions in the zenithal and azimuthal planes [Karlsson et al., 2013]. The black-sky albedo is therefore a substantially different quantity than the albedo of both direct and diffuse radiation treated in this study.

Figure 5.6 shows a map of the difference between the modelled albedo distribution and the black-sky albedo from the CMSAF SAL product where data from both sources are available. The SAL product distributed via the CMSAF homepage[2] covers the Arctic only up to 85°N. The map reveals a relatively constant difference between the albedo values of about 10%. Validations of the SAL product with the Surface Heat Balance of the Arctic Ocean (SHEBA) Project and Tara floating ice camps have shown that the surface albedo can be retrieved with a relative accuracy no better than 5 to 15% (see Karlsson et al. [2013] and references therein for information about the validations). Nevertheless, this uncertainty likely does not explain the difference to the model results described here. Also errors in the normalisation of the albedo with respect to an SZA of 60° does not explain an offset in the order of 0.1 [Karlsson et al., 2013]. It is more likely that the difference arises mostly from the difference of the albedo quantities since diffuse radiation has an effect on the broadband albedo (Section 3.3). Furthermore, also the airborne measurements (Figure 5.4) show higher broadband albedo values than the SAL product. Thence, it is not possible to directly compare the different quantities calculated in the two products. Unfortunately, it is not implemented in SoSIM to calculate the albedo of only direct irradiance, thus the black-sky albedo was not modelled in this study. Nevertheless, it can be concluded from this comparison (Figure 5.6), that the modelled albedo reveals a consistent behaviour also in the Inner and Eastern Arctic, where no measurements from the PAMARCMiP campaigns are available for a validation.

The computation of a surface broadband albedo from satellite-borne radiance measurements is a complex task with several possible sources of error. Substantial contributors to its uncertainty are the narrow-to-broadband conversion, masking of clouds, directional aspects of the surface reflectance and instrument calibration [e. g. Karlsson et al., 2013, Xiong et al., 2002]. The relatively simple model formulated here, that derives the spatial variability of Arctic sea-ice albedo from radar and microwave satellite instruments, circumnavigates these essential problems. The satellite products, which the model is based upon, are not influenced by clouds and the optical radiative transfer is entirely done by model calculations. Besides these advantages, the model, as formulated here,

---

[2]The SAL product is distributed via the website http://www.cmsaf.eu, last visited 20.10.2014
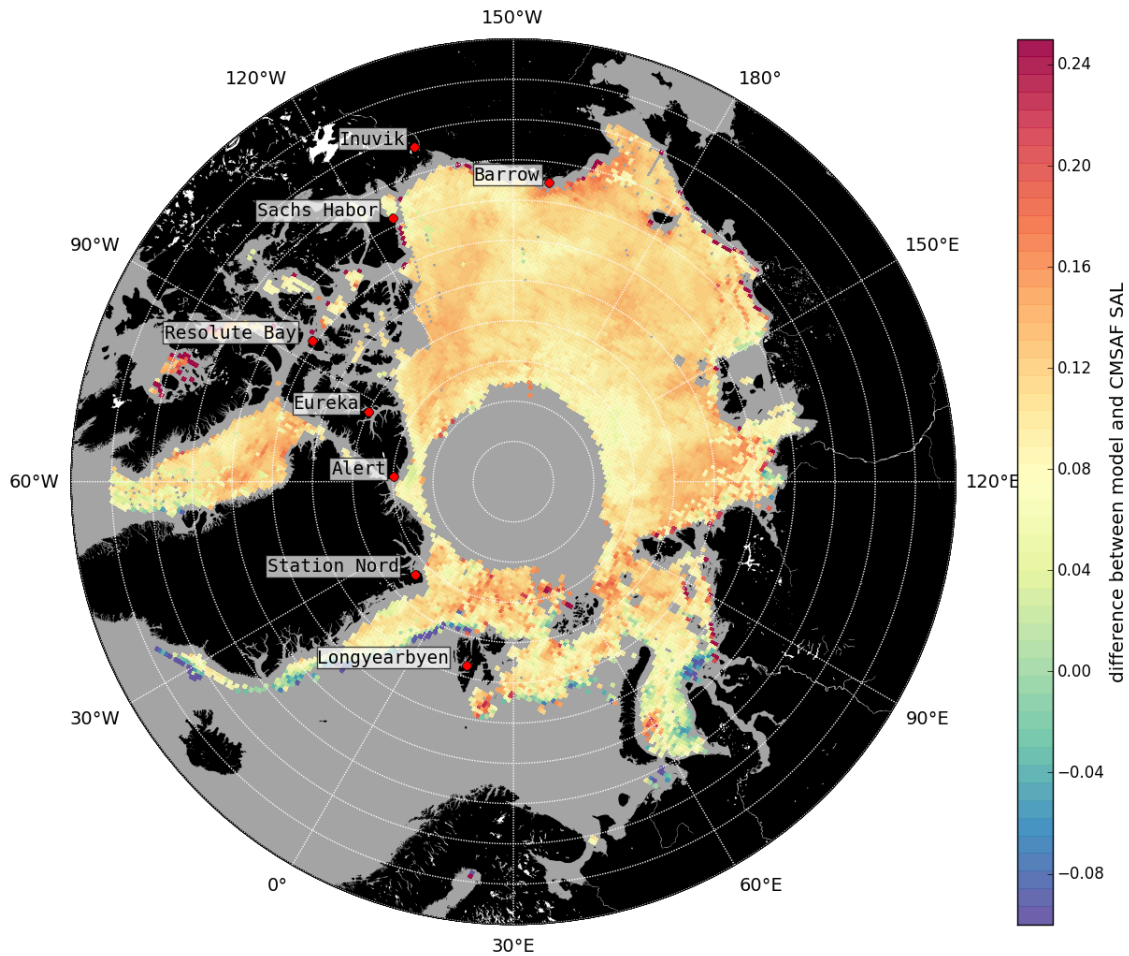
Figure 5.6: Map of the difference between modelled albedo (direct and diffuse) distribution
and the CMSAF SAL black-sky albedo product for the monthly mean of April 2011. Both
albedo distributions are normalised to an SZA of 60°.

is only able to predict the albedo for spring conditions without melting snow and ice. It cannot
produce precise predictions, mostly, due to the limitations regarding the input data. The model
needs further validation with measurements. However, with the coupling to SoSIM, this model is a
valuable tool that will be used in Section 5.3 to determine the surface forcing of changes to the
snow cover on Arctic sea ice – including spatial differences.

5.2   BC in the Arctic local-climate system

The Arctic polar air mass is clean compared to the atmosphere over the Eurasian and North
American continents as it is mostly free of any sources of natural aerosols as desert dust and
anthropogenic pollutants such as BC. An evaluation of the aerosol measurements from PAMAR-
CMiP'09 by Stone et al. [2010] support this general expectation. The high static stability of the
cold polar air mass inhibits a mixing with air masses with higher aerosol burden from further south.

However, there are events during which the meteorological situation allows a long-range transport of pollutants into the Arctic. There are many reports of layers of pollutants in the Arctic atmosphere from December to April – a phenomenon known as *Arctic Haze* and thought to be mostly composed of BC, dust, and sulphates [Barrie, 1986]. Studies of Arctic Haze in the 1980s showed that most of the aerosols originated in Europe and the Former Soviet Union, as reviewed by Barrie [1986]. After the collapse of the Former Soviet Union economy, emissions declined sharply. Stone et al. [2010] find much lower mass concentrations of BC aerosols in recent years than observed in the 1980s but they also find a positive trend, indicating that the reduced BC emissions are not permanent. Clarke and Noone [1984] find typical BC amounts in Arctic snow of 10 to 50 ng/g in the 1980s, which is, again, more than the typical 10 ng/g that have been observed in snow samples in recent years (Section 3.2).

A particular feature of the Arctic atmosphere is the stable atmospheric boundary layer. This suppresses heat exchange with upper layers and the surface temperature response is closely related to radiative fluxes at or near the surface. The surface radiation balance can be perturbed by depositions of BC into a snow layer, which enhances the absorption of shortwave radiation. Ice and snow surfaces are very vulnerable to warming via the ice-albedo feedback. This feedback includes, besides the complete melt of snow or ice exposing darker surfaces, also snow metamorphism processes. These processes lead to growing snow grains that will lower the albedo thus increasing the energy available for further temperature rise. Snow metamorphism is more effective at temperatures closer to the melting point (Section 2.2).

The ice-albedo feedback is a substantial natural process during Arctic spring that leads to the start of the melting season. However, where extra energy absorbed by BC is available for surface heating, the temperature of the snowpack rises. This triggers the feedback processes that will accelerate the albedo decrease by snow grain metamorphism and enhance the absorption of solar energy. According to Hansen and Nazarenko [2004], this may result in an earlier start of the melting period. Therefore, they found BC in the high latitudes to be twice as effective as carbon dioxide in changing the global surface air temperature, given the same perturbation of the energy balance (in W/m^2), because all energy is directly deposited into the snow. Hansen and Nazarenko [2004] estimate a global radiative forcing of $0.3\,W/m^2$ for the effect of BC on snow and ice albedo in the Northern Hemisphere. The recent AR5 of the IPCC states a new estimate of 0.04 (0.02 to 0.09) W/m^2 for the radiative forcing, but this estimate is still given a low confidence since processes need deeper scientific understanding Stocker et al. [2013].

In the following, quantifying the effect of BC depositions onto snow covered Arctic sea ice will be approached. For reasons of feasibility, this study will only investigating changes of the surface shortwave energy balance – the surface forcing. It will be evaluated decoupled from other components of the climate system.

First of all, the amount of shortwave energy being absorbed at a surface depends on its albedo and the amount of incoming solar radiation and can be calculated from quantities defined in Section 2.3.3 as:

$$E_{\text{absorbed}}(\lambda) = (1 - \alpha(\lambda))E^{\downarrow}(\lambda). \tag{5.1}$$

Of concern in this section is the surface forcing, a term that refers to the instantaneous perturbation of the surface radiative balance by a forcing agent [Ramaswamy et al., 2001]. The surface forcing is here explicitly defined as the difference in the absorbed energy due to a change in surface albedo from state 1 to state 2:

$$SF(\lambda) = E_{\text{absorbed},2}(\lambda) - E_{\text{absorbed},1}(\lambda). \tag{5.2}$$

The spectral distribution of the solar energy absorbed by a snow volume has been calculated with results obtained with SoSIM after Equation 5.2. The incoming solar radiation for these calculations
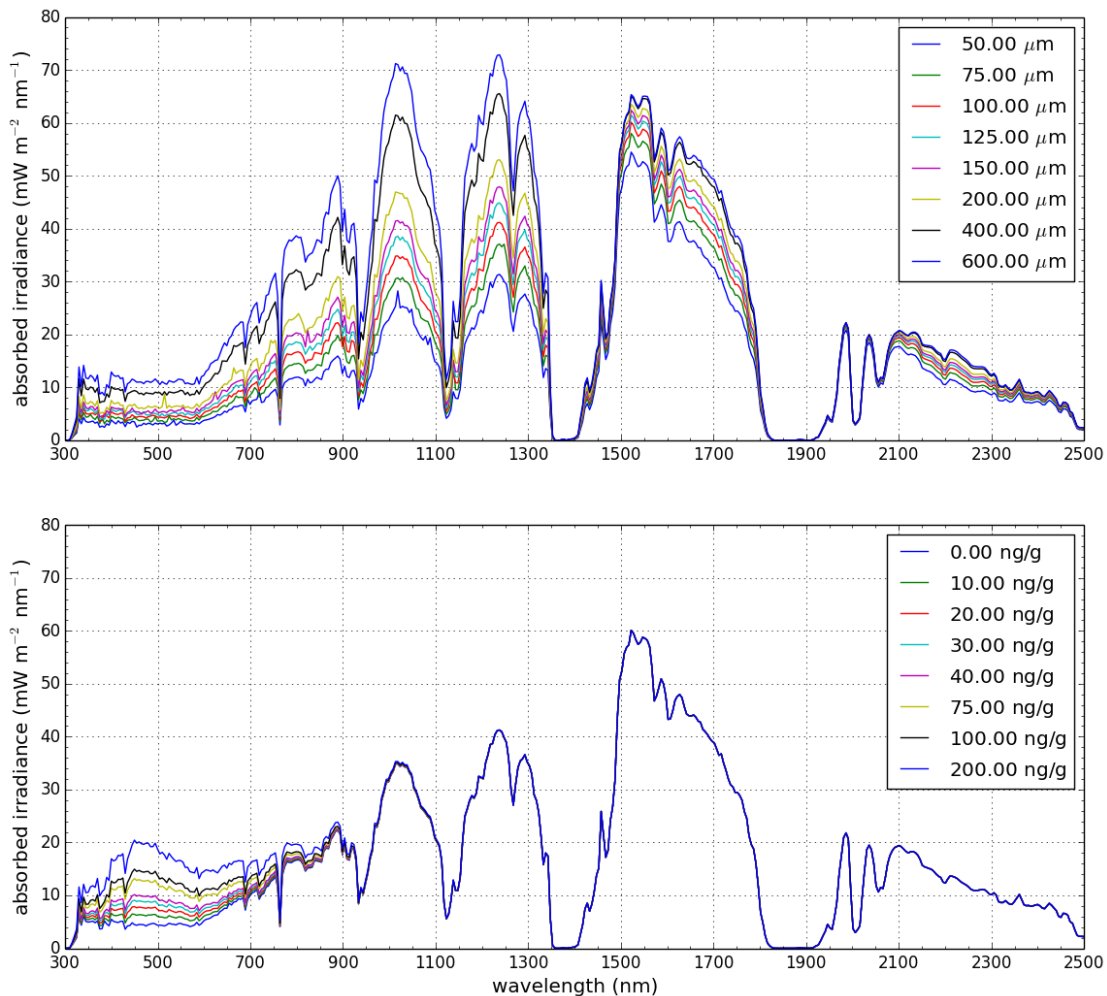
Figure 5.7: Spectral distribution of the solar irradiance absorbed in a snow volume for: pure snow of various snow grain radii (top); and different concentrations of BC within snow consisting of $r_{\text{eff}} = 100\,\mu\text{m}$ grains (bottom).

resembled Arctic winter conditions with a SZA of 75°. The results are presented in Figure 5.7. Despite most of the solar energy is found in the VIS, the NIR range has a large contribution to the total absorbed energy. Snow grain size has a strong influence on the absorbed energy over the entire spectral range, with the strongest influence between 750 and 1350 nm (Figure 5.7, top). BC content in snow, however, only significantly changes the amount of absorbed energy below about 950 nm, as shown in Figure 5.7, bottom, for snow consisting of 100 µm grains. The next section will evaluate the spatial variability of the surface forcing according to Equation 5.2, but integrated over the solar spectrum from 280 to 3000 nm.

5.3 Estimated surface forcing of BC in snow on Arctic sea ice

It has been demonstrated in the previous section that BC has the potential to decrease the surface albedo, thus to increase the amount of energy absorbed at the surface. How much energy is absorbed at the surface, of course, is not only a question of the surface albedo, but also of how much energy reaches the surface (Equation 5.1). Atmospheric state and, first of all, clouds modify the energy supply. Clouds may mitigate the effects of BC on the surface by reflecting and absorbing a share of the incoming radiation which is then not available for surface heating. Also, the magnitude of the decreasing effect of BC on the snow albedo depends on snow grain size and snow (physical/optical) thickness, the latter has a spatial variability in the model. Thus, the effect of BC will show a regional variability. Furthermore, it can be expected that BC is not distributed homogeneously in the Arctic due to the spatial differences in sources and transport mechanisms [Stone et al., 2010]. However, this study will, as a first step, estimate what surface forcing a certain, fixed amount of BC in the snow has in different regions of the Arctic sea-ice area. This estimate can be used, in another step, to calculate the true effect of the local BC concentrations in snow, if they are known from measurements or transport models. This can then be the basis for a further study estimating the radiative forcing of BC in snow using GCMs featuring snow metamorphism processes that may be triggered by the surface forcing of BC (Section 5.2).

The scenario that will be investigated in the following is adding BC in a concentration of 40 ng/g to pure, medium aged snow with a grain radius of 100 µm. As discussed in Chapter 3, this is a relatively high concentration for snow in pristine regions as the Arctic. Such high values were observed in the 1980s but are rare today. The effect of adding BC to the snow volume is shown as a map in Figure 5.8. The albedo is lowered by up to 0.8% in the multi-year ice region of the Western Arctic where the snow is thickest. Where the snow is thinner, the effect of BC lowering the albedo is weaker. A reason might be the lower optical thickness of the thinner snow cover, because an optical thin snow cover, with the darker underlying ground shining through, may conceal the effect of BC in the snow (see Section 3.3).

In order to calculate the energy that is absorbed in every grid cell according to Equation 5.1, it has to be known how much energy reaches the surface. Data on the energy supply to the sea-ice surface
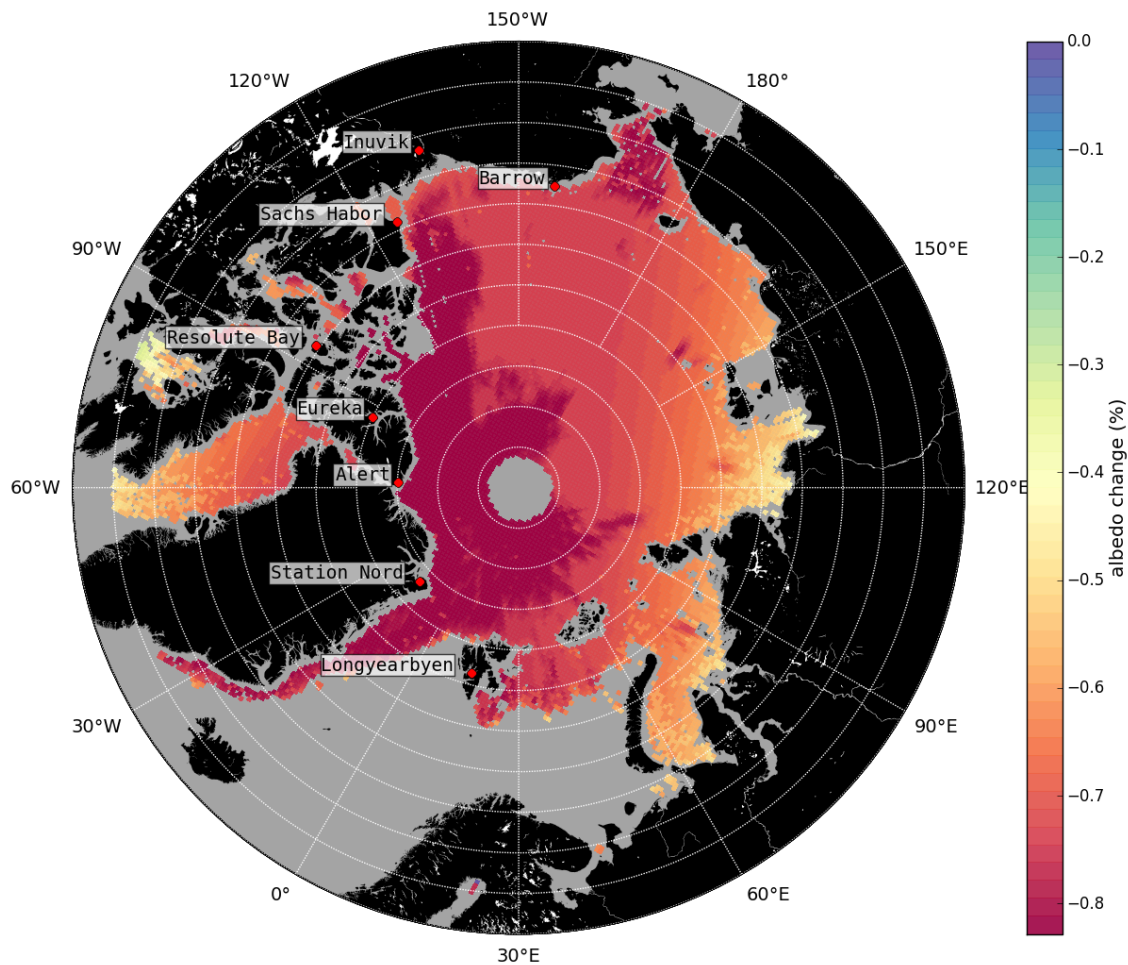
Figure 5.8: Map of change in surface albedo due to adding $40\,\mathrm{ng/g}$ BC to a pure snow cover consisting of grains $100\,\mathrm{\mu m}$ in radius. The BC is evenly distributed over the entire sea-ice area.

for this evaluation has been taken from the ECMWF (European Centre for Medium-Range Weather Forecasts) re-analysis product ERA Interim. From the synoptic monthly mean of the surface solar downward radiation with respect to the monthly mean cloud conditions, the daytime average has been calculated. The ERA Interim data also had to be re-sampled to the equal-area projection of the EASE2.0 grid, which is used for the CryoSat-2 data and the albedo distribution computed from it. The spatial distribution of the daily incoming solar radiation is shown in Figure 5.9.

The surface forcing of a changed albedo is now evaluated as the energy additionally absorbed by BC compared to the reference state of pure snow. The change in surface albedo described above results in the forcing shown in Figure 5.10. Spatial variability is caused by the average presence of clouds and incoming solar irradiance changing with latitude. The forcing is strongest in the Eastern Arctic and south of $70°\mathrm{N}$, where the surface forcing reaches 2.5 to $3.3\,\mathrm{W/m^2}$. Averaged over the entire sea-ice area, the surface forcing of an increase of C_{BC} from 0 to $40\,\mathrm{ng/g}$ is estimated to be $1.58\,\mathrm{W/m^2}$.
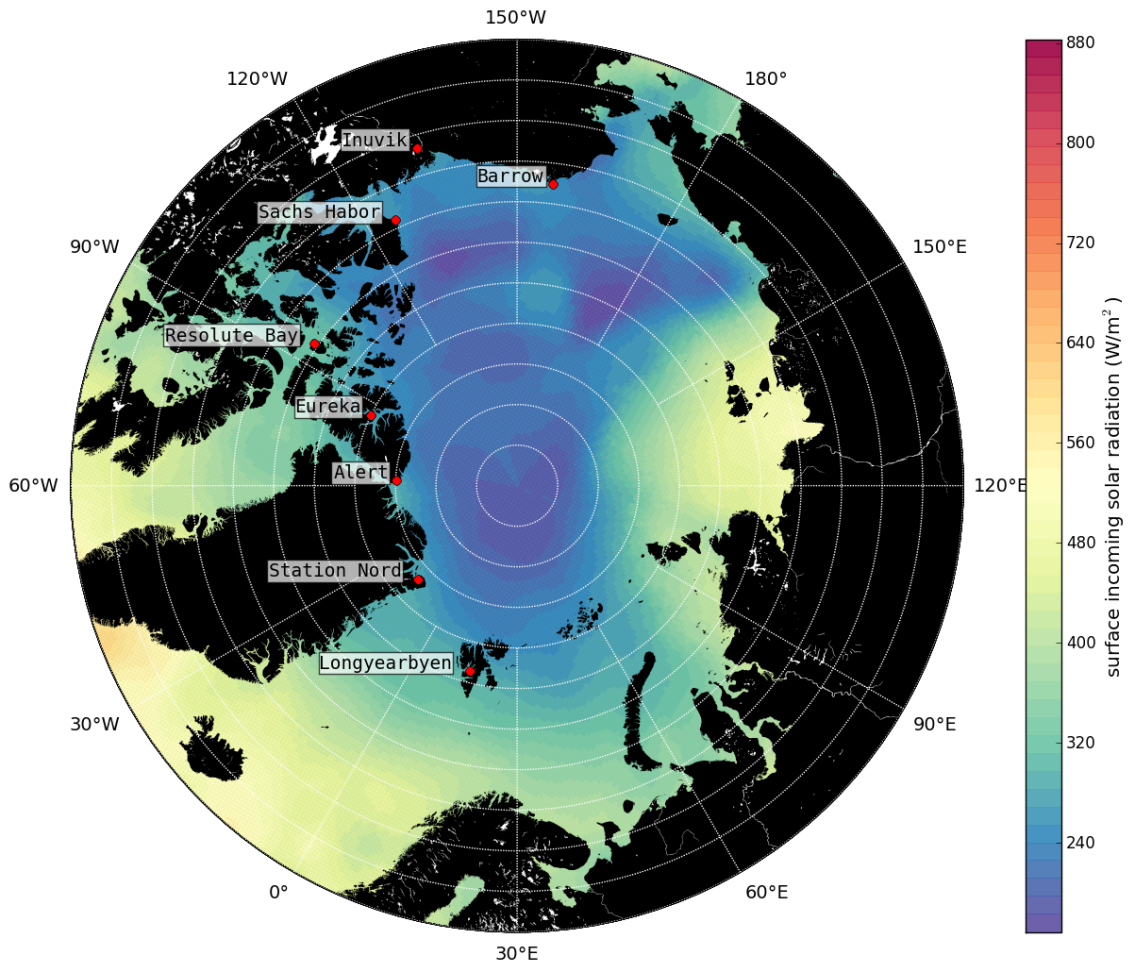
Figure 5.9: Incoming solar radiation at the surface as a mean value for April 2011 with respect to mean cloud conditions. Plotted with data from the ECMWF ERA-Interim re-analysis product and only shown over the oceans.

In the following, the uncertainty of the estimated surface forcing will be evaluated. One contribution is that the albedo reduction due to BC in snow depends on snow grain size (see Figure 3.7). The true local snow grain size is unknown. Since the albedo is calculated for monthly average snow conditions and snow grains tend to grow asymptotically, it is reasonable to assume a snow grain radius of $100\,\mu\text{m}$ for mean conditions without melting. However, deviations are likely and would introduce some uncertainty to the calculations of the surface forcing. Therefore, also *bracketing* calculations with snow grains of $25\,\mu\text{m}$ larger and smaller radius have been conducted and the resulting uncertainty has been calculated as a RMS (root mean square) difference [Willmott and Matsuura, 2005]:

$$\Delta SF = \sqrt{1/2 \cdot ((SF_{75\,\mu\text{m}} - SF_{100\,\mu\text{m}})^2 + (SF_{125\,\mu\text{m}} - SF_{100\,\mu\text{m}})^2)}. \tag{5.3}$$

This specific uncertainty for the surface forcing is presented in Figure 5.11. The average uncertainty is evaluated as $0.15\,\text{W/m}^2$ or 9.5%. The map reveals that the uncertainty is particularly high in
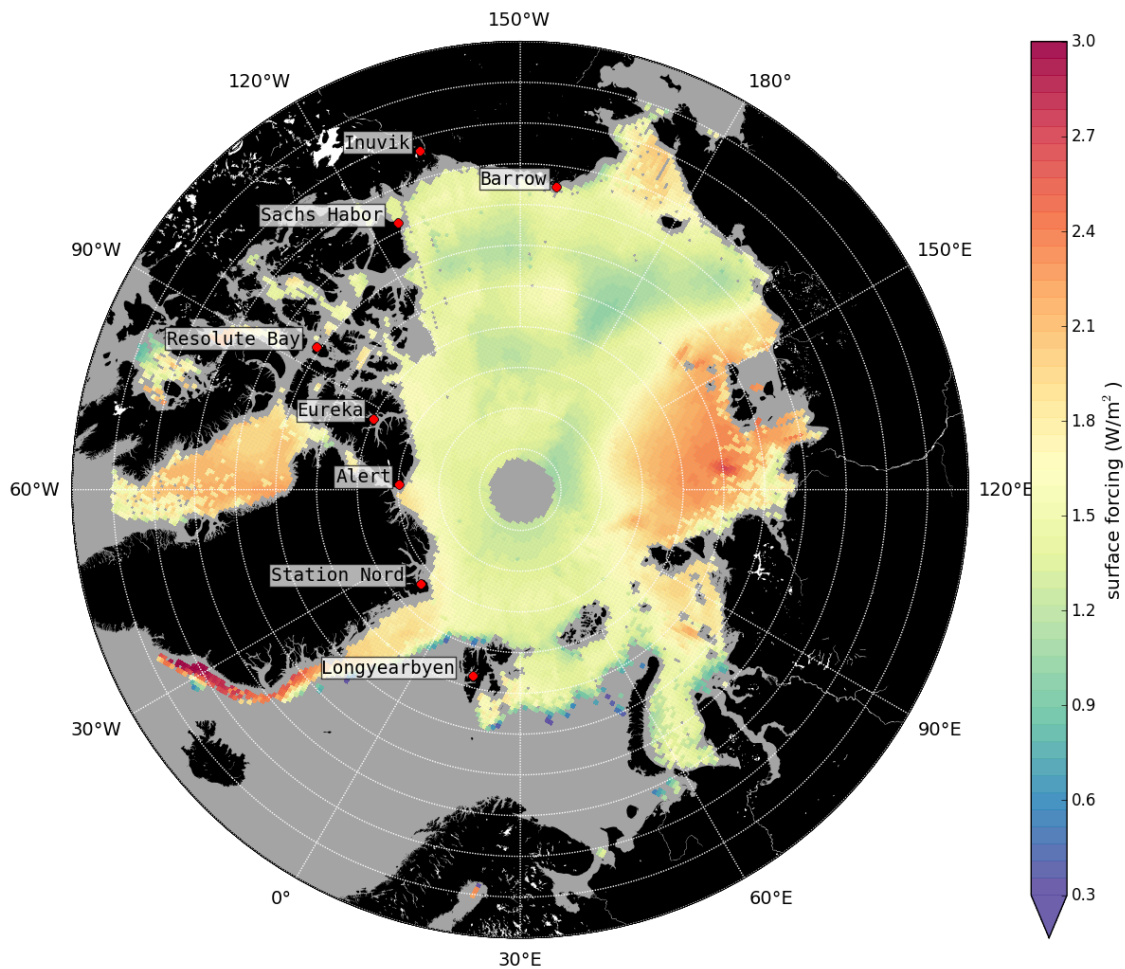
Figure 5.10: Additionally absorbed irradiance due to adding a concentration of 40 ng/g BC to pure snow of 100 mu m grain size for the mean sea-ice conditions and incoming solar radiation for April 2011.

areas of high incoming solar irradiance and areas of thicker snow.

When snow is optically thin and the darker ground underneath the snowpack influences the albedo, the albedo reduction of BC can be concealed (see Figure 3.9). The validation of the modelled albedo with instantaneous line measurements in the previous section (Figure 5.5) revealed local deviations of the climatological snow thickness from the true conditions. Since the effect of BC absorption is influenced by the snow optical thickness, the uncertain distribution of snow thickness has to be accounted for. Figure 5.8 reveals a difference of the albedo reduction between areas of thicker and thinner snow of about 5%. This translates into an uncertainty of the estimated surface forcing of $\pm 0.08 \, \text{W/m}^2$.

Furthermore, there is a relatively large uncertainty in the MAC of BC, the property that describes how efficient absorption by a certain mass concentration of BC is. There is likely an enhancement of the MAC due to coating of the particles with non-carbonaceous substances during their atmospheric stay and due to the unknown mixing state of the particles in snow (see sections 2.4 and 3.3). The
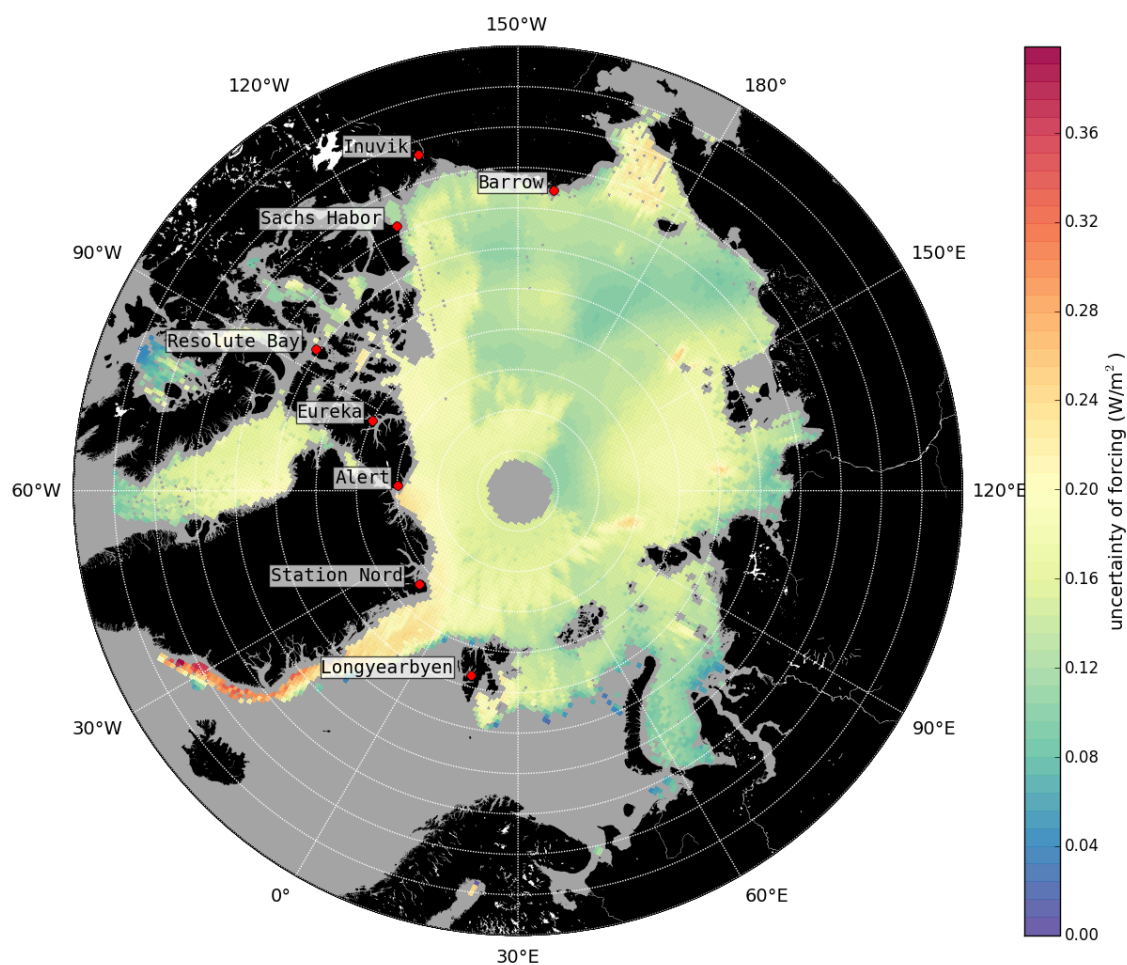
Figure 5.11: Uncertainty of the surface forcing of adding a concentration of 40 ng/g BC to pure snow due to the effect of snow grain size on BC absorption.

calculations listed in Table 3.2 reveal a 0.3% stronger decrease of the broadband albedo for BC absorption enhanced by a factor of 1.5 due to ageing processes as suggested by Bond and Bergstrom [2006]. Therefore, the additional absorption caused by BC might as well be 0.54 W/m² more on average. Thus, this is a large contributor to the uncertainty of the surface forcing of BC on Arctic sea ice.

Conclusion

The average surface forcing for the scenario of rising the BC content in the snow cover of the Arctic sea ice from 0 to 40 ng/g has been evaluated as 1.58 W/m². The uncertainty of this average forcing is ±(0.21 + 0.08) W/m² and if the higher MAC of BC applies for the Arctic, the average forcing might as well be 0.54 W/m² higher. The forcing varies between 0.0 and 3.3 W/m² within different regions of Arctic sea-ice area (Figure 5.10). These values are plausible for an albedo reduction of about 0.5 to 1.0% and an average irradiance of 250 to 500 W/m². If the surface forcing by such a deposition of BC aerosol onto the snow triggers snow grain growth, the albedo would be

decreased further. Increasing the snow grain size from an effective radius of 100 to 125 μm induces an average surface forcing of $2.8\,\mathrm{W/m^2}$ to the snow covered sea-ice (Figure A.2 in the appendix). This forcing also has a regional dependence and varies between about 1.5 and $5.0\,\mathrm{W/m^2}$ according to the availability of surface radiation (Figure 5.9).

These two components of the surface forcing, together with the strong static stability of the boundary layer above the sea ice likely will rise the surface temperatures. In order to evaluate the radiative forcing in the sense of the IPCC Assessment Reports, this surface forcing now could be used within a GCM. Such a climate model can evaluate the impact onto the climate system by accounting for coupled processes like heating of the snowpack and snow metamorphism, as well as, treating the other terms of the surface energy balance such as longwave radiation and turbulent heat fluxes. The investigation in this study can only be a supporting basis for further studies.

The surface forcing evaluated here reveals a dependence on the ice regimes. BC absorption is stronger in the multi-year ice region than on seasonal sea ice where the snow cover is thinner (Figure 5.10). Hence, also the potential of BC to raise the near surface temperature is higher over multi-year ice than over the seasonal sea-ice cover. This feature depends on the optical thickness of a snowpack which is a non-linear function of physical snow depth (Section 3.3). With these findings in mind, it has to be stressed that the snow thickness distribution after the climatology by Warren et al. [1999], and modified according to Kurtz and Farrell [2011], that is used here is actually a poor estimate of the real conditions in some regions. Today, this climatology is widely used as a best estimate, e. g. in the CryoSat-2 sea-ice thickness product [Hendricks et al., 2013], knowing that differences of several tenth of centimetres are possible where the ocean is not covered by multi-year ice any more. There is an ongoing change of the Arctic sea ice towards more seasonal ice cover and changed winter time precipitation rates affect snow accumulation [Webster et al., 2014].

Snow albedo parametrisations in GCMs often employ a coarse representation of snow optical thickness, thus they likely cannot resolve the spatial differences in the surface forcing of BC, that were observed here. The results of this study could be used to parametrise a two dimensional surface forcing due to BC in a GCM in order to evaluate the radiative forcing of BC in snow on Arctic sea ice similar to the approach by Hansen and Nazarenko [2004]. For estimates of the radiative forcing from other studies see the discussion in Section 5.2.

6. Discussion and outlook

This study focussed on the shortwave energy balance of Arctic sea ice in early spring. The ice covered ocean reflects substantially more solar radiation than open water surfaces, thus steering a part of the energy and heat uptake into the global climate system. A snow cover on top of the ice, as present in large parts of the sea-ice area, rises the surface reflectance by up to 30% (see Figure 1.1). This also implies a strong possible variability of the reflectance induced by changes of the snow cover.

The goals of this study were to acquire knowledge of the physical processes governing the reflectance of snow covered sea ice and to quantify the variability each of these processes can cause. Necessary steps were to

- investigate the variability of the albedo of a snow cover due to changes of its microstructure and distribution of incident radiation with a radiative transfer model, and to

- characterise the variability of the albedo of heterogeneously snow covered sea ice on a regional scale from airborne measurements.

This was done in order to combine these results in an attempt to: transfer values that are modelled for homogeneous surface conditions to an Arctic wide representation of the spatially and temporally averaged sea-ice albedo, according to sea-ice and snow heterogeneities. The spatial information on the sea-ice conditions was obtained from satellite products of the sea-ice thickness and concentration, as well as a climatological snow depth distribution. Assumptions had to be made for the snow grain size.

The calculated spatial albedo distribution is coupled to a snow-albedo model, thus the spatial variability of albedo changes induced by single parameters can be evaluated. Furthermore, with the knowledge of the monthly mean irradiance at the surface, it is possible to evaluate the surface forcing of these albedo changes.

This chapter will discuss the major findings of the previous Chapters 3, 4 and 5 and give an outlook for necessary improvements and further studies.

Model study

Snow albedo models have been previously used to investigate changes of the reflectance of a snow cover due to altered microphysical parameters of the snowpack, atmospheric conditions diffusing the

incident radiation, effects of the SZA on light propagation in the snow and the presence of LAI in the snowpack. A model permitted the study of single parameters within a controlled environment. The incentive for this model study was to set up and test a sophisticated radiative transfer model, based on the DISORT method, in which the propagation of solar radiation in atmosphere and snowpack is coupled, thus allowing multiple reflections. The model setup developed here follows the principle of the setup formulated in the study by Gardner and Sharp [2010] and is specialised for the conditions in the Arctic and snow on top of sea ice. This *model*, called SoSIM, was used here for studies with a set of parameters that is expected to represent Arctic conditions based on literature research.

SoSIM is not only able to simulate the albedo of a snowpack, but also features of the atmosphere can be investigated. This is needed in order to study the effects of atmospheric backscatter on airborne surface albedo measurements as a function of altitude, as mentioned below in more detail. This type of model offers further possibilities for studies involving snow on the ground. For example, evaluating the impact of Arctic Haze on the energy balance of the boundary layer could be possible. Thus, there are further applications for SoSIM in connection with the diverse measurements conducted during airborne campaigns like PAMARCMiP. It would be possible to include measured vertical profiles of atmospheric state (e.g. temperature, pressure and humidity), aerosols, such as BC, and trace gases, such as ozone, into the model. However, even though this data was (partly) available for this thesis, the given time did not allow to prepare the data in a way that it could have been included into the model atmosphere properly. Nevertheless, there is a tool and data for further studies.

Comparison of model results

Model results of the spectral albedo were compared with a set of models based on different approaches, that are described in Section 2.5. The comparison was done with regard especially to the effects of BC added to the snow crystals. An agreement of the albedo reduction due to BC better than $\pm 1.1\%$ was found in the VIS. However, the model results reveal a slightly different sensitivity of the UV and VIS albedo to equal concentrations of BC in the snow. SoSIM showed very good agreement to other models in the wavelength region near $1300\,\text{nm}$, where the albedo is very sensitive to the microphysical properties of the snow and to the SZA. At higher wavelengths, the relative differences between model results are generally greater, especially near the absorption band of ice and water. Comparisons of the broadband albedo with values calculated with another model and a physically based parametrisation revealed an agreement better than about 1%. An attempt to re-simulate field measurements of the spectral albedo of a real snowpack with complex vertical structure demonstrated the complexity of snow reflectance. It could be achieved to generally match the measurements by tuning the model parameters. However, using spectral measurements as a sophisticated validation of SoSIM would need accurately known snow parameters and a less complex snow stratigraphy.

Albedo changes by single parameters

For typical conditions in the Arctic sea-ice area, it was found that the size of spherical snow grains and the angle of the sun above the horizon ultimately determine both spectral and broadband

albedo of a thick snow layer. At 1300 nm, doubling the snow grain size decreases the albedo by about 20%, while a lower incident angles of solar light can offset this effect. BC has a distinct influence on the albedo in the UV and VIS range of the solar spectrum. However, a realistic, but for Arctic conditions already high, BC concentration of 40 ng/g added to pure snow only lowers the spectral albedo by less than 2% around 500 nm and the broadband albedo is lowered by less than 1%. The effect depends on snow grain size and the MAC of BC, the property that describes how efficient absorption by a certain mass concentration of BC is. Nevertheless, the decreasing effect of BC or other light absorbing substances on snow albedo can be significant if a high mass concentration is present in the snow. It is known that the spectral signature of BC is very similar to that of a thinning snow cover on top of a darker surface [Warren, 2013, Wiscombe and Warren, 1980]. With the model results obtained here it can be shown that the two effects closely resemble each other for parameters that are likely to occur on Arctic sea ice (Figure 3.9).

Implications for modelling and measurements

The characteristic behaviour of the spectral albedo for changes of certain snow parameters could be used to formulate retrieval algorithms. A problem with all possible retrievals of snow properties from spectral albedo measurements is that too many factors influence the spectral albedo. Table 3.5 gives a priority of the parameters based on model calculations showing which albedo changes can be expected during measurements on Arctic sea ice. Parameters with high influence on the albedo have to be accurately known to infer others with smaller influence. A similar argumentation holds if parameters have to be assumed for modelling purposes. The following point can be seen as guidelines for measurements or modelling:

- The thickness of an optically thin snowpack has to be accurately known, however the albedo does not change significantly for a snow depth above 20 cm. A fixed value can be assumed for the snow density since changes influence the albedo by $\ll 1\%$ for most snowpacks.

- The SZA must be known with an accuracy of at least $\pm 1\%$ because of its strong influence on NIR albedo. This effect vanishes if no direct radiation reaches the snow surface, i. e. for an overcast sky.

- Changes of the snow grain size have a strong impact on the spectral albedo. If assumptions are made, the possible large uncertainties have to be accounted for.

When modelling the hemispheric reflectance, or albedo, the exact angular distribution of the reflected radiation is not of particular interest, therefore a description of all snow grains as equally sized spherical particles is feasible [Grenfell and Warren, 1999]. The approximation is favoured by the fact that angular details in the phase function of complex snow grains are smeared by multiple scattering [Warren, 1982]. However, a high SZA or very thin snow reduce the number of scattering events within the snowpack, thus a model utilising the assumption of spherical grains should be limited. SoSIM was not used to model snow below a thickness of 1 cm and an SZA above 80°.

Airborne measurements

Data from the PAMARCMiP campaigns, operated between end of March and beginning of May in 2009 and 2011, showed large variability and differences within single measurement flights, in different regions and from one campaign to the next. Yet, there might be limitations arising from the quality of the data and uncertainties of the measurements concerning possible interpretations of the data. Thus, the quality of the data had to be evaluated first, in order to interpret these measurements. The goal is to characterise the albedo variability caused by the heterogeneity of snow and ice conditions by putting the albedo data into a context with additional measurements.

Data quality and measurement uncertainties

The quality and uncertainty of the airborne broadband albedo measurements had not been previously documented in depth, thence there was a need to quantify the measurement uncertainty of this specific instrument setup. The instruments' sensitivities contribute with individual uncertainties. The exact sign and magnitude of the uncertainties may depend on the orientation of the sensor relative to the sun. Thus, it has to be assumed, that the uncertainties sum up to $\pm 4.1\%$. The instantaneous contribution of this uncertainty may vary, especially with flight direction (azimuth dependence of uncertainty). The same is true for the uncertainty of the flight attitude correction. This correction had been applied during post-processing of the data. Its uncertainty is evaluated as 7.0%, assuming that the built-in offset could not be evaluated with an accuracy better than $\pm 1°$ for the campaign in 2009. This extra uncertainty does not apply for the campaign in 2011. Data from the campaign in 2009 showed numerous occurrences of unrealistically high albedo values. The erroneous built-in offset correction might explain this and data from this campaign cannot be evaluated in terms on absolute values.

It is possible that the measured surface albedo is significantly biased by backscatter radiation of the atmosphere below the aeroplane. A correction of atmospheric influences as a function of altitude above ground level according to the method of Wendisch et al. [2004] has been tested. Simulations with SoSIM revealed that the measured albedo over a highly reflective snow surface will decrease with altitude of the sensor above ground level, while Wendisch et al. [2004] investigated the effects over dark ocean and land surfaces and found the opposite effect. For the relatively low operational flight altitude during the measurements ($90\,\mathrm{m}$), the expected underestimation of the surface albedo is low ($-0.5 \pm 0.5\%$). The small, typical variations of the flight altitude of about $\pm 20\,\mathrm{m}$ have minor impact. Thus, a correction of the measurements has been rejected in order not to introduce new and even larger uncertainties by possible false corrections [Wendisch et al., 2004].

In order to account a change in the measured albedo to a change in snow parameters, the change must be significantly higher than the measurement uncertainty. This could be the case for the expected variability of the broadband albedo induced from changes in snow grain size (in the order of 10%) but not for changes of the BC content in the snow (less than 1%).

Influence of surface heterogeneities

The albedo measurements over the Beaufort Sea and Fram Strait demonstrate the influence of

differently scaled surface heterogeneities. The resulting albedo measurement is a folding of the spatial distribution of different surface types and the signal-weighting characteristics of the sensor. Parallel measurements of sea-ice thickness and photographs taken with an automated camera system helped to characterise the surface features that influence the measured albedo. To evaluate the photographs, a simple threshold value based algorithm has been developed, classifying each pixel as snow, bare ice or open water and, furthermore, detecting shadowed areas. The result served as an indicator for rather homogeneous or heterogeneous surface conditions, which proofed as valuable extra information for the interpretation of the albedo data. Leads (covered with new ice or open water) cause a drop of the albedo signal. The minimum depends on the size of the lead and on the fraction of open water. Shadows and reflections due to ridges cause a sinusoidal behaviour of the measured albedo signal with an amplitude of about 0.03. The effects of ridges can be attenuated by an average over a larger area, e.g. by temporal averaging [Gallet et al., 2011]. The temporal average must be long enough, otherwise the average might be superimposed by surface heterogeneities.

Implications

Averaged broadband albedo measurements from the flight leg near Alert reveal values between 0.81 to 0.84. An attempt to re-simulate the values with SoSIM revealed values in the same rage, although no exact input parameters were known. This intercomparison indicates that the obtained vales are coherent. Values from previously published literature also support the results. These investigations helped to characterise the variation of the measured albedo signal. Signal drops in the vicinity of leads actually imply a change in surface energy balance due to the surface covers with different albedo. Leads can be detected by the sea-ice thickness measurements. The sinusoidal response of the albedo measurements to ridges is a bias and has to be filtered out, since it does not resemble the true surface energy balance. The interpretation of the measured albedo time series is ambiguous, if no additional information about the surface conditions are available.

Improvements

Broadband albedo measurements are not adequate for sophisticated evaluations of snow surface reflectance. The spectral characteristics of albedo changes by single snow parameters are smeared in broadband measurements. Therefore, the measurement setup should be extended by spectral measurements – as argued in Section 4.7. Furthermore, this study emphasises that radiation-box-patterns for calibration purposes are flown, instrument domes are cleaned and clouds are documented during future campaigns. This might decrease uncertainties and increase the availability of data.

Spatial distribution of sea-ice albedo

In case that very different surface types appear within the footprint of a sensor, the measured albedo will be a complex mixture between the individual albedo values of the surfaces. With this understanding, that helped to interpret the airborne albedo measurements, it was also possible to bridge the gap between modelled spot measurements and measurements representative for a

larger area. The formulated approach transfers values that were modelled for homogeneous surface conditions to an Arctic wide representation of the spatially averaged albedo for the monthly mean sea-ice conditions – an *albedo map*.

Spatial knowledge about the parameters with most influence on the albedo were used to choose albedo values from a look-up-table calculated with SoSIM and alter these values according to sea-ice and snow heterogeneities. The spatial information on the sea-ice conditions were obtained from satellite products of the sea-ice thickness and concentration, as well as a climatological snow depth distribution, all of which is combined in the CryoSat-2 sea-ice thickness product [Hendricks et al., 2013]. Assumptions had to be made for the snow grain size.

Quality of the result

First comparisons of the modelled spatial albedo distribution with air and satellite borne albedo measurements showed that the modelled albedo is plausible. For the case study in April 2011, the agreement to airborne measurements is about $\pm 5\%$ at three spots in the Western Arctic. The model values did not accurately resemble the measurements. Yet, the spatially averaged measurements are likely not representative for the area and time span for which the model values are calculated. Thus, the model lacks a sophisticated validation. A quantitative comparison to an alternative satellite product, derived from radiance measurements in the VIS and NIR [Xiong et al., 2002], indicated the consistency of the modelled values also in the Central and Eastern Arctic.

Improvements

The goal of formulating a sophisticated model, based on physical principles, that is able to calculate the distribution of albedo values in the Arctic sea-ice area succeeded. However, the results may not improve until a better testing of the model can be achieved.

Limitations of the accuracy of modelled albedo values are mostly caused by the quality and spatial resolution of the input parameters. Especially information on the distribution of snow depth on the sea ice with better resolution and accuracy, than the modified climatology by Warren et al. [1999], would improve the model results. There is recent research activity trying to improve snow thickness distributions so they account for the ongoing change of the Arctic sea ice towards more seasonal ice cover and the changed winter time precipitation rates that affect snow accumulation [Webster et al., 2014].

During the research for this model, no source for data on the spatial distribution of snow grain size on Arctic sea ice could be found. However, there is ongoing work trying to derive spatial snow grain size distributions from satellite measurements [e. g. Zege et al., 2011]. This information would improve the estimate of the albedo in general, and also that of regional differences.

The model, as formulated here, can only describe the albedo for winter and spring conditions without melting. To extend the model principle to the melting season, new and complex simulations with SoSIM or another snow-albedo model would be necessary to account for the albedo development of wet, melting snow. New surface heterogeneities would be introduced, e. g. by melt ponds and rain for which spatial information would be needed.

Climate impact of albedo changes

The potential of BC to decrease the surface albedo, thus to increase the amount of energy absorbed at the surface, has been demonstrated. Since the calculated spatial albedo distribution is coupled to a snow-albedo model, the spatial variability of albedo changes induced by one single parameter, such as BC, can be evaluated.

It has been found that the average surface forcing for the scenario of rising the BC content in the snow from 0 to 40 ng/g causes a surface forcing of $1.58 \pm 0.29\,\mathrm{W/m^2}$, but this value might as well be $0.54\,\mathrm{W/m^2}$ higher. This deviation is caused by the uncertainty of the mass specific absorption cross section (MAC) of BC. It is likely that the MAC is enhanced by a factor of 1.5 due to ageing processes during its atmospheric stay. However, no consistent value for the MAC of BC in the Arctic atmosphere can be found in literature.

The surface forcing of BC is stronger in the multi-year ice region than on seasonal sea ice, where the snow cover is thinner, because it depends on the optical thickness. With this in mind, it has to be stressed that the snow thickness distribution used here is actually a poor estimate of the real conditions in some regions, albeit it is often the best information available. Same as for the general representation of albedo values, as stated above, also the estimated surface forcing would improve in accuracy if a more accurate snow thickness distribution would be available.

Hansen and Nazarenko [2004] argue that a surface forcing triggers feedback processes that will accelerate the albedo decrease by snow grain metamorphism and enhance the absorption of solar energy. It was found with this model, that increasing the snow grain size from an effective radius of 100 to 125 μm induces a surface forcing of $2.8\,\mathrm{W/m^2}$, averaged over the area of snow covered sea-ice.

Reducing the uncertainty of the surface forcing by BC
Better knowledge of the MAC would reduce the uncertainty of the calculated albedo reduction and surface forcing of BC in snow. Measurements of BC aerosol with the SP2, an instrument flown aboard Polar 5 during the PAMARCMiP campaigns (Section 4.4), could reveal information about the coating of BC particles. Furthermore, a better understanding of the spatial distribution of BC in the Arctic, together with particle mass and absorption capabilities, would be an advance for future investigations of spatial differences of the radiative forcing of BC aerosols and the amount of BC deposited onto the sea ice. Measurements of the BC content in snow are not as widespread as measurements of atmospheric concentrations. Clarke and Noone [1984] found a consistent *scavenging ratio* relating BC amounts in the snow to concentrations in the atmosphere. Future studies could utilise this ratio to estimate BC concentrations in the snow from atmospheric measurements with the SP2. The three-dimensional distribution of BC in the Arctic is often estimated wrong by models [Samset et al., 2014]. Therefore, BC measurements in the Arctic are necessary for better estimates of the climate impact of BC emissions.

Radiative forcing

In order to evaluate the radiative forcing in the sense of the IPCC Assessment Reports, the estimates of the surface forcing from this study could be used to parametrise a surface forcing in a GCM (global circulation model), similar to the approach by Hansen and Nazarenko [2004]. It is necessary to evaluate the impact onto the climate system by accounting for coupled processes like heating of the snowpack and snow metamorphism, as well as, treating the other terms of the surface energy balance such as longwave radiation and turbulent heat fluxes. Such model studies were out of the scope for this thesis.

Appendices

A.   Additional figures
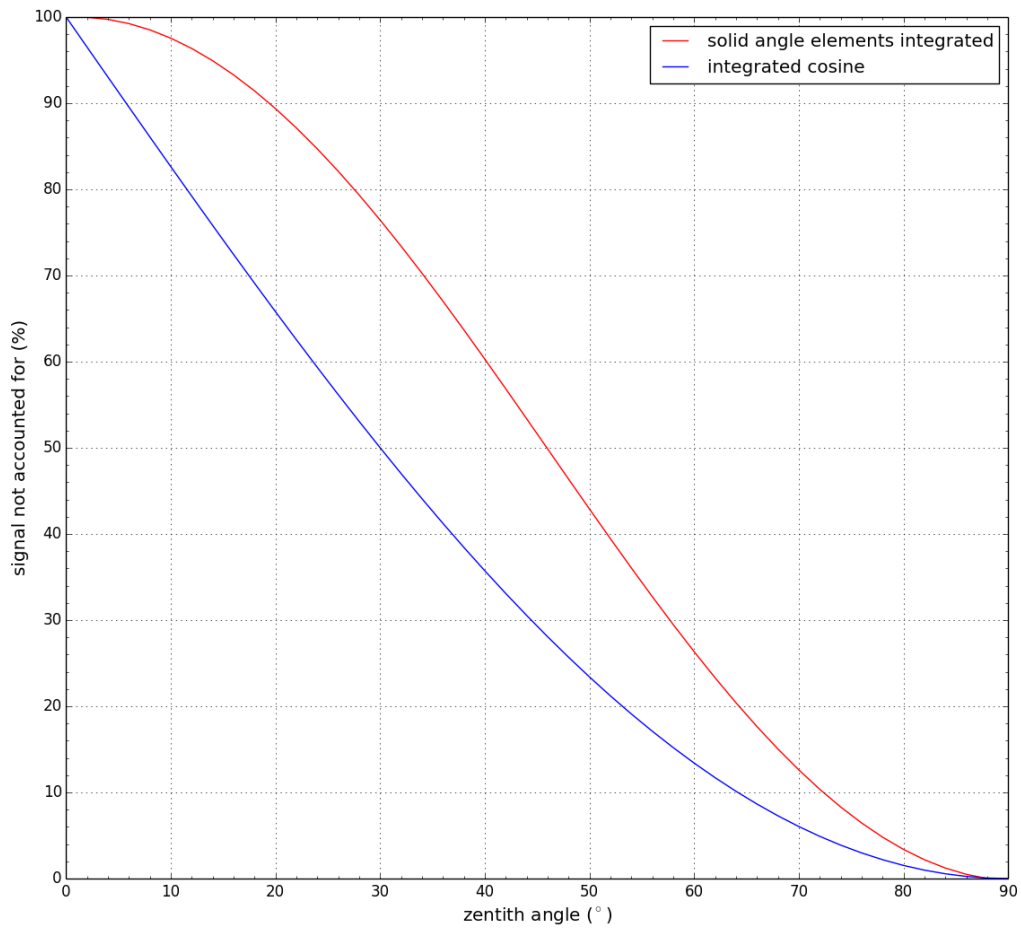
Figure A.1: Convergence of the signal received by a spherical cap compared to a full hemispheric receiver while increasing the surface of the cap. Assumed is a perfect cosine receiver. A spherical cap is defined as the part of the surface of a half-sphere from the zenith point down to a certain zenith angle $< 90°$. Evaluated is for the red curve: the cosine weighted integral over the solid angle elements for all azimuth angles and in increments of $1°$ for the zenith angle, divided by the full half-sphere; and for the blue curve: $\sin(\Delta$zenith angle$)$.
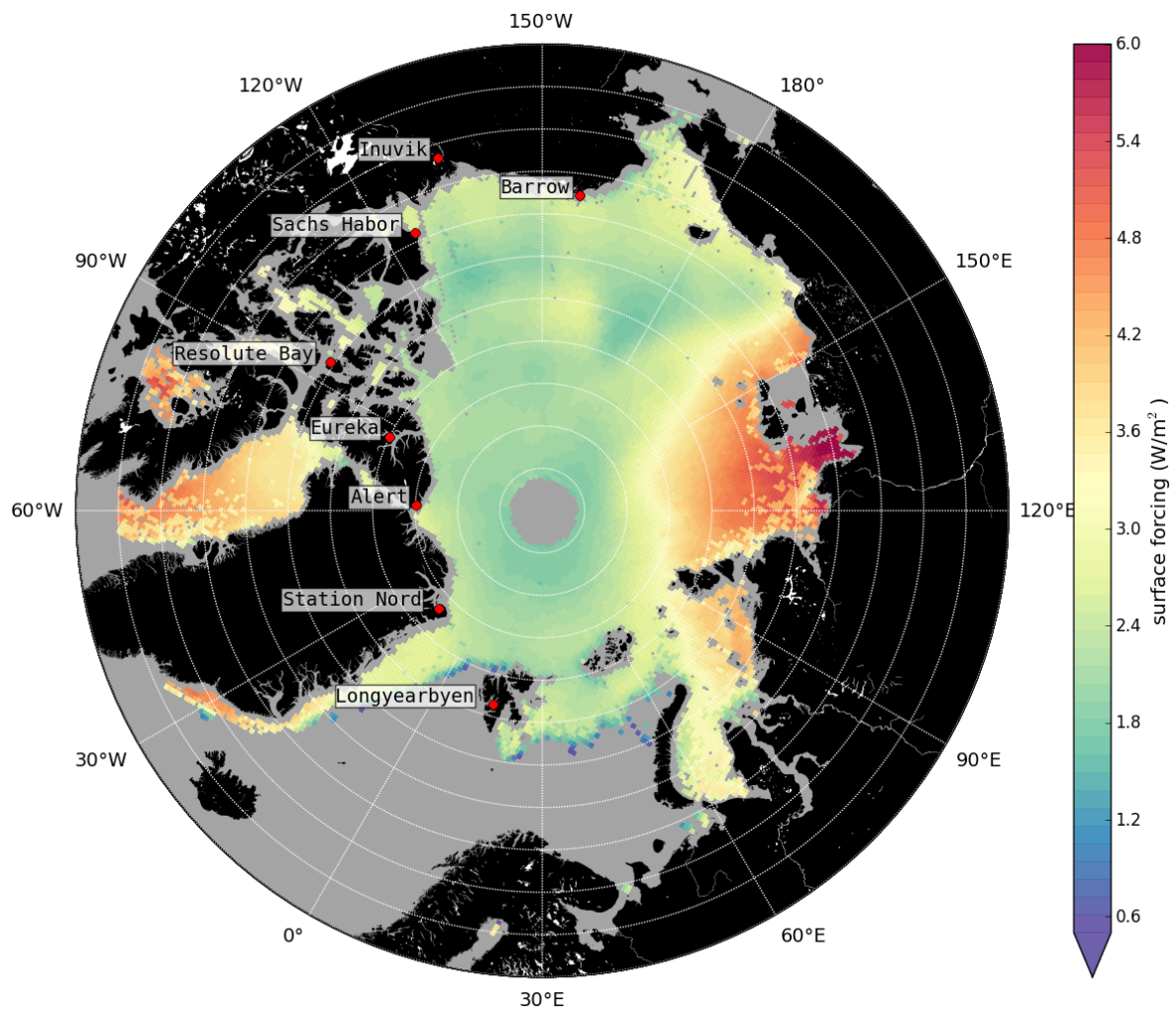
Figure A.2: Map of the regional surface forcing of an increase in snow grain effective radius from 100 to 125 μm.

List of Figures

List of Tables

List of abbreviations

UV	ultra violet	below 380 nm
VIS	visible	380 - 780 nm
NIR	near infrared	780 - 3000 nm

abs	absorption
ext	extinction
dif	diffuse
dir	direct
sca	scattering
m	measured

AGL	Above Ground Level
AOD	Aerosol Optical Depth
AR	Assessment Report
ASCAT	Advanced Scatterometer
AVHRR	Advanced Very High Resolution Radiometer
AW	Atlantic Waters
AWI	Alfred-Wegener Institute
BC	Black Carbon
BG	Beaufort Gyre
CCD	Charge-Coupled Device
CMOS	Complementary Metal-Oxide-Semiconductor
CMSAF	Climate Monitoring Satellite Application Facility
DISORT	Discrete-Ordinate

DSLR	Digital Single-Lens Reflex
DWD	Deutscher Wetterdienst
EM	Electromagnetic
EUMETSAT	European Organisation for the Exploitation of Meteorological Satellites
FOV	Field Of View
GCM	Global Circulation Model
GPL	General Public License
GPS	Global Positioning System
IMuK	Institute for Meteorology and Climatology
INS	Inertial Navigation System
IPCC	International Panel on Climate Change
LAI	Light Absorbing Impurity
LGGE	Laboratoire de Glaciologie et Geophysique de l'Environnement
MAC	Mass specific Absorption Cross-section
MODIS	Moderate-Resolution Imaging Spectroradiometer
NASA	National Aeronautics and Space Administration
OSI SAF	Ocean and Sea Ice Satellite Application Facility
PAMARCMiP	Polar Airborne Measurements and Arctic Regional Model Simulation Project
PMOD	Physikalisch-Meteorologisches Observatorium Davos
PSP	Precision Spectral Pyranometer
RGB	Red-Green-Blue
RTE	Radiative Transfer Equation
SAF	Satellite Application Facility
SAL	Surface Albedo
SAR	Synthetic Aperture Radar
SHEBA	Surface Heat Balance of the Arctic Ocean
SIRAL	SAR/Interferometric Radar Altimeter
SNICAR	Snow, Ice, and Aerosol Radiation (model)
SoSIM	Snow on Sea Ice Model
SSA	Specific Surface Area
SSM/I	Special Sensor Microwave/Imager
SZA	Solar Zenith Angle
TARTES	Two-streAm Radiative TransfEr in Snow
TD	Transpolar Drift
UTC	Universal Time, Coordinated
WMO	World Meteorological Organisation

List of symbols

A	Grain shape parameter
B	Absorption enhancement parameter
C	Flight attitude parameter
C_x	Concentration of impurities
d	Diameter
E	Irradiance
f	Focal length
g	Asymmetry parameter
h	Altitude
L	Radiance
M	Mass
n	Refractive index with real m and imaginary part m'
P	Phase function
p	Pressure
Q_e	Extinction efficiency
R	Ratio of diffuse radiation
r	Radius
r_eff	Effective radius
S	Surface
$\hat{S}$	SSA, specific surface area
s	Distance
SF	Surface forcing
t	Time
T	Temperature
V	Volume
z	Height

α Albedo

β Zenith angle of the sun relative to sensor plane

γ Absorption coefficient

ζ Uncertainty

η Built-in error

θ Zenith angle

κ MAC, mass specific absorption cross section

λ Wavelength

μ Cosine of the solar zenith angle

ρ Density

σ Cross section

φ Azimuth angle

τ Optical depth/thickness

ω Single scattering albedo

Ω Solid angle

Bibliography

AMAP (2011). *The Impact of Black Carbon on Arctic Climate.* By: P.K. Quinn, A. Stohl, A. Arneth, T. Berntsen, J. F. Burkhart, J. Christensen, M. Flanner, K. Kupiainen, H. Lihavainen, M. Shepherd, V. Shevchenko, H. Skov, and V. Vestreng. Arctic Monitoring and Assessment Programme (AMAP), Oslo, 72 pp.

Aoki, T., Aoki, T., Fukabori, M., Hachikubo, A., Tachibana, Y., and Nishio, F. (2000). Effects of snow physical parameters on spectral albedo and bidirectional reflectance of snow surface. *Journal of Geophysical Research: Atmospheres*, 105(D8):10219–10236.

Bannehr, L. and Schwiesow, R. (1993). A technique to account for the misalignment of pyranometers installed on aircraft. *Journal of Atmospheric and Oceanic Technology*, 10(5):774–777.

Barrie, L. A. (1986). Arctic air pollution: An overview of current knowledge. *Atmospheric Environment*, 20(4):643 – 663.

Bohren, C. F. and Barkstrom, B. R. (1974). Theory of the optical properties of snow. *Journal of Geophysical Research*, 79(30):4527–4535.

Bohren, C. F. and Beschta, R. L. (1979). Snowpack albedo and snow density. *Cold Regions Science and Technology*, 1(1):47–50.

Bohren, C. F. and Huffman, D. R. (2008). *Absorption and scattering of light by small particles.* John Wiley & Sons, New York, 544 pp.

Bond, T. C. and Bergstrom, R. W. (2006). Light absorption by carbonaceous particles: An investigative review. *Aerosol Science and Technology*, 40(1):27–67.

Bond, T. C., Doherty, S. J., Fahey, D., Forster, P., Berntsen, T., DeAngelo, B., Flanner, M., Ghan, S., Kärcher, B., Koch, D., et al. (2013). Bounding the role of black carbon in the climate system: A scientific assessment. *Journal of Geophysical Research: Atmospheres*, 118(11):5380–5552.

Bond, T. C., Habib, G., and Bergstrom, R. W. (2006). Limitations in the enhancement of visible light absorption due to mixing state. *Journal of Geophysical Research: Atmospheres*, 111(D20).

Brandt, R., Gerland, S., Pedersen, C., Berntsen, T., and Aamaas, B. (2008). Spectral albedo of the snow surface: Elson Lagoon, Barrow, AK 15-19 April 2008. *not published.*

Brandt, R. E., Warren, S. G., and Clarke, A. D. (2011). A controlled snowmaking experiment

testing the relation between black carbon content and reduction of snow albedo. *Journal of Geophysical Research: Atmospheres*, 116(D8).

Brodzik, M. J., Billingsley, B., Haran, T., Raup, B., and Savoie, M. H. (2012). Ease-grid 2.0: Incremental but significant improvements for earth-gridded data sets. *ISPRS International Journal of Geo-Information*, 1(1):32–45.

Carmack, E. C. (1990). Large-scale physical oceanography of polar oceans. *Polar Oceanography, Part A: Physical Science*, pages 171–222.

Carroll, J. J. and Fitch, B. W. (1981). Effects of solar elevation and cloudiness on snow albedo at the south pole. *Journal of Geophysical Research: Oceans (1978–2012)*, 86(C6):5271–5276.

Clarke, A. and Noone, K. (1984). Soot in the Arctic snowpack: A cause for perturbations in radiative transfer. *Atmospheric Environment*, 19:2045–2053.

Colbeck, S. C. (1982). An overview of seasonal snow metamorphism. *Reviews of Geophysics*, 20(1):45–61.

Conrady, K. (2013). Atmospheric concentration of black carbon in the western Arctic. Master's thesis, Meteorologisches Institut, Universität Hamburg.

Doherty, S., Warren, S., Grenfell, T., Clarke, A., and Brandt, R. (2010). Light-absorbing impurities in Arctic snow. *Atmospheric Chemistry and Physics*, 10(23):11647–11680.

Domine, F., Albert, M., Huthwelker, T., Jacobi, H.-W., Kokhanovsky, A., Lehning, M., Picard, G., and Simpson, W. (2008). Snow physics as relevant to snow photochemistry. *Atmospheric chemistry and physics*, 8(2):171–208.

Dumont, M., Brissaud, O., Picard, G., Schmitt, B., Gallet, J.-C., and Arnaud, Y. (2010). High-accuracy measurements of snow bidirectional reflectance distribution function at visible and nir wavelengths–comparison with modelling results. *Atmospheric Chemistry and Physics*, 10(5):2507–2520.

Eastwood, S. (2014). Sea ice product user's manual. Technical Report 3.11, OSI SAF.

Fierz, C., Armstrong, R. L., Durand, Y., Etchevers, P., Greene, E., McClung, D. M., Nishimura, K., Satyawali, P. K., and Sokratov, S. A. (2009). *The International Classification for Seasonal Snow on the Ground*. UNESCO/IHP.

Flanner, M. G. and Zender, C. S. (2005). Snowpack radiative heating: Influence on Tibetan Plateau climate. *Geophysical Research Lettersesearch letters*, 32(6).

Flanner, M. G. and Zender, C. S. (2006). Linking snowpack microphysics and albedo evolution. *Journal of Geophysical Research: Atmospheres (1984–2012)*, 111(D12).

Flanner, M. G., Zender, C. S., Hess, P. G., Mahowald, N. M., Painter, T. H., Ramanathan, V., and Rasch, P. J. (2009). Springtime warming and reduced snow cover from carbonaceous particles. *Atmospheric Chemistry and Physics*, 9(7):2481–2497.

Flanner, M. G., Zender, C. S., Randerson, J. T., and Rasch, P. J. (2007). Present-day climate

forcing and response from black carbon in snow. *Journal of Geophysical Research: Atmospheres*, 112.

Freese, D. (1999). *Solare und terrestrische Strahlungswechselwirkung zwischen arktischen Eisflächen und Wolken*. PhD thesis, Fachbereich Physik an der Universität Bremen.

Gallet, J.-C., Domine, F., Arnaud, L., Picard, G., and Savarino, J. (2011). Vertical profile of the specific surface area and density of the snow at Dome C and on a transect to Dumont D'Urville, Antarctica – albedo calculations and comparison to remote sensing products. *The Cryosphere*, 5(3):631–649.

Gardner, A. S. and Sharp, M. J. (2010). A review of snow and ice albedo and the development of a new physically based broadband albedo parameterization. *Journal of Geophysical Research*, 115.

Grenfell, T. C. (1991). A radiative transfer model for sea ice with vertical structure variations. *Journal of Geophysical Research: Oceans*, 96(C9):16991–17001.

Grenfell, T. C. and Perovich, D. K. (2008). Incident spectral irradiance in the Arctic Basin during the summer and fall. *Journal of Geophysical Research: Atmospheres*, 113(D12).

Grenfell, T. C. and Warren, S. G. (1999). Representation of a nonspherical ice particle by a collection of independent spheres for scattering and absorption of radiation. *Journal of Geophysical Research: Atmospheres*, 104(D24):31697–31709.

Haas, C., Lobach, J., Hendricks, S., Rabenstein, L., and Pfaffling, A. (2009). Helicopter-borne measurements of sea ice thickness, using a small and lightweight, digital em system. *Journal of Applied Geophysics*, 67(3):234–241.

Hansen, J. and Nazarenko, L. (2004). Soot climate forcing via snow and ice albedos. *Proceedings of the National Academy of Sciences of the United States of America*, 101(2):423–428.

Heinle, A., Macke, A., and Srivastav, A. (2010). Automatic cloud classification of whole sky images. *Atmospheric Measurement Techniques*, 3(3):557–567.

Hendricks, S., Ricker, R., and Helm, V. (2013). AWI CryoSat-2 Sea Ice Thickness Data Product. Data product manual, Alfred-Wegener-Institut.

Henyey, L. G. and Greenstein, J. L. (1941). Diffuse radiation in the galaxy. *Astrophysical Journal*, 93:70–83.

Herber, A. (2012). Regular Airborne Surveys of Arctic Sea Ice and Atmosphere. *Eos*, 93:41–48.

Hulst, H. C. and Van De Hulst, H. (1957). *Light scattering by small particles*. Courier Dover Publications, New York, 470 pp.

Kaempfer, T. U., Schneedbeli, M., and Pinzer, B. (2008). A micro-structural approach to snow metamorphism: Computed tomography experiments and numerical simulations. In *Proceedings Whistler 2008 International Snow Science Workshop September 21-27, 2008*, page 978.

Karlsson, K.-G., Riihelä, A., Müller, R., Meirink, J., Sedlar, J., Stengel, M., Lockhoff, M., Trentmann, J., Kaspar, F., Hollmann, R., et al. (2013). CLARA-A1: a cloud, albedo, and

radiation dataset from 28 yr of global AVHRR data. *Atmospheric Chemistry and Physics*, 13(10):5351–5367.

Kidder, S. Q. and Haar, T. H. V. (1995). *Satellite meteorology: An Introduction.* Gulf Professional Publishing, Waltham, 466 pp.

Kokhanovsky, A. A. (2006). *Cloud optics.* Springer, New York, 276 pp.

Kokhanovsky, A. A. and Zege, E. P. (2004). Scattering optics of snow. *Applied Optics*, 43(7):1589–1602.

Kou, L., Labrie, D., and Chylek, P. (1993). Refractive indices of water and ice in the 0.65-to 2.5-μm spectral range. *Applied Optics*, 32(19):3531–3540.

Kuipers Munneke, P., van den Broeke, M. R., Lenaerts, J. T. M., Flanner, M. G., Gardner, A. S., and van de Berg, W. J. (2011). A new albedo parameterization for use in climate models over the Antarctic ice sheet. *Journal of Geophysical Research: Atmospheres*, 116(D5).

Kumai, M. (1976). Identification of nuclei and concentrations of chemical species in snow crystals sampled at the south pole. *Journal of the Atmospheric Sciences*, 33(5):833–841.

Kurtz, N. T. and Farrell, S. L. (2011). Large-scale surveys of snow depth on Arctic sea ice from Operation IceBridge. *Geophys. Res. Lett.*, 38.

Kylling, A., Albold, A., and Seckmeyer, G. (1997). Transmittance of a cloud is wavelength-dependent in the UV-range: Physical interpretation. *Geophysical Research Letters*, 24(4):397–400.

Legagneux, L., Cabanes, A., and Domine, F. (2002). Measurement of the specific surface area of 176 snow samples using methane adsorption at 77 K. *Journal of Geophysical Research: Atmospheres*, 107(D17).

Legagneux, L., Taillandier, A., and Domine, F. (2004). Grain growth theories and the isothermal evolution of the specific surface area of snow. *Journal of Applied Physics*, 95(11, 1):6175–6184.

Li, W., Stamnes, K., Chen, B., and Xiong, X. (2001). Snow grain size retrieved from near-infrared radiances at multiple wavelengths. *Geophysical Research Letters*, 28(9):1699–1702.

Libbrecht, K. (2005). The physics of snow crystals. *Reports on Progress in Physics*, 68(4):855–895.

Libois, Q., Picard, G., Dumont, M., Arnaud, L., Sergent, C., Pougatch, E., Sudul, M., and Vial, D. (2014). Experimental determination of the absorption enhancement parameter of snow. *Journal of Glaciology*, 60(222):714.

Libois, Q., Picard, G., France, J. L., Arnaud, L., Dumont, M., Carmagnola, C. M., and King, M. D. (2013). Influence of grain shape on light penetration in snow. *The Cryosphere*, 7:1803–1818.

Marks, A. and King, M. (2013). The effects of additional black carbon on the albedo of Arctic sea ice: variation with sea ice type and snow cover. *The Cryosphere*, 7(4):1193–1204.

Markus, T., Stroeve, J. C., and Miller, J. (2009). Recent changes in Arctic sea ice melt onset, freezeup, and melt season length. *Journal of Geophysical Research: Oceans*, 114(C12).

McArthur, L. J. B. (2004). Baseline Surface Radiation Network (BSRN) Operations Manual. Operations Manual 1274, WCRP/WMO.

McClatchey, R., Fenn, R., Selby, J., Volz, F., and Garing, J. (1972). Optical properties of the atmosphere (third edition). *Air Force Cambridge Research Labs Report*, 72.

Meier, W. N., Hovelsrud, G. K., van Oort, B. E. H., Key, J. R., Kovacs, K. M., Michel, C., Haas, C., Granskog, M. A., Gerland, S., Perovich, D. K., Makshtas, A., and Reist, J. D. (2014). Arctic sea ice in transformation: A review of recent observed changes and impacts on biology and human activity. *Reviews of Geophysics*, 51.

Nakaya, U. (1954). Snowcrystals, natural and artificial. *HarvardUniv. Press. 510 pp.*

Otsu, N. (1979). A threshold selection method from gray-level histograms. *IEEE Transactions on Systems*, 9:62–66.

Painter, T. H. and Dozier, J. (2004). Measurements of the hemispherical-directional reflectance of snow at fine spectral and angular resolution. *Journal of Geophysical Research: Atmospheres*, 109(D18).

Paterson, W. and Reeh, N. (2001). Thinning of the ice sheet in northwest Greenland over the past forty years. *Nature*, 414(6859):60–62.

Perovich, D. K. and Polashenski, C. (2012). Albedo evolution of seasonal Arctic sea ice. *Geophysical Research Letters*, 39(8).

Perovich, D. K., Roesler, C. S., and Pegau, W. S. (1998). Variability in Arctic sea ice optical properties. *Journal of Geophysical Research: Oceans*, 103(C1):1193–1208.

Picard, G., Arnaud, L., Domine, F., and Fily, M. (2009). Determining snow specific surface area from near-infrared reflectance measurements: Numerical study of the influence of grain shape. *Cold Regions Science and Technology*, 56(1):10 – 17.

Predoehl, N. M. C., Predoehl, N. M. C., Spano, A. F., Predoehl, M. C., Angel, and Span, F. (1965). Airborne Albedo Measurements over the Ross Sea October-November 1962. *Monthly Weather Review*, 1:687–696.

Ramaswamy, V., Boucher, O., Haigh, J., Hauglustaine, D., Haywood, J., Myhre, G., Nakajima, T., Shi, G. Y., and Solomon, S. (2001). *Radiative Forcing of Climate Change. In: Climate Change 2001*, volume 3. Cambridge University Press, Cambridge, United Kingdom and New York, NY, USA.

Rebhan, H., Drinkwater, M., and Ratier, G. (2003). CryoSat Science Report. Technical Report 1272, ESA.

Ricchiazzi, P., Yang, S., Gautier, C., and Sowle, D. (1998). SBDART: A research and teaching software tool for plane-parallel radiative transfer in the Earth's atmosphere. *Bulletin of the American Meteorological Society*, 79(10):2101–2114.

Samset, B. H., Myhre, G., Herber, A., Kondo, Y., Li, S.-M., Moteki, N., Koike, M., Oshima, N., Schwarz, J. P., Balkanski, Y., Bauer, S. E., Bellouin, N., Berntsen, T. K., Bian, H., Chin, M.,

Diehl, T., Easter, R. C., Ghan, S. J., Iversen, T., Kirkevåg, A., Lamarque, J.-F., Lin, G., Liu, X., Penner, J. E., Schulz, M., Seland, Ø., Skeie, R. B., Stier, P., Takemura, T., Tsigaridis, K., and Zhang, K. (2014). Modeled black carbon radiative forcing and atmospheric lifetime in AeroCom Phase II constrained by aircraft observations. *Atmospheric Chemistry & Physics*, 436.

Schwarz, J., Gao, R., Fahey, D., Thomson, D., Watts, L., Wilson, J., Reeves, J., Darbeheshti, M., Baumgardner, D., Kok, G., et al. (2006). Single-particle measurements of midlatitude black carbon and light-scattering aerosols from the boundary layer to the lower stratosphere. *Journal of Geophysical Research: Atmospheres (1984–2012)*, 111(D16).

Sergent, C., Pougatch, E., Sudul, M., and Bourdelles, B. (1993). Experimental investigation of optical snow properties. *Annals of Glaciology*, 17:281–287.

Solar Radiation Monitoring Laboratory at the University of Oregon (2000). Eppley Precision Spectral Pyranometer (PSP): [http://solardat.uoregon.edu/EppleyPSP.html].

Stamnes, K., Tsay, S.-C., Wiscombe, W., Jayaweera, K., et al. (1988). Numerically stable algorithm for discrete-ordinate-method radiative transfer in multiple scattering and emitting layered media. *Applied Optics*, 27(12):2502–2509.

Stocker, T., Qin, D., Plattner, G.-K., Alexander, L., Allen, S., Bindoff, N., Bréon, F.-M., Church, J., Cubasch, U., Emori, S., Forster, P., Friedlingstein, P., Gillett, N., Gregory, J., Hartmann, D., Jansen, E., Kirtman, B., Knutti, R., Krishna Kumar, K., Lemke, P., Marotzke, J., Masson-Delmotte, V., Meehl, G., Mokhov, I., Piao, S., Ramaswamy, V., Randall, D., Rhein, M., Rojas, M., Sabine, C., Shindell, D., Talley, L., Vaughan, D., and Xie, S.-P. (2013). *Technical Summary. In: Climate Change 2013: The Physical Science Basis*, volume 5. Cambridge University Press, Cambridge, United Kingdom and New York, NY, USA.

Stone, R. S. (2002). Monitoring aerosol optical depth at Barrow, Alaska and South Pole; historical overview, recent results and future goals. In *Conference proceedings - Italian Physical Society*, volume 80, pages 123–144.

Stone, R. S., Herber, A., Vitale, V., Mazzola, M., Lupi, A., Schnell, R. C., Dutton, E. G., Liu, P. S. K., Li, S.-M., Dethloff, K., Lampert, A., Ritter, C., Stock, M., Neuber, R., and Maturilli, M. (2010). A three-dimensional characterization of Arctic aerosols from airborne Sun photometer observations: PAM-ARCMIP, April 2009. *Journal of Geophysical Research: Atmospheres*, 115(D13).

Stroeve, J., Markus, T., Boisvert, L., Miller, J., and Barrett, A. (2014). Changes in Arctic melt season and implications for sea ice loss. *Geophysical Research Letters*, 41(4):1216–1225.

Thekaekara, M. P. (1974). Extraterrestrial solar spectrum, 3000–6100 Å at 1-Å intervals. *Applied Optics*, 13(3):518–522.

Thomas, D. N. and Dieckmann, G. S. (2009). *Sea ice*. John Wiley & Sons, New York, 634 pp.

Van de Hulst, H. (1968). Asymptotic fitting, a method for solving anisotropic transfer problems in thick layers. *Journal of Computational Physics*, 3(2):291–306.

van Leeuwen, W. J. and Roujean, J.-L. (2002). Land surface albedo from the synergistic use of polar

(EPS) and geo-stationary (MSG) observing systems: An assessment of physical uncertainties. *Remote Sensing of Environment*, 81(2–3):273 – 289.

Wadhams, P. (2000). *Ice in the Ocean.* CRC Press, New York, 364 pp.

Warren, S. G. (1982). Optical properties of snow. *Reviews of Geophysics*, 20(1):67–89.

Warren, S. G. (2013). Can black carbon in snow be detected by remote sensing? *Journal of Geophysical Research: Atmospheres*, 118(2):779–786.

Warren, S. G. and Brandt, R. E. (2008). Optical constants of ice from the ultraviolet to the microwave: A revised compilation. *Journal of Geophysical Research: Atmospheres*, 113(D14).

Warren, S. G., Brandt, R. E., and O'Rawe Hinton, P. (1998). Effect of surface roughness on bidirectional reflectance of Antarctic snow. *Journal of Geophysical Research: Planets*, 103(E11):25789–25807.

Warren, S. G., Rigor, I. G., Untersteiner, N., Radionov, V. F., Bryazgin, N. N., Aleksandrov, Y. I., and Colony, R. (1999). Snow Depth on Arctic Sea Ice. *Journal of Climate*, 12(6):1814–1829.

Warren, S. G. and Wiscombe, W. J. (1980). A model for the spectral albedo of snow. II: Snow containing atmospheric aerosols. *Journal of the Atmospheric Sciences*, 37(12):2734–2745.

Webster, M. A., Rigor, I. G., Nghiem, S. V., Kurtz, N. T., Farrell, S. L., Perovich, D. K., and Sturm, M. (2014). Interdecadal changes in snow depth on Arctic sea ice. *Journal of Geophysical Research: Oceans*, 119(8):5395–5406.

Wendisch, M., Müller, D., Schell, D., and Heintzenberg, J. (2001). An airborne spectral albedometer with active horizontal stabilization. *Journal of Atmospheric and Oceanic Technology*, 18(11):1856–1866.

Wendisch, M., Pilewskie, P., Jäkel, E., Schmidt, S., Pommier, J., Howard, S., Jonsson, H. H., Guan, H., Schröder, M., and Mayer, B. (2004). Airborne measurements of areal spectral surface albedo over different sea and land surfaces. *Journal of Geophysical Research: Atmospheres*, 109(D8).

Willmott, C. J. and Matsuura, K. (2005). Advantages of the mean absolute error (MAE) over the root mean square error (RMSE) in assessing average model performance. *Climate Research*, 30(1):79.

Wiscombe, W. J. (1980). Improved Mie scattering algorithms. *Applied optics*, 19(9):1505–1509.

Wiscombe, W. J. and Warren, S. G. (1980). A model for the spectral albedo of snow. I: Pure snow. *Journal of the Atmospheric Sciences*, 37(12):2712–2733.

Xiong, C. and Shi, J. (2014). Simulating polarized light scattering in terrestrial snow based on bicontinuous random medium and Monte Carlo ray tracing. *Journal of Quantitative Spectroscopy and Radiative Transfer*, 133(0):177 – 189.

Xiong, X., Stamnes, K., and Lubin, D. (2002). Surface albedo over the Arctic Ocean derived from AVHRR and its validation with SHEBA data. *Journal of applied Meteorology*, 41(4):413–425.

Zege, E., Katsev, I., Malinka, A., Prikhach, A., Heygster, G., and Wiebe, H. (2011). Algorithm for retrieval of the effective snow grain size and pollution amount from satellite measurements. *Remote Sensing of Environment*, 115(10):2674 – 2685.

Zhou, X., Li, S., and Stamnes, K. (2003). Effects of vertical inhomogeneity on snow spectral albedo and its implication for optical remote sensing of snow. *Journal of Geophysical Research: Atmospheres*, 108(D23).

Acknowledgements

First of all, I would like to thank Prof. Dr. Gunther Seckmeyer for allowing me to leave the normal trails and take this opportunity. I have to thank you, Ansgar Stührmann and the whole workgroup at the IMuK for your time, good advice, guidance and supervision. I am also very grateful to Dr. Andreas Herber, Dr. Gerit Birnbaum and Prof. Dr. Rüdiger Gerdes from the AWI in Bremerhaven for inviting me to the sea-ice group and providing me with data and this great topic I loved to devote so much blood and sweat. Thank you for so much help and support and thank you for introducing me so many interesting new colleagues and friend. Thanks to everyone I met on this journey and who shared some inspiring conversation or good advice with me. Without the motivating discussions supporting the progress of this thesis it all would not have been possible. Thank you lots!

I thank Richard Brandt from the Atmospheric Science Department at the University of Washington for supporting this thesis with a his field-measurement data from Barrow, Christine Pohl from the IMuK for her figure of the camera sensitivity and Klaus Behrens from the DWD in Lindenberg for his explanations on problems with the cosine response of pyranometers.

Also, I have to thank my family and friends for keeping me sane. Thank you for not minding my bad mood and the little time I had for every one of you. Thanks for your encouragement and help. I owe you a lot!

And last but not least, I am very grateful to everyone who read my thesis and gave hints for improvement. I am very, very thankful for your help! Thanks for your time!

Eidesstattliche Erklärung

Hiermit erkläre ich, dass ich die vorliegende Masterarbeit selbstständig und nur unter Verwendung der angegebenen Quellen und Hilfsmittel sowie dem Rat meiner akademischen Lehrer angefertigt habe.

Hannover, d. 20.11.2014

Hannes Schulz